Magnetism in uranium and praseodymium intermetallic compounds studied by inelastic neutron scattering

University College London

A thesis submitted in accordance with the requirements of the University of London for the degree of Doctor of Philosophy

Jonathan Paul Allen

2003

ProQuest LLC
789 East Eisenhower Parkway
P.O. Box 1346
Ann Arbor, MI 48106-1346

Abstract

The dispersion of magnetic excitations in PrNiSn has been studied using inelastic neutron scattering. The dispersion relations along [0 0 **Q**] and [**Q** 0 0] have been determined for the excitations observed at 1.5, 2.5 and 5.2 meV. The two lower excitations are proposed to be modes originating from the 2 meV level predicted by earlier inelastic measurements. Additional measurements of the 3.5 meV excitation already studied were performed to provide higher resolution data and improved statistics. Preliminary measurements on NdNiSn were also made.

Searches have been made using inelastic neutron scattering to look for crystalline electric field (CEF) excitations in the uranium-based intermetallics UPdSn, UCu_2Sn and $U_3Pd_{20}Si_6$.

In UPdSn, a distinct CEF excitation has been observed at 50 meV in the paramagnetic phase. On cooling, the excitation shifts to lower energies and its temperature dependence exhibits marked changes at the antiferromagnetic transition temperatures of T_N = 25 and 40 K. The quasielastic scattering below 20 meV is found to increase significantly below the lower transition temperature. A set of Stevens parameters have been proposed to account for the observed data.

The magnetic scattering observed in UCu_2Sn is a broad, asymmetric peak centred at 7 meV which disappears above the quadrupolar ordering temperature of T_Q = 16.5 K. The temperature dependence of the peak has been determined and comparisons with two different energy level schemes have been made.

Three clear CEF excitations, which are visible in both the paramagnetic and ordered phase, have been observed at energies of 14.3, 23.9 and 31.6 meV in $U_3Pd_{20}Si_6$. The temperature dependence of the excitations has been followed and a tentative level scheme proposed. A sharp, intense peak at 3 meV is visible at low temperatures and has been attributed to the exchange induced splitting of the 8*c* ground state below T_N = 19 K.

Acknowledgements

First and foremost, I would like to thank my supervisor Professor Keith McEwen for his help and guidance over the course of my PhD. Thanks must also go to Dr Stan Zochowski and Dr Mark Ellerby who were always there when I needed them and even when I didn't!

The instrument scientists who helped me obtain all of my data must also be mentioned. So thank you to Rob Bewley, Martin Bull, Devashibhai Adroja, Björn Fåk, Klaus Habicht and Jens Klenke.

Thanks to everyone at UCL who kept me entertained during the long days in F10b and during the long nights in Huntley Street! Thanks for their friendship and support goes to Shusaku Hayama, Daniel Ucko, Gary Martin, Jonathan Wasse, Simon Armitage, Louise Affleck, Helen Thompson, Hayley Spiers, Tom Weller and Chris Howard. Thanks also to Laura Glynn for the much needed tea breaks. And of course I can't forget my mentor, Eamonn Beirne!

I'd like to thank my brother Mark and sister Lois for always being there for me and, finally, a huge thank you goes to my parents, David and Ruth, for the love and support they have given to me throughout my life.

Contents

List of Figures

Chapter 1

Chapter 2

Chapter 4

Chapter 5

Chapter 6

Chapter 7

Chapter 8

List of Tables

Chapter 3

Chapter 5

Chapter 6

Chapter 7

Chapter 8

CHAPTER 1

Magnetism

1.1 Lanthanides and actinides

Many of the most interesting discoveries in the field of condensed matter physics have come from materials which include elements from the lanthanide or actinide series. Some examples are unconventional superconductivity, heavy fermions, non-Fermi liquid behaviour and quantum critical points. Lanthanides and actinides are characterised by having unpaired electrons in the *f* shell and their diverse behaviour is due to interactions between the highly anisotropic *f* electron wavefunctions. It is clear that such "*f* electron" physics is a fascinating area of research.

Intermetallics containing magnetic ions exhibit different types of behaviour depending on the interactions between the magnetic moments. In the lanthanide series, the 4*f* electrons are deeply embedded within the atom and their wavefunctions do not extend particularly far. This means that most materials containing lanthanide ions exhibit *localised* magnetism with magnetic moments that are usually close to the free ion values.

The actinide series is very different because the 5*f* electrons are often involved in bonding and their wavefunctions are more spatially extended. Most actinide based materials therefore exhibit *itinerant* magnetism in which energy bands are formed instead of discrete energy levels. The magnetic moments in such materials are therefore much smaller than the free ion values.

Uranium is on the border between the localised and itinerant regimes and thus compounds containing uranium can be used to look at the crossover from one to the other. Unfortunately, uranium compounds showing localised behaviour are relatively rare and so compounds which exhibit such behaviour, like those studied in this thesis, are particularly interesting. In order to understand the experimental results, the mechanisms behind localised moment magnetism must be understood. The rest of this chapter will therefore be used to describe the basic theories of magnetism.

1.2 Paramagnetism

For free atoms, the magnetic moment consists of three components. Firstly, the intrinsic spin of the electrons provides a paramagnetic contribution. A second paramagnetic contribution comes from the orbital angular momentum of the electrons about the nucleus. The third component is a diamagnetic one, which arises from the change in orbital moment induced by a magnetic field.

Atoms with completely filled electron shells have zero spin and orbital angular momentum in their ground state, hence only the diamagnetic component contributes to the susceptibility. However, atoms with a partially filled inner shell (such as rare-earth and actinide elements) and solids containing atoms with partially filled electron shells exhibit very different magnetic properties. In these cases, we will have some form of paramagnetism.

In order to obtain a simple theory that describes such magnetism, it is assumed that the sources of magnetic moment (e.g. unfilled electron shells or conduction electrons) do not interact with each other. Later, an interaction between moments will be included in order to account for magnetic ordering.

The magnetic moment of a free ion is given by:

$$\boldsymbol{\mu} = g\mu_B \mathbf{J}$$

where $\mu_B = e\hbar/2m$ is the Bohr magneton and g is the Landé factor given by:

$$g = 1 + \frac{J(J+1) + S(S+1) - L(L+1)}{2J(J+1)}$$

Such an ion will have a set of J-multiplets arising from a given L and S, and the ground state will be $(2J + 1)$-fold degenerate in zero field. To calculate the value of the total angular momentum, **J**, we use Hund's rules:

i. Maximise the total spin, S, consistent with the Pauli exclusion principle.

ii. Maximise the total orbital angular momentum, L, consistent with rule (i) and the Pauli exclusion principle.

iii. Calculate the total angular momentum, J, using:
$J = |L - S|$, if the shell is less than half-full,
$J = |L + S|$, if the shell is more than half-full.

For example, the ions Pr^{3+} and U^{4+} both have two f electrons so $g = 0.8$, $S = 1$, $L = 5$ and $J = |L - S| = 4$, which gives the free ion magnetic moment as 3.2 μ_B.

This method of calculating the total angular momentum, i.e. $J = \sum l_i + \sum s_i$, is known as *Russell-Saunders (LS) coupling*. Note that another method known as *j-j coupling*, i.e. $J = \sum j_i = \sum (l_i + s_i)$, is used when the coupling between the spin and orbital angular momentum for each electron is stronger than the *l-l* or *s-s* coupling between electrons. This is more applicable to very heavy atoms.

The degeneracy of the J-multiplet is lifted by the Zeeman interaction between the magnetic moment and an applied field and produces $(2J + 1)$ states with energies:

$$H_{Zeeman} = -\boldsymbol{\mu} \cdot \mathbf{B} = -g\mu_B J_Z B$$

for a field applied along the z-axis. At a finite temperature, the levels are populated according to the Boltzmann distribution:

$$P(E_i) = \frac{e^{-E_i/k_BT}}{\sum_i e^{-E_i/k_BT}}$$

which, assuming **M** is parallel to **B**, leads to a susceptibility of the form:

$$\chi = \mu_0 \frac{\partial M}{\partial B} = n\mu_0 \mu_B gJ \left[\frac{2J+1}{2J} \coth\left(\frac{2J+1}{2J} \cdot \frac{g\mu_B JB}{k_BT} \right) - \frac{1}{2J} \coth\left(\frac{1}{2J} \cdot \frac{g\mu_B JB}{k_BT} \right) \right]$$

where the term in square brackets is the Brillouin function with $x = g\mu_B JB/k_BT$. At high temperatures and small magnetic fields, i.e. for small x, the above equation gives the *Curie paramagnetic susceptibility*:

$$\chi = \frac{n\mu_0 \mu_B^2 g^2 J(J+1)}{3k_BT} = \frac{n\mu_0 \mu_{eff}^2}{3k_BT} = \frac{C}{T}$$

where n is the number of ions per unit volume and $\mu_{eff} = \mu_B g\sqrt{J(J+1)}$ is the effective magnetic moment of each ion. In the $5f^2$ and $5f^3$ configurations of uranium, for example, the effective moments are 3.58 and 3.62 μ_B, respectively. In uranium compounds which show itinerant magnetism the effective magnetic moments are much smaller than expected, hence the magnitude of μ_{eff} can be used as an indication of the degree of f electron localisation.

1.3 Magnetic Order

1.3.1 Curie-Weiss mean field theory

In zero applied field, non-interacting magnetic ions are randomly oriented so the net magnetic moment is zero. As a field is applied the magnetic moments begin to align along the direction of the field and the net magnetic moment is initially proportional to the field strength, i.e. $M \propto B$ for small fields.

Some materials, however, exhibit a net magnetic moment even in zero field, when they are cooled below a critical Curie temperature T_C. This type of behaviour is known as *ferromagnetism.* (In antiferromagnetism the spins also align, but antiparallel to one another. Although this does not result in a net moment, the moments are still well ordered in zero field below a critical Néel temperature T_N).

Such a transition from a disordered paramagnetic state to a highly ordered magnetic state requires a coupling between the individual magnetic ions. To model this interaction we assume that each of the magnetic ions experiences an internal field proportional to the magnetisation, in addition to any applied field:

$$B_{eff} = B_{app} + B_{\text{int}} = B + \lambda M$$

This is obviously a *mean field* theory since we are considering one spin in the mean field produced by all of the other spins. Inserting this into $M = \chi_0 B_{eff} / \mu_0$, where $\chi_0 = C/T$ is the susceptibility for non-interacting moments, gives the Curie-Weiss susceptibility:

$$\chi_{CW} = \mu_0 \frac{M}{B} = \left(\frac{\chi_0}{1 - \lambda \chi_0} \right) = \frac{C}{(T - \lambda C)} = \frac{C}{(T - T_C)}$$

Spontaneous magnetisation occurs at and below the singularity at $T = T_C$. (Note that for non-interacting moments we have $\lambda = 0$ which gives $\chi = C/T$ as before.) The internal field can be estimated as the temperature tends to zero by:

$$B_{\text{int}} = \lambda M = \frac{T_C}{C} M = \frac{3k_B T_C}{ng^2 \mu_B^2 J(J+1)} ng\mu_B J = \frac{3k_B T_C}{g\mu_B (J+1)}$$

1.3.2 Heisenberg exchange interaction

Heisenberg explained the origin of this internal (or exchange) field by considering the electrostatic interaction between the charge densities of two ions. The Pauli exclusion principle states that the wavefunction of a complete system must be antisymmetric with respect to the exchange of two fermions, such as electrons (with spin s_i at position $\mathbf{r}_i$):

$$\text{i.e. } \Psi(\mathbf{r}_1, s_1, \mathbf{r}_2, s_2) = -\Psi(\mathbf{r}_2, s_2, \mathbf{r}_1, s_1)$$

The total wavefunction can be written as the product of spatial and spin parts:

$$\text{i.e. } \Psi(\mathbf{r}_1, s_1, \mathbf{r}_2, s_2) = \alpha(\mathbf{r}_1, \mathbf{r}_2) \cdot \beta(s_1, s_2)$$

So, if $\beta(s_1, s_2)$ is antisymmetric (i.e. a *singlet* state with $S = 0$, $S_Z = 0$) then $\alpha(\mathbf{r}_1, \mathbf{r}_2)$ must be symmetric, and if $\beta(s_1, s_2)$ is symmetric (i.e. a *triplet* state with $S = 1$, $S_Z = -1, 0, 1$) then $\alpha(\mathbf{r}_1, \mathbf{r}_2)$ must be antisymmetric. Therefore, for the spatial part:

$$\alpha_S = \tfrac{1}{\sqrt{2}}[\psi_a(\mathbf{r}_1)\psi_b(\mathbf{r}_2) + \psi_b(\mathbf{r}_1)\psi_a(\mathbf{r}_2)]$$
$$\alpha_T = \tfrac{1}{\sqrt{2}}[\psi_a(\mathbf{r}_1)\psi_b(\mathbf{r}_2) - \psi_b(\mathbf{r}_1)\psi_a(\mathbf{r}_2)]$$

where $\psi_a(\mathbf{r}_1)$ represents the wavefunction of electron 1 in state *a*, and $\psi_b(\mathbf{r}_2)$ represents the wavefunction of electron 2 in state *b*.

This leads directly to a correlation between the spins of electrons on two different ions, which is all that is required for a magnetically ordered state. The *direct* Heisenberg *exchange interaction* between atomic spins can be written as:

$$H_{ex} = -2J_{ex}\sum \mathbf{S}_i \cdot \mathbf{S}_j$$

where the *exchange integral* is given by:

$$J_{ex} = \int \psi_a^*(\mathbf{r}_1)\psi_b^*(\mathbf{r}_2)U(\mathbf{r}_1,\mathbf{r}_2)\psi_b(\mathbf{r}_1)\psi_a(\mathbf{r}_2)d\tau$$

and $U(\mathbf{r}_1,\mathbf{r}_2)$ is a function which describes the interaction between the electrons and the ions and between the electrons themselves. Ferromagnetism results when $J > 0$ and antiferromagnetism results when $J < 0$.

1.3.3 RKKY interaction

In rare earth intermetallics, there is little direct overlap of the *4f* electron wavefunctions which means that the exchange interaction cannot act directly between them. Instead, the exchange interaction acts between the localised *4f* electrons and the conduction electrons. The polarised conduction electrons thereby mediate the spin between *4f* electrons. This *indirect* exchange mechanism was formulated by Ruderman, Kittel, Kasuya & Yoshida and is therefore known as the *RKKY interaction.*

In this case, the Heisenberg exchange is rewritten in terms of J_{ij}, the Fourier transform of the q-dependent exchange integral $J(q)$, as:

$$H_{ex} = -\frac{1}{2}\sum_{i\neq j} J_{ij}\,\mathbf{J}_i \cdot \mathbf{J}_j$$

The RKKY interaction is a long-range, oscillatory function and the interaction with a given ion will be either ferromagnetic or antiferromagnetic depending on the distance from it. It is this interaction which is responsible for the complex and often periodic magnetic structures in the rare earth elements.

1.3.4 Spin waves

Consider a line or ring of N ions of spin S with nearest neighbours coupled by the Heisenberg interaction (shown schematically in Figure 1.1):

$$U = -2J_{ex}\sum_{p=1}^{N}\mathbf{S}_p \cdot \mathbf{S}_{p+1}$$

The ground state energy of the system is therefore given by $U_0 = -2J_{ex}NS^2$. Now consider an excited state in which the p^{th} spin is reversed. The energy of this excited state is $U_1 = -2J_{ex}(N-1)S^2 + 2J_{ex}S^2 = U_0 + 4J_{ex}S^2$.

Figure 1.1 The ground state (left) and an excited state (right) of a line of aligned spins.

There is, however, an excited state known as a magnon (or *spin wave*) which has a lower energy than this. In this configuration, the spins 'share' the reversal by precessing around their mean direction but with a uniform phase change between successive spins (see Figure 1.2). In the case when the precession angle is small, the energy of the system is:

$$U(\theta) = -2J_{ex}(N\cos\theta)S^2 = U_0 + J_{ex}N\theta^2S^2$$

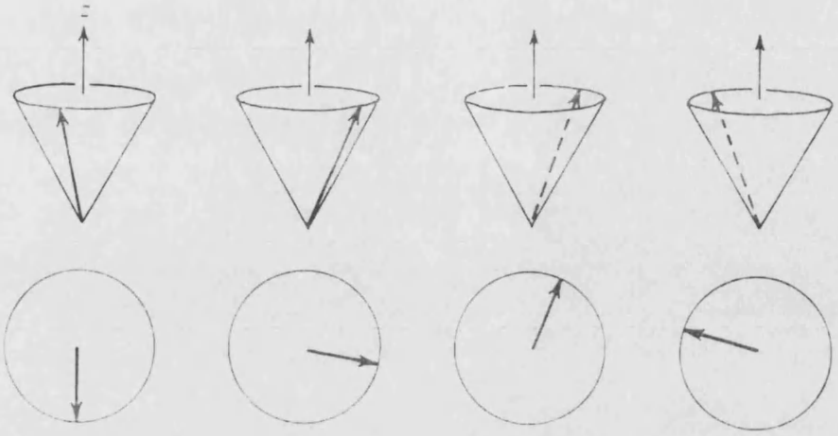

Figure 1.2 The precession of a one dimensional spin wave.

For a rotation of π over the N spins (which is equivalent to the reversal of one spin) we have $U(\theta) = U_0 + J_{ex}\pi^2 S^2 / N$. So as the number of spins increases, the energy of the spin wave state becomes lower than when a single spin is reversed.

It is assumed that the precession angle is small and that the spin wave is in the form of a travelling wave, $S_p \propto \exp[i(Qa - \omega t)]$ where Q is the wavevector and a is the spin separation distance. The dispersion for a one-dimensional ferromagnet is then given by $\hbar\omega = 4J_{ex}S(1-\cos Qa)$ which means that $\omega \propto Q^2$ in the long wavelength limit. (Note that the long wavelength limit for phonons is $\omega \propto Q$). Magnon dispersion relations for real crystals can be determined by inelastic neutron scattering, in exactly the same way as for phonon dispersion relations which arise from lattice excitations.

1.4 Crystalline Electric Fields

The energy spectrum of an isolated magnetic ion in a crystal carries information about the magnetic ion itself, the crystalline environment and the interaction between the two. In a periodic lattice of magnetic ions, each ion experiences an electrostatic potential due to the regular array of charges from the surrounding ions. If the symmetry of the lattice is high enough, this *crystalline electric field* (CEF) will lift the degeneracy of the ground state multiplet to form various (possibly degenerate) sub-levels.

The splittings of these levels are usually much smaller than the multiplet separations, so the mixing of different multiplets can usually be neglected. The magnitude of the energy splitting between these levels is also comparable to thermal energies and therefore many physical quantities are strongly affected by their changing populations. Techniques commonly used to detect such CEF levels include magnetisation, resistivity, susceptibility, heat capacity measurements and neutron scattering.

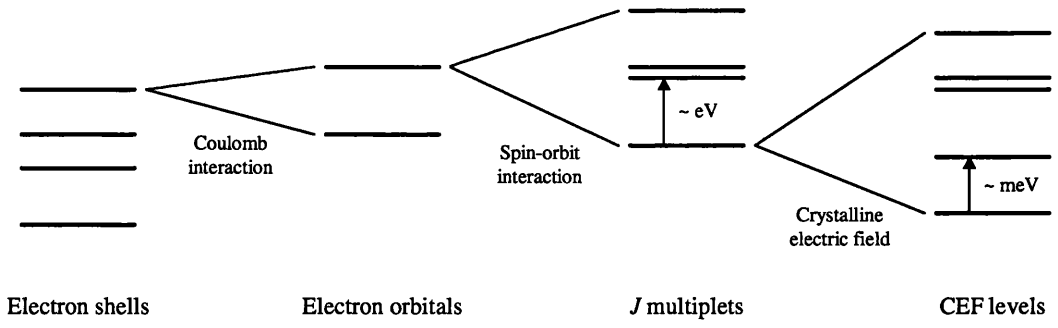

Figure 1.3 Schematic diagram showing typical energy level splittings due to interactions between the *f* electrons and their environment.

There are two general theorems which apply to the lowest energy level produced by the CEF splitting:

- *Kramers' theorem* states that, in the absence of an applied field, an ion containing an odd number of f electrons has CEF levels which are at least doubly degenerate.

- The *Jahn-Teller effect* causes the environment around an ion with a degenerate (non-Kramers) ground state to distort to a lower symmetry so as to remove the degeneracy.

1.4.1 CEF Hamiltonian

In rare-earth and light actinide elements, the CEF interaction is weaker than the spin-orbit interaction and can therefore be treated as a perturbation of the free ion Hamiltonian. The CEF perturbation Hamiltonian is given by:

$$\mathrm{H}_{CEF} = \sum_i q_i V_i = \sum_i \sum_j \frac{q_i q_j}{|\mathbf{r}_j - \mathbf{r}_i|}$$

and determines the effect that charges q_j situated at distances $\mathbf{r}_j$ from the origin have on the unpaired electrons q_i within the magnetic ion at $\mathbf{r}_i$ from the origin.

Each contribution to the potential can be represented as the product of a radial component, $f(r)$, and a spherical harmonic, $Y_n^m(\theta,\phi)$. In order to calculate the eigenvalues and eigenvectors of the ion, the CEF transition matrix must be diagonalised. This task is simplified considerably by noting that, within a specific J multiplet, the matrix elements of the Y_n^m operators are proportional to those of J-operator equivalents.

Using the *Stevens operator equivalents*[1], O_n^m, the CEF Hamiltonian becomes:

$$H_{CEF} = \sum_{nm} \left[c_n \left\langle r^n \right\rangle A_n^m \right] O_n^m = \sum_{nm} B_n^m O_n^m$$

where the c_n are multiplicative Stevens factors which can be calculated using standard formulae[2] and $\left\langle r^n \right\rangle$ is the mean n^{th} power of the magnetic electron radius.

The B_n^m are known as the *crystal field parameters*. In theory, it should be possible to calculate their values from the charge distribution in the material, although in practice this proves to be too difficult.

These parameters can be determined experimentally, however, from measurements of specific heat, susceptibility and inelastic neutron scattering. Single crystal samples are especially useful since the different symmetry directions can be looked at independently. In fact, determination of the paramagnetic Curie temperatures, θ_α, along the three principle axes allows the B_2^0 and B_2^2 parameters to be obtained directly from the high temperature susceptibility, since[3]:

$$\begin{aligned}
\theta_a &= \theta_p + \tfrac{1}{10k_B}(2J-1)(2J+3)\left[B_2^0 + B_2^2\right] \\
\theta_b &= \theta_p - \tfrac{1}{5k_B}(2J-1)(2J+3)\left[B_2^0\right] \\
\theta_c &= \theta_p + \tfrac{1}{10k_B}(2J-1)(2J+3)\left[B_2^0 - B_2^2\right]
\end{aligned}$$

and rearranging these gives:

$$\begin{aligned}
B_2^0 &= \frac{5}{3} k_B \frac{(\theta_a + \theta_c - 2\theta_b)}{(2J-1)(2J+3)} \\
B_2^2 &= 5 k_B \frac{(\theta_a - \theta_c)}{(2J-1)(2J+3)}
\end{aligned}$$

In practice, these calculated values are used as starting parameters which are allowed to vary when fitting to the experimental data. The number of terms needed to describe the CEF potential is determined by the symmetry of the magnetic lattice, with more terms required as the symmetry is reduced:

$$
\begin{aligned}
(H_{CEF})_{cubic} &= B_4^0 O_4^0 + B_4^4 O_4^4 + B_6^0 O_6^0 + B_6^4 O_6^4 \\
(H_{CEF})_{hexagonal} &= B_2^0 O_2^0 + B_4^0 O_4^0 + B_6^0 O_6^0 + B_6^6 O_6^6 \\
(H_{CEF})_{tetragonal} &= B_2^0 O_2^0 + B_4^0 O_4^0 + B_4^4 O_4^4 + B_6^4 O_6^4 + B_6^0 O_6^0 \\
(H_{CEF})_{orthorhombic} &= B_2^0 O_2^0 + B_2^2 O_2^2 + B_4^0 O_4^0 + B_4^2 O_4^2 + B_4^4 O_4^4 \\
&\quad + B_6^0 O_6^0 + B_6^2 O_6^2 + B_6^4 O_6^4 + B_6^6 O_6^6
\end{aligned}
$$

The eigenfunctions obtained by diagonalisation are written, using the notation of Bethe[4], as Γ_i where i = 1,2,3,4,5 for integer J and i = 6,7,8 for half-integer J. In this notation, Γ_1 and Γ_2 are singlet states, Γ_3 is a non-magnetic doublet, Γ_4 and Γ_5 are magnetic triplets, Γ_6 and Γ_7 are magnetic doublets and Γ_8 is a quartet.

1.4.2 Bulk properties

Using the eigenvalues E_n and eigenfunctions λ_n obtained from the diagonalisation of the CEF transition matrix, the paramagnetic susceptibility, magnetisation and magnetic specific heat can be calculated[5,6,7] (for a field applied along $\alpha = x, y, z$) via:

$$
\chi_{\alpha\alpha}(T) = N(g_J \mu_B)^2 \left[\sum_n \beta \frac{e^{-\beta E_n}}{Z} \langle \lambda_n | J_\alpha | \lambda_n \rangle^2 + \sum_n \sum_m \frac{1}{\Delta E} \frac{e^{-\beta E_m} - e^{-\beta E_n}}{Z} \langle \lambda_m | J_\alpha | \lambda_n \rangle^2 \right]
$$

$$
M_\alpha(T) = g_J \mu_B \sum_n \frac{e^{-\beta E_n}}{Z} \langle \lambda_n | J_\alpha | \lambda_n \rangle
$$

$$
C(T) = k_B \sum_n \frac{e^{-\beta E_n}}{Z} \left(\frac{E_n}{k_B T} \right)^2 - k_B \sum_n \left(\frac{e^{-\beta E_n}}{Z} \frac{E_n}{k_B T} \right)^2
$$

where $\beta = 1/k_B T$, $\Delta E = E_m - E_n$ and the partition function $Z = \sum e^{-\beta E_{\lambda_i}}$.

Since the susceptibility depends on the matrix elements between CEF eigenstates it is sensitive to the arrangement of the eigenstates within the level scheme. It was shown by Van Vleck[8] that the thermal population of multiplets above the ground state multiplet has a significant effect on the measured susceptibility.

The CEF modifies the susceptibility in a similar way. This is reflected in the second term in the susceptibility which is dependent on the transition between different eigenstates. Thus there is a Curie-type term and a Van Vleck-type term.

If the ground state is non-magnetic, the only contribution to the susceptibility at $T = 0$ comes from the Van Vleck coupling of the ground state to the excited states. At finite temperatures, the Curie term will also contribute due to the thermal population of excited states.

A program has been written in FORTRAN to allow calculations of the eigenvalues, eigenvectors and the transition matrix elements between eigenstates to be made. This program also uses these eigenvalues and eigenvectors to calculate the susceptibility, magnetisation and magnetic specific heat.

1.5 References

[1] K. W. H. Stevens, Proc. Phys. Soc. **65** (1952) 209; Proc. R. Soc. **A214** (1952) 237

[2] M. T. Hutchings, Solid State Phys. **16** (1964) 227

[3] O. Moze, *Handbook of Magnetic Materials Volume 11*, Elsevier Science (1998) 493

[4] H. Bethe, Annalen Physik, **3** (1929) 3

[5] S. K. Chan and D. J. Lam, *The Actinides: Electronic Structure and Related Properties Volume 1*, Academic Press, New York (1974)

[6] K. A. McEwen, *Handbook on the Physics and Chemistry of Rare Earths Volume 1*, Elsevier Science (1978)

[7] W. Matz *et al.*, *Crystalline Electric Field effects in f-electron magnetism*, Plenum Press (1982) 69

[8] J. H. Van Vleck, *The Theory of Electric and Magnetic Susceptibilities*, Oxford University Press (1932)

CHAPTER 2

Neutron Scattering

2.1 Properties of the neutron

Neutron scattering is one of the most powerful tools available with which to look at the properties of condensed matter. It is the intrinsic properties of thermal neutrons (listed below) which make them perfectly suited to condensed matter studies:

mass	1.675×10^{-27} kg
charge	0
spin	½
moment	$-1.913\ \mu_N$

The following relationships between energy E, mass m, velocity v, temperature T, wavevector k, wavelength λ and momentum p can be defined for the neutron:

$$E = \tfrac{1}{2}mv^2 = k_B T$$
$$\lambda = \frac{h}{p} = \frac{h}{mv} = \frac{2\pi}{k}$$

where k_B is the Boltzmann constant and h is the Planck constant. Inserting these values, we obtain the following values for thermal neutrons ($100 < T < 1000$ K):

$$9 \text{ meV} < E < 90 \text{ meV} \quad \text{and} \quad 1 \text{ Å} < \lambda < 3 \text{ Å}$$

Some of the reasons why thermal neutrons are so useful in studying condensed matter systems, especially those in which magnetism is present, are given below:

- Since the neutron has a magnetic moment it will interact with unpaired electrons in magnetic atoms. This enables magnetic structures and dynamics to be directly observed. Neutrons can also be spin polarised which allows further information about the magnetism of a material to be determined.

- Since the neutron is uncharged it can penetrate into the bulk of a material and, more importantly, since there is no Coulomb repulsion from the electron 'cloud' surrounding an atom it is scattered entirely by the nucleus.

- The neutron mass is such that the de Broglie wavelength of thermal neutrons is comparable to the interatomic distances in solids and liquids. This means that interference effects between neutrons scattered from the nuclides can provide information about the structure of the scattering system.

- Thermal neutrons have a kinetic energy which is comparable to many types of excitations in condensed matter. This means that the transfer of energy to or from the neutron can provide information about the dynamics of the scattering system.

Neutrons are usually produced by nuclear reactors or spallation sources. The two methods of production are discussed in Chapter 4, using the ILL reactor and ISIS spallation source as examples.

2.1.1 Comparison with x-rays

It is worth mentioning the differences between neutrons and x-rays which allow neutron scattering to be used advantageously:

- X-rays are scattered by the electron charge density surrounding the atom. Neutrons, however, are scattered entirely by the nucleus, meaning that certain nuclides from which x-rays are only weakly scattered (such as hydrogen) can be observed very easily using neutrons.

- The uncharged nature of neutrons makes them highly penetrating. This means that a wide range of sample environments (e.g. furnaces, cryostats, magnets, pressure cells) can be used without significantly reducing the beam intensity.

- The scattering of x-rays is proportional to the atomic number whereas the neutron scattering length varies from atom to atom. This means that neutrons can be sensitive to light atoms in the presence of heavy atoms.

- The difference in sign for the neutron scattering lengths of certain isotopes (e.g. hydrogen and deuterium) means that isotopic substitution can be used to provide additional information through contrast variation.

- Neutrons can interact directly with unpaired electron spins to provide information about magnetic structures and excitations.

The major disadvantage of neutron scattering compared to x-ray scattering is the much lower intensities available from neutron sources compared to x-ray synchrotrons. This means that large samples must be used which are often difficult to obtain, especially in single crystal form. Samples for neutron experiments are typically required to be 1000 times larger than for a similar x-ray measurement.

2.2 Neutron Scattering Theory

There are many classic texts which describe in detail the theory of neutron scattering, including those by Marshall and Lovesey[1], Squires[2], Lovesey[3] and Jensen and Mackintosh[4]. The equations for nuclear scattering will be derived first, followed by those for magnetic scattering. The relationship between these equations and the actual quantities measured will be discussed.

In order to obtain information from the scattering of neutrons from a sample, it is necessary to measure the neutron *cross-section*. These cross-sections are the quantities actually measured in a scattering experiment. Suppose the scattering process is that as shown in Figure 2.1 in which the incident neutron flux is Φ. The *partial differential cross-section* is defined as:

$$\frac{\mathrm{d}^2\sigma}{\mathrm{d}\Omega \mathrm{d}E_f} = \frac{\left(\begin{array}{c}\text{number of neutrons scattered per second into a small} \\ \text{solid angle } \mathrm{d}\Omega \text{ with final energy between } E_f \text{ and } E_f + \mathrm{d}E_f\end{array}\right)}{\Phi \mathrm{d}\Omega \mathrm{d}E_f}$$

If the final neutron energy is not analysed, the *differential cross-section* is then defined as:

$$\frac{d\sigma}{d\Omega} = \frac{(\text{number of neutrons scattered per second into a small solid angle } \mathrm{d}\Omega)}{\Phi d\Omega}$$

By integrating over all angles, we obtain the *total scattering cross-section*:

$$\sigma_{total} = \frac{(\text{total number of neutrons scattered per second})}{\Phi}$$

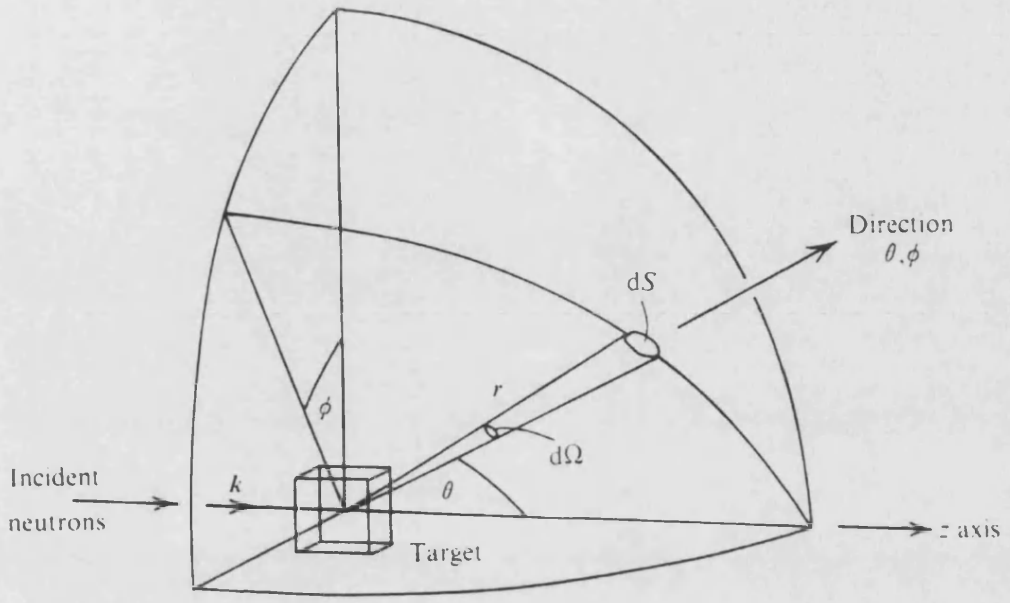

Figure 2.1 Generic scattering diagram for a beam of neutrons being scattered into a solid angle dΩ at an angle of θ,φ

2.2.1 Elastic and inelastic scattering

Elastic scattering occurs when the energies of the incident and scattered neutron are identical and so the magnitude of the scattering is given by the differential cross-section. Inelastic scattering, on the other hand, occurs when the incident neutron gains (or loses) energy through the absorption (or emission) of an excitation. The magnitude of inelastic scattering is therefore obtained by measuring the partial differential cross-section. This cross-section is measured as a function of *momentum transfer* and *energy transfer*, which are defined as:

$$\hbar\mathbf{Q} = \hbar(\mathbf{k}_i - \mathbf{k}_f) \qquad \text{and} \qquad \hbar\omega = E_i - E_f = \frac{\hbar^2}{2m}\left(k_i^2 - k_f^2\right)$$

2.2.2 Nuclear scattering

The derivations of nuclear and magnetic cross-sections both begin with a general description of the neutron-sample interaction. Consider a neutron scattered from an initial state (wavevector $\mathbf{k}_i$ and spin σ_i) to a final state (wavevector $\mathbf{k}_f$ and spin σ_f) by an interaction potential *V*. The probability of such a scattering event is given by Fermi's Golden Rule as:

$$\frac{d^2\sigma}{d\Omega dE_f} = \frac{k_f}{k_i}\left(\frac{m}{2\pi\hbar^2}\right)^2 \sum_{\lambda_i,\lambda_f} p_{\lambda_i} \sum_{\sigma_i,\sigma_f} p_{\sigma_i} \left|\left\langle \mathbf{k}_f \sigma_f \lambda_f \right| V \left| \mathbf{k}_i \sigma_i \lambda_i \right\rangle\right|^2 \delta(\hbar\omega + E_{\lambda_i} - E_{\lambda_f})$$

where λ_i, λ_f denote the initial and final state of the sample and $p_{\lambda_i}, p_{\sigma_i}$ are the occupation probabilities of the initial states. The terms $\left|\mathbf{k}_i \sigma_i \lambda_i\right\rangle$ and $\left|\mathbf{k}_f \sigma_f \lambda_f\right\rangle$ are the initial and final wavefunctions of the complete scattering process. The delta function is simply energy conservation, i.e. the difference in energy between the final and initial states must be equal to the energy transferred to or from the neutron.

In order to obtain the form of the neutron-nucleus interaction V_N we assume that it is very short ranged, i.e. $V_N(\mathbf{r}) \propto \delta(\mathbf{r})$. This is valid since the range of the nuclear force (~1 fm) is much smaller than the neutron wavelength. Calculations of the coefficient then give:

$$V_N(\mathbf{r}) = \frac{2\pi\hbar^2}{m} b\delta(\mathbf{r})$$

where *b* is known as the scattering length which varies with element, isotope and nuclear spin. Tables of scattering lengths for all of the elements are available in many places, including Marshall and Lovesey[1], Lovesey[3] and the NIST website (http://www.ncnr.nist.gov/resources/n-lengths/).

For a scattering system containing j nuclei with scattering lengths b_j the partial differential cross-section (for unpolarised neutrons) becomes:

$$\frac{d^2\sigma}{d\Omega dE_f} = \frac{k_f}{k_i} \sum_{\lambda_i,\lambda_f} p_{\lambda_i} \left| \left\langle \lambda_f \left| \sum_j b_j e^{i\mathbf{Q}\cdot\mathbf{R}_j} \right| \lambda_i \right\rangle \right|^2 \delta(\hbar\omega + E_{\lambda_i} - E_{\lambda_f})$$

after integrating over the space co-ordinates of the neutron.

The delta function for energy can be rewritten as an integral with respect to time and the $\mathbf{R}_j$ operators can be converted into time-dependent Heisenberg operators $\mathbf{R}_j(t)$. Then, after integrating over the λ states, the partial differential cross-section can be expressed as the sum of *coherent* and *incoherent* inelastic scattering cross-sections:

$$\frac{d^2\sigma}{d\Omega dE_f} = \left(\frac{d^2\sigma}{d\Omega dE_f}\right)_{coh} + \left(\frac{d^2\sigma}{d\Omega dE_f}\right)_{inc}$$

where $$\left(\frac{d^2\sigma}{d\Omega dE_f}\right)_{coh} = \left(\overline{b}^2\right)\frac{k_f}{k_i}\frac{1}{2\pi\hbar}\sum_{jj'}\int_{-\infty}^{\infty}\left\langle e^{-i\kappa\cdot\mathbf{R}_{j'}(0)} e^{i\kappa\cdot\mathbf{R}_j(t)}\right\rangle e^{-i\omega t}\,dt$$

and $$\left(\frac{d^2\sigma}{d\Omega dE_f}\right)_{inc} = \left(\overline{b^2} - \overline{b}^2\right)\frac{k_f}{k_i}\frac{1}{2\pi\hbar}\sum_{j}\int_{-\infty}^{\infty}\left\langle e^{-i\kappa\cdot\mathbf{R}_j(0)} e^{i\kappa\cdot\mathbf{R}_j(t)}\right\rangle e^{-i\omega t}\,dt$$

It can be seen that incoherent scattering depends only on the correlation between the *same* nucleus at different times. Coherent scattering, however, also depends on the correlation between *different* nuclei at different times. Coherent scattering therefore gives interference effects.

Actual systems consist of different nuclei and therefore different scattering lengths. The coherent scattering is that which would be obtained if all the scattering lengths were equal to the ensemble average, $\bar{b}$. The term which must be added to this to regain the actual scattering is the incoherent scattering.

From the coherent nuclear scattering cross-section we can obtain the coherent elastic nuclear scattering cross-section for a non-Bravais crystal (i.e. one in which there is more than one atom per unit cell):

$$\left(\frac{d\sigma}{d\Omega}\right)_{coh} = N_N \frac{(2\pi)^3}{v_N} \sum_{\tau} [F_N(\mathbf{Q})]^2 \delta(\mathbf{Q}-\tau)$$

where the N_N nuclear unit cells of volume v_N each contain d atoms at positions $\mathbf{d}$ and $\boldsymbol{\tau}$ is a vector in the reciprocal lattice. It can be seen that scattering occurs only when $\mathbf{Q} = \mathbf{k}_i - \mathbf{k}_f = \boldsymbol{\tau}$ which is the same as Bragg's Law, i.e. coherent elastic scattering of neutrons is simply Bragg scattering.

The *nuclear structure factor* in the above equation is given by:

$$F_N(\kappa) = \sum_d \bar{b}_d e^{-W(\mathbf{Q})} e^{i\kappa\cdot\mathbf{d}}$$

where the exponential term, $e^{-W(\mathbf{Q})}$, is known as the *Debye-Waller factor.* This factor is due to the thermal motion of atoms from their equilibrium positions and results in a diminishing scattering intensity with increasing $\mathbf{Q}$.

2.2.3 Magnetic scattering

The magnetic field generated by an electron with spin **s** and moving with momentum **p** is given, at a point **R** away from the electron, by the sum of the spin and orbital contributions:

$$\mathbf{B} = \mathbf{B}_S + \mathbf{B}_L = \frac{\mu_0}{4\pi}\left[\left(\nabla \times \frac{\boldsymbol{\mu}_e \times \hat{\mathbf{R}}}{R^2}\right) + \left(\frac{-2\mu_B}{\hbar}\frac{\mathbf{p}\times\hat{\mathbf{R}}}{R^2}\right)\right]$$

where $\mu_e = -2\mu_B \mathbf{s}$ is the electron magnetic dipole moment. The interaction potential of a neutron in this field is given by:

$$V = -\boldsymbol{\mu}_n \cdot \mathbf{B} = -\frac{\mu_0(\gamma\mu_N)(2\mu_B)}{4\pi}\boldsymbol{\sigma}\cdot\left[\left(\nabla\times\frac{\mathbf{s}\times\hat{\mathbf{R}}}{R^2}\right) + \left(\frac{1}{\hbar}\frac{\mathbf{p}\times\hat{\mathbf{R}}}{R^2}\right)\right]$$

where $\boldsymbol{\mu}_n = -\gamma\mu_N\boldsymbol{\sigma}$ is the neutron magnetic dipole moment, μ_N is the nuclear magneton, $\gamma = 1.913$ is the gyromagnetic ratio and $\boldsymbol{\sigma}$ is the neutron Pauli spin matrix.

The magnetic scattering cross-section for unpolarised neutrons can then be derived:

$$\frac{d^2\sigma}{d\Omega dE_f} = \frac{k_f}{k_i}(\gamma r_e)^2 \sum_{\lambda_i,\lambda_f} p_{\lambda_i} \langle\lambda_i|\sigma\cdot\mathbf{M}_\perp^*|\lambda_f\rangle\langle\lambda_f|\sigma\cdot\mathbf{M}_\perp|\lambda_i\rangle\delta(\hbar\omega + E_i - E_f)$$

where the *magnetic interaction operator* is defined for an electron at $\mathbf{r}_j$ as:

$$\mathbf{M}_\perp(\mathbf{Q}) = \sum_j\left[\hat{\mathbf{Q}}\times(\mathbf{s}_j\times\hat{\mathbf{Q}}) + \frac{i}{\hbar Q}(\mathbf{p}_j\times\hat{\mathbf{Q}})\right]\exp i(\mathbf{Q}\cdot\mathbf{r}_j)$$

In the dipole approximation, which is valid for case where $|\mathbf{Q}|^{-1}$ is much greater than the mean radius of the orbital wavefunctions of the unpaired electrons, the magnetic scattering cross-section can be written in terms of the total angular momentum:

$$\frac{d^2\sigma}{d\Omega dE_f} = \frac{k_f}{k_i}(\gamma r_e)^2\left[\frac{1}{2}gF_M(\mathbf{Q})\right]^2 \sum_{\lambda_i,\lambda_f} p_{\lambda_i} \sum_{i,j} \left\langle \lambda_i \left| (\mathbf{J}_\alpha)_j \right| \lambda_f \right\rangle \left\langle \lambda_f \left| (\mathbf{J}^*_\beta)_j \right| \lambda_i \right\rangle \times \sum_{\alpha,\beta} \left(\delta_{\alpha\beta} - \hat{Q}_\alpha \hat{Q}_\beta\right) \exp i\mathbf{Q}\cdot(\mathbf{r}_i - \mathbf{r}_j)\, \delta(\hbar\omega + E_i - E_f)$$

where $\alpha, \beta = x, y, z$ and the *magnetic form factor*, $F_M(\mathbf{Q})$, is defined as the Fourier transform of the magnetisation density of unpaired electrons. Integration over energy then gives the coherent elastic magnetic cross-section:

$$\left(\frac{d\sigma}{d\Omega}\right)_{coh} = (\gamma r_0)^2 N_M \frac{(2\pi)^3}{v_M} e^{-2W(\mathbf{Q})} \sum_{\tau} \left[\frac{1}{2}gF_M(\mathbf{Q})\right]^2 \delta(\mathbf{Q} - \tau) \times \sum_{\alpha\beta} \left(\delta_{\alpha\beta} - \hat{Q}_\alpha \hat{Q}_\beta\right) \left\langle J^o_\alpha \right\rangle \left\langle J^d_\beta \right\rangle$$

where the N_M magnetic unit cells each contain d atoms in a volume v_M and $\boldsymbol{\tau}$ is a vector in the reciprocal lattice.

By using the integral representation of the δ-function, the magnetic neutron scattering cross-section may be written[5] in terms of the scattering function, $S(\mathbf{Q}, \omega)$:

$$\frac{d^2\sigma}{d\Omega dE_f} = \frac{k_f}{k_i}(\gamma r_e)^2\left[\frac{1}{2}gf(\mathbf{Q})\right]^2 e^{-2W(\mathbf{Q})} \sum_{\alpha,\beta} \left(\delta_{\alpha\beta} - \hat{Q}_\alpha \hat{Q}_\beta\right) S_{\alpha,\beta}(\mathbf{Q}, \omega)$$

where the Van Hove scattering function $S_{\alpha\beta}(\mathbf{Q}, \omega)$ is the Fourier transform of the magnetic correlation function, $\left\langle J_\alpha(\mathbf{Q}, t)\, J^*_\beta(\mathbf{Q}, t) \right\rangle$.

It is assumed that the probability of a transition between any two states in a system is the same in both directions. Then, the *principle of detailed balance* states that:

$$S(\mathbf{Q},\omega) = \exp\left(\frac{\hbar\omega}{k_B T}\right) S(-\mathbf{Q},-\omega)$$

since the probability of the system being initially in the higher energy state is a factor of $\exp\left(\frac{\hbar\omega}{k_B T}\right)$ lower than the probability of it being in the lower energy state.

2.2.4 Dynamical susceptibility

Linear response theory is a method of "analysing the dynamical properties of a condensed matter system close to thermal equilibrium"[4]. It shall be used to relate the magnetic susceptibility to the neutron scattering function. Consider the *dynamical susceptibility* which describes the dynamics of magnetic moments and is defined via:

$$M_\alpha(\mathbf{Q},\omega) = \sum_\beta \chi_{\alpha\beta}(\mathbf{Q},\omega) H_\beta(\mathbf{Q},\omega)$$

Using the Kramers-Kronig relationship which relates the real and imaginary components of $\chi(\mathbf{Q},\omega)$, the principle of detailed balance and by applying linear response theory, we obtain[2] the *fluctuation-dissipation theorem*:

$$S(\mathbf{Q},\omega) = \left[\frac{2\hbar}{1-\exp\left(-\frac{\hbar\omega}{k_B T}\right)}\right] \chi''(\mathbf{Q},\omega)$$

Thus, using this expression, *comparisons between the measured neutron cross-section and calculations of the dynamical susceptibility can be made directly.*

The *random-phase approximation*, which assumes that the fluctuations of the angular momentum vectors away from their thermal averages are small and uncorrelated, results in the *MF-RPA dynamical susceptibility*:

$$\chi''(\mathbf{Q},\omega) = \frac{\chi_0''(\omega)}{1-\chi_0''(\omega)J_{ex}(\mathbf{Q})}$$

where $\chi_0''(\omega) = C/T$ is the non-interacting susceptibility derived in Section 1.3.1 using mean field theory.

2.3 References

[1] W. Marshall and S. W. Lovesey, *Theory of Thermal Neutron Scattering*, Clarendon Press, Oxford (1971)

[2] G. Squires, *Thermal Neutron Scattering*, Cambridge University Press (1978)

[3] S. W. Lovesey, *Theory of Neutron Scattering from Condensed Matter*, Oxford University Press (1984)

[4] J. Jensen and A. R. Mackintosh, *Rare Earth Magnetism: Structures and Excitations*, Clarendon Press, Oxford (1991)

[5] L. Van Hove, Phys. Rev. **95** (1954) 249

CHAPTER 3

Literature Review

Due to the extremely localised nature of the $4f$ electrons in rare-earth intermetallics and the resulting high value of the effective magnetic moment, there are many examples of crystal field excitations in such compounds. In contrast, the $5f$ electrons in uranium intermetallics are usually delocalised and so the observation of clearly defined crystal field excitations is relatively rare.

In this chapter, comparisons and contrasts between rare-earth and actinide electronic and magnetic behaviour will be made. Typical signatures of localised magnetism and the techniques available to detect such properties will be discussed. Finally, a literature review of the small number of localised uranium intermetallics will be presented.

3.1 Lanthanide and actinide magnetism

In the lanthanides, the $4f$ electrons are tightly bound to the core of the ion, so the interaction between them and their environment is weak. Consequently, the ground state magnetic moments are usually close to the free-ion values calculated in the *LS* coupling scheme. Differences between calculated and experimental moments can often be attributed to the interaction between the aspherical $4f$ charge cloud and the surrounding charge distribution. This interaction causes CEF effects and also leads to the single-ion magnetocrystalline anisotropy of the lanthanide magnetic moments. This anisotropy causes the $4f$ magnetic moments to align preferentially with respect to the crystallographic axes.

The outermost electrons of the ion, i.e. the $6s6p5d$ electrons, form the conduction band leaving the ion in a tripositive state. The properties of this band therefore influence the magnetic properties of the material. The indirect RKKY interaction responsible for coupling the $4f$ orbitals is a long range interaction and is often oscillatory, which gives rise to periodic spin structures such as helical and conical.

In the actinides, the wavefunctions of $5f$ electrons extend much further than the $4f$ wavefunctions, so they interact much more strongly with their environment. Consequently, the $5f$ electrons in actinides are usually delocalised and considerable hybridisation occurs between them and the valence electrons in neighbouring atoms. In these delocalised cases, the $5f$ states form a narrow band meaning that the magnetic moments due to the itinerant $5f$ electrons are much smaller than the free-ion values. So, in the vast majority of uranium intermetallics, no crystal field excitations are observed by inelastic neutron scattering and instead a broad quasielastic response is usually seen.

In 1970, Hill recognised that in compounds with a small uranium-uranium spacing the ground state is often superconducting and non-magnetic. Conversely, a large uranium-uranium separation often leads to a magnetic, non-superconducting ground state. The critical separation between these two regimes (the Hill limit) is considered to be around 3.5 Å. So, for actinide-actinide separations below this value, itinerant behaviour and a non-magnetic ground state is expected whereas, for separations above this value, localised magnetism often results.

Obviously there are exceptions to this primitive rule, such as UNi_2 which orders magnetically despite having $d_{U\text{-}U} \approx 3.1$ Å. Exceptions for compounds with $d_{U\text{-}U}$ greater than the Hill limit are numerous due to the $5f$-ligand hybridisation which causes delocalisation of the f electrons and can make compounds with negligible direct $5f$-$5f$ overlap non-magnetic. Since the hybridisation process conserves spin information, however, it can also lead to an indirect exchange coupling. There is therefore a competition between strong hybridisation, which suppresses magnetic moments, and weak hybridisation which weakly couples magnetic moments.

3.2 Signatures of localised and itinerant behaviour

An effective magnetic moment close to the free ion value indicates that the *f* electrons are well localised. Itinerant *f* electron systems often show an enhanced γ coefficient of the low temperature specific heat. The integrated magnetic contribution to C/T gives the magnetic entropy, which is usually only a fraction of $R\ln 2$ in the itinerant regime.

Indirect observations of localised behaviour may be obtained using techniques such as NMR, Mössbauer, electrical conductivity and resistivity. Direct observations, on the other hand, come from specific heat, susceptibility, thermal expansion, magnetostriction and high field magnetisation measurements. The observation of crystal field excitations using inelastic neutron scattering gives the strongest indication that the *f* electrons in a material are localised. However, *clear CEF excitations are rare in uranium-based intermetallics.*

3.3 UTX, UT_2X, UT_2X_2 and U_2T_2X compounds

Comprehensive reviews of the UTX, UT_2X and U_2T_2X series of compounds have been assembled by Sechovsky and Havela in Volume 11 of the Handbook of Magnetic Materials (Elsevier, 1998). The following sections will summarise the relevant information in regards to localised magnetism in these series. The compounds studied in this thesis will be mentioned briefly, however a more detailed literature review will be presented in each experimental chapter.

3.3.1 UTX compounds

There are almost 50 isostoichiometric compounds in the UTX series. The crystal structure is determined primarily by the transition metal component, T, which

comes from the second half of the 3*d*, 4*d* or 5*d* series. The systematic occurrence of crystal structures is shown in Table 3.1 where structures in brackets are the ordered derivative of the preceding structure. Most UTX compounds crystallise in the ordered ZrNiAl and TiNiSi structures and most exhibit itinerant electron behaviour. In fact, URhSi is an outstanding example of itinerant 5*f* magnetism in which the magnetic moments are extremely small but are strongly anisotropic.

Compounds with nearly (Ni, Pd, Pt) or fully (Cu, Ag, Au) occupied *d* electron states usually form in the $CaIn_2$ or ordered GaGeLi structure. As the *d* electron states are populated, the 5*f*-*d* hybridisation is reduced which leads to more localised 5*f* states. The largest uranium spacings in the series are towards the right hand side and the $CaIn_2$ and GaGeLi structures typically have $d_{U\text{-}U} = c/2 \approx$ 3.6 Å along the c-axis whilst the uranium spacing in the basal plane is significantly larger.

Mn	Fe	Co	Ni	Cu
Tc	Ru	Rh	Pd	Ag
Re	Os	Ir	Pt	Au
Hexagonal $MgZn_2$	Hexagonal Fe_2P (ZrNiAl)		Hexagonal $CaIn_2$ (GaGeLi)	
	Orthorhombic $CeCu_2$ (TiNiSi)		Cubic MgAgAs	

Table 3.1 Systematics of the crystal structure of UTX compounds as the transition metal, T, is changed.

UPdSn is one of these GaGeLi structures and has an effective magnetic moment of $\mu_{eff} = 3.31\mu_B$, a low value of the specific heat coefficient $\gamma = 5$ mJ/mol/K^2 and a high magnetic entropy $\Delta S = 1.1R\ln 2$. These values, together with a uranium spacing above the Hill limit, all suggest that the 5*f* electrons are localised. Specific heat measurements on UCuSn show a similar behaviour to UPdSn and the large magnetic entropy changes around T_N are indicative of *f* electron localisation.

The three cubic MgAgAs compounds UNiSn, UPtSn and URhSb have effective moments of 3.15, 3.55 and 3.25 μ_B, respectively, which indicate localised moment magnetism at high temperatures. UNiSn has an interesting phase transition at T_N = 43 K above which it is a semiconducting paramagnet and below which it is a metallic antiferromagnet[1]. The $d_{U\text{-}U}$ separation of 4.2 Å is well above the Hill limit. The low value of γ = 18 mJ/mol/K^2 and a magnetic entropy of almost Rln2 at T = 43 K suggest localised behaviour and UNiSn indeed shows clear CEF excitations.

The $5f^2$ configuration is split into a singlet, a doublet and two triplets by the cubic crystal field. From susceptibility and heat capacity measurements, Aoki *et al.* proposed[2] a crystal field scheme for UNiSn with levels at 16, 45 and 270 meV. However, inelastic neutron scattering measurements[3] have since determined that the upper limit for the CEF energy level scheme is around 40 meV. X-ray diffraction[4] has also shown that the AFM ordering splits the ground state which induces ferroquadrupolar order which, in turn, triggers a cubic to tetragonal distortion.

3.3.2 UT_2X compounds

Most of the UT_2X series crystallises in the cubic $MnCu_2$ structure, although some form in the hexagonal $ZrPt_2Al$ structure. The cubic compounds are related to the Heusler 1-1-1 compounds but with the extra transition metal atoms filling in the vacancies. This increases the 5*f*-*d* hybridisation and so most of these compounds are paramagnets. As an example, UNi_2Sn is non-magnetic despite the fact that the UNiSn and U_2Ni_2Sn compounds order magnetically.

Although $d_{U\text{-}U}$ and μ_{eff} are often large, the hybridisation usually causes these compounds to tend towards itinerant *f* electron behaviour. An exception to this trend is UCu_2Sn which has the $ZrPt_2Al$ structure. It exhibits a sharp λ-type

anomaly at T_N = 16.5 K which contains an entropy of Rln2, suggestive of localised electronic states. The difference in properties of UPt_2Sn has been attributed to stronger 5*f*-*d* hybridisation due to a 3.5 % reduction in the $d_{U\text{-}T}$ distance compared to UCu_2Sn.

3.3.3 UT_2X_2 compounds

From this series it is the UT_2Si_2 and UT_2Ge_2 families of compound which have been most intensively studied. A common feature of the series is a strong uniaxial anisotropy of the susceptibility in which the *c*-axis response is much greater than the *a*- or *b*-axis response. The magnetic ordering temperatures have been found to be related to the *f*-*d* hybridisation.

Out of these compounds, UNi_2Si_2 has attracted attention due to its rich phase diagram and URu_2Si_2 due to the coexistence of the antiferromagnetic ordering of weak magnetic moments with superconductivity at low temperatures. Some of these compounds have had CEF models proposed to explain their magnetic properties, but crystal field excitations have only been clearly observed in UPt_2Si_2 for which a CEF level scheme has been proposed[5].

UPt_2Si_2 orders antiferromagnetically below T_N = 35 K which is accompanied by a strong uniaxial magnetocrystalline anisotropy. This can be seen in the susceptibility and high-field magnetisation curves. The estimated anisotropy field of 50 T is low compared to other magnetic silicides.

UCo_2P_2 has an effective moment close to that for free U^{3+} or U^{4+} ions which points to possible localised 5*f* states. UCu_2P_2 exhibits attributes of a local moment system and the high temperature susceptibility of has been interpreted in terms of a CEF model with molecular field[6].

3.3.4 U_2T_2X compounds

Hybridisation effects obviously play an important role in the U_2T_2X series since, although the $d_{U\text{-}U}$ distance is usually just above 3.5 Å, the *f* electron states exhibit itinerant behaviour in almost all of these compounds.

3.3.5 Other localised 5f materials

As has already been mentioned, there are only a few uranium-based intermetallics in which the *f* electrons are known to be localised by the observation of clear crystal field excitations. Among these compounds, the most well known example is UPd_3 which shows sharp CEF excitations in the 1-20 meV range consistent with a $5f^2$ configuration[7,8]. Neutron diffraction, ultrasonic attenuation and elastic constant measurements have established[9,10] the existence of antiferroquadrupolar (AFQ) order below T_0 = 7.6 K. Resonant x-ray scattering has shown that the AFQ ordering is on the uranium sites and that the quasi-cubic sites order with a $Q_{x^2-y^2}$ order parameter.

Doping with Y on the U sites increases the hybridisation between the $5f$ electrons and the conduction electrons. For $U_xY_{1-x}Pd_3$ with x = 0.45, crystal field excitations are observed at 5 and 40 meV. As the uranium concentration is reduced, these excitations becoming weaker and broader and, at x = 0.2, non-Fermi liquid behaviour is observed[11].

The $U(Pd_{1-x}Pt_x)_3$ series has also been investigated[12] to follow the transition between localised UPd_3 and the itinerant, heavy fermion UPt_3. In contrast to pure UPt_3 which exhibits antiferromagnetic fluctuations, the x = 0.95 compound exhibits long-range antiferromagnetism below T_N = 6.4 K. In this doped compound, a damped spin wave is visible below T_N which exhibits dispersion

along the c^* direction but not along the a^* direction. This indicates a strong coupling between uranium moments along the *c*-axis but not in the basal plane.

Photoelectron spectroscopy[13] of $U_3Ni_3Sb_4$ suggests an itinerant behaviour of the 5*f* states. Inelastic neutron scattering[14], however, has revealed clear CEF excitations below 60 meV, an intermultiplet transition at 370 meV and a lack of quasielastic scattering which is more indicative of localised 5*f* electrons. Similar features were observed for $U_3Pt_3Sb_4$ but a broad quasielastic response and no distinct CEF excitations were observed for $U_3Cu_3Sn_4$ which suggests an itinerant nature of the *f* electron states in this compound.

The UNi_2Al_3 and UPd_2Al_3 compounds are both heavy fermion superconductors which order antiferromagnetically at low temperatures. UPd_2Al_3 has a γ value of 140 mJ/mol/K^2 and an effective moment of $\mu_{eff} = 3.2\,\mu_B$ and the magnetic ordering coexists with the superconductivity. It has therefore been proposed[15] that two subsystems exist; a local 5*f* moment one responsible for the magnetic features and a heavy fermion one responsible for superconductivity and the enhanced γ value. Inelastic neutron scattering found possible evidence for crystal field excitations (a signature of local moments) on top of a quasielastic (itinerant *f* electron type) response[16]. The 5*f*-*d* hybridisation is stronger in UNi_2Al_3 which makes the 5*f* states more delocalised in this compound.

$U_2Rh_3Si_5$ orders antiferromagnetically at T_N = 26 K at which point the susceptibility shows a sharp cusp. The associated magnetic entropy is around *R*ln2, so it has been suggested that this compound has a ground state which undergoes an exchange-induced magnetic ordering.

3.4 References

[1] H. Fujii *et al.*, J. Phys. Soc. Japan, **58** (1989) 2495

[2] Y. Aoki *et al.*, Phys. Rev. B, **47** (1993) 15060

[3] K. A. McEwen *et al.*, Physica B, **281 & 282** (2000) 600

[4] T. Akazawa *et al.*, J. Phys. Soc. Japan, **65** (1996) 3661

[5] R. A. Steeman *et al.*, J. Mag. Mag. Mat, **76-77** (1988) 435

[6] D. Kaczorowski, J. Mag. Mag. Mat, **76-77** (1988) 366

[7] W. J. L. Buyers and T.M. Holden, Handbook *on the Physics and Chemistry of the Actinides Volume 2*, Elsevier Science, Amsterdam (1985) 239

[8] K. A. McEwen *et al.*, Physica B **186-188** (1993) 670

[9] K. A. McEwen *et al.*, J. Mag. Mag. Mat, **177-181** (1998) 37

[10] N. Lingg *et al.*, Phys. Rev. B, **60** (1999) R8430

[11] A. Martin-Martin, PhD thesis, University of London (2000)

[12] M. J. Bull *et al.*, Phys. Rev. B, **57** (1998) 3850

[13] T. Takabatake *et al.*, Solid State Comm, **81** (1992) 433

[14] B. D. Rainford *et al.*, Physica B, **224** (1996) 231

[15] R. Feyerherm *et al.*, Phys. Rev. Lett. **73** (1994) 1849

[16] A. Krimmel *et al.*, J. Phys. Cond. Mat. **8** (1996) 1677

CHAPTER 4

Experimental Techniques

4.1 Sample preparation

The $U_3Pd_{20}Si_6$, UCu_2Sn and U_2Co_2Sn polycrystalline samples were all grown by the arc-melting method; the former two using a Bühler arc furnace at University College London and the latter by Dave Fort at the University of Birmingham. The required amount of uranium was cut from a large disc of (99.9% purity) depleted uranium from the Ames Laboratory (USA) using a spark eroder. The surface was then cleared of any oxide layers by etching in a diluted nitric acid solution and the final amount of uranium weighed. The necessary amounts of high purity (99.999%) constituent elements in the form of powder, wire or thin sheets were then weighed out and placed into a copper crucible, along with a zirconium getter. The chamber was put under vacuum, flushed with high purity Argon and then purged. This procedure was repeated three times and a final pressure of 300 mbar of Argon was left in the chamber.

A voltage was applied between a tungsten tip and the copper crucible, to create a plasma arc. The tip was then manipulated so that the arc came into contact with the getter for 1 minute. Since zirconium oxide has a dull surface, air leaks in the chamber were checked for by noting whether the surface of the getter remained shiny after this procedure. The plasma arc was created again and moved slowly onto the constituent elements for around 10 seconds. The heat generated melted the elements together to form a single 'button'. To ensure sample homogeneity, each button was flipped and re-melted up to three times. Depending on the relative vapour pressures of the constituent materials, fractional percentages of the elements were added to compensate for loss through evaporation.

The UPdSn sample was grown, in the form of six small single crystals, at the University of Amsterdam by Heinz Nakotte and colleagues. The PrNiSn and NdNiSn single crystals were grown by Dave Fort in the University of Birmingham in a tri-arc furnace. The PrNiSn crystal used in the present work is the same as that used in the experiments by Eamonn Beirne (PhD Thesis, University College London, 2002).

4.2 SQUID magnetometer

The susceptibility and magnetisation measurements were performed using a Quantum Design SQUID magnetometer. This type of magnetometer uses the *Superconducting QUantum Interference Device* (SQUID) as a kind of picovoltmeter. This is achieved through use of the Meissner effect which prevents magnetic flux from entering a superconductor, and the Josephson effect in which superconducting electrons are able to tunnel through a thin insulating layer separating two superconductors.

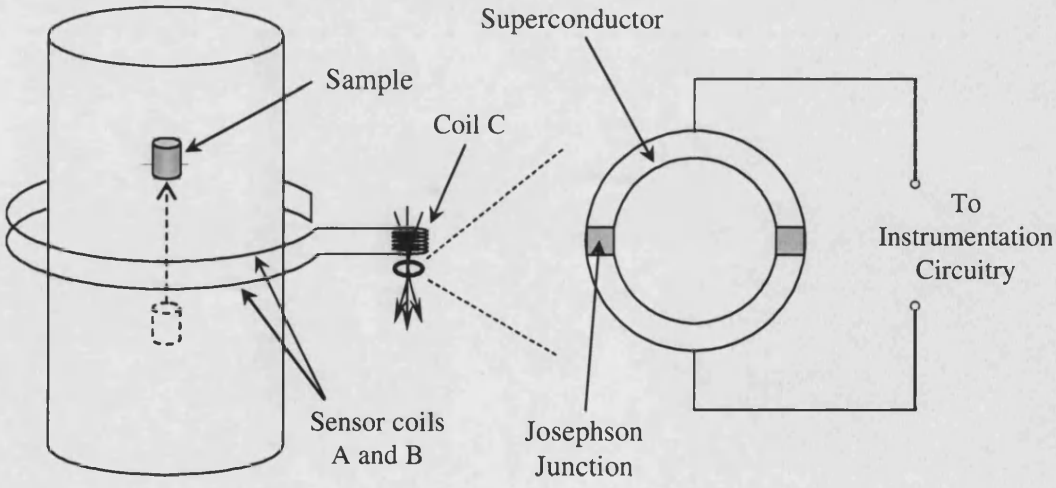

Figure 4.1 Schematic diagram of the SQUID magnetometer.

The sample is raised through two counter-wound sensor coils (A and B) and its magnetic moment induces a current in the coils. This induced current is then passed through another set of tightly wound coils (C) to generate a magnetic flux which threads through the superconducting SQUID ring (as shown in Figure 4.1). If the ring was completely superconducting the flux through it could not change. However, the value of the supercurrent flowing through the ring is restricted by the presence of the weak links. Therefore, once the supercurrent exceeds this critical value, a flux quantum can enter or leave the ring.

So as the magnetic flux due to the sample changes, the output voltage across the SQUID changes and is sent to a series of radio frequency circuits. This instrumentation circuitry allows magnetic fields to be measured to an accuracy of a fraction of a flux quantum.

4.3 Neutron Sources and Spectrometers

There are two main types of spectrometer used at neutron sources; triple-axis and time-of-flight spectrometers, each with their own advantages and disadvantages. Typical experimental setups are shown in Figure 4.2.

Triple-axis spectrometers are designed to look at specific points in $(\mathbf{Q}, \omega)$ space. They are therefore ideally suited to making point-by-point scans along lines of constant energy or constant wavevector, which makes them perfect for determining dispersion relations in single crystals. The main advantage of triple-axis spectrometers is their flexibility since the resolution, collimation and choice of incident energy can be finely tuned to meet experimental requirements. Disadvantages include slow data acquisition and the problem of the fast neutron background from uranium based samples.

Time-of-flight spectrometers are designed to survey wide areas of $(\mathbf{Q},\omega)$ space. The range of available incident energies is wide and the resolution can be controlled by changing the type or speed of the chopper. The main benefit of the time-of-flight technique is that there is no need to select the energy or direction of the detected neutrons, meaning that detector banks with large solid angles can be used to detect a large percentage of the scattered neutrons. Using software, cuts through regions of constant energy or wavevector can be made. At pulsed sources, where these spectrometers are used, the fast neutron background can be eliminated by gating out neutrons that arrive too soon after the initial pulse.

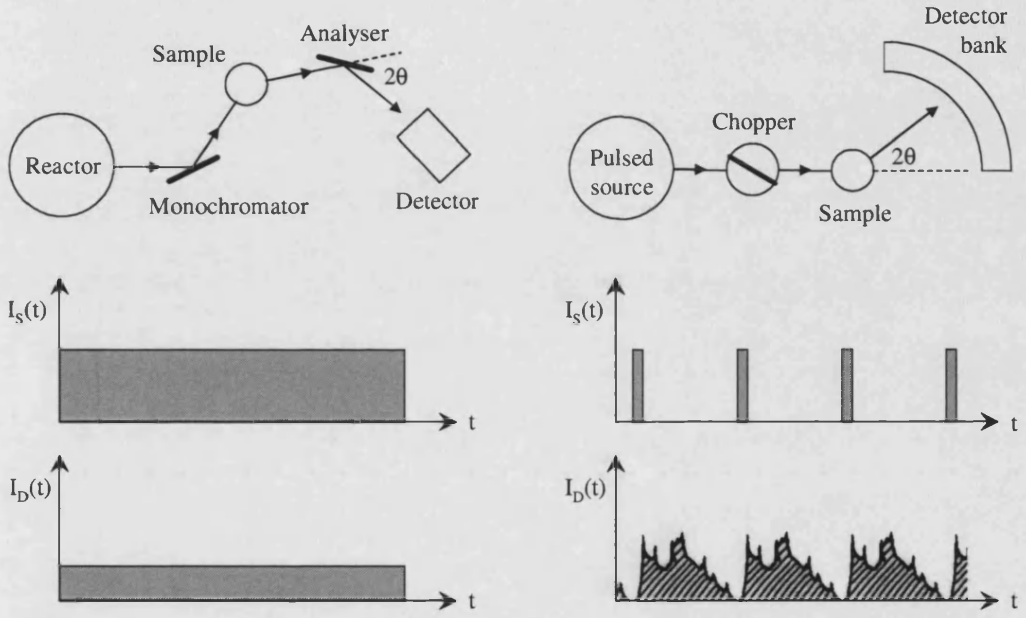

Figure 4.2 Schematic of a typical triple-axis (left) and time-of-flight (right) experiment. For both, the variation with time of flux at the sample position (top) and at the detector (bottom) is shown.

4.3.1 Triple-axis spectrometers: V2

The V2 triple-axis spectrometer is situated in the BER-II reactor at the Berlin Neutron Scattering Centre (BENSC) in Germany[1]. Neutrons produced from the fission process in the 10 MW reactor core are moderated by light water and are then directed down a guide tube to the experimental apparatus (see figure 4.3). A triple-axis spectrometer is so named because of the axes about which the monochromator crystal, sample and analyser crystal rotate.

When the "white beam" of neutrons from the reactor hits the monochromator crystal, only those neutrons satisfying the correct Bragg condition are diffracted towards the sample. Thus, by varying the angle of this crystal, the energy of the neutrons incident on the sample can be selected. The analyser crystal works in the same way to ensure that only neutrons of the required energy are detected. They are both made from pyrolitic graphite (002) strips and can be curved to focus the beam. The collimators and diaphragms are used to optimise the signal-to-noise ratio and a cooled Be filter is used to eliminate second order $(\lambda/2)$ contamination.

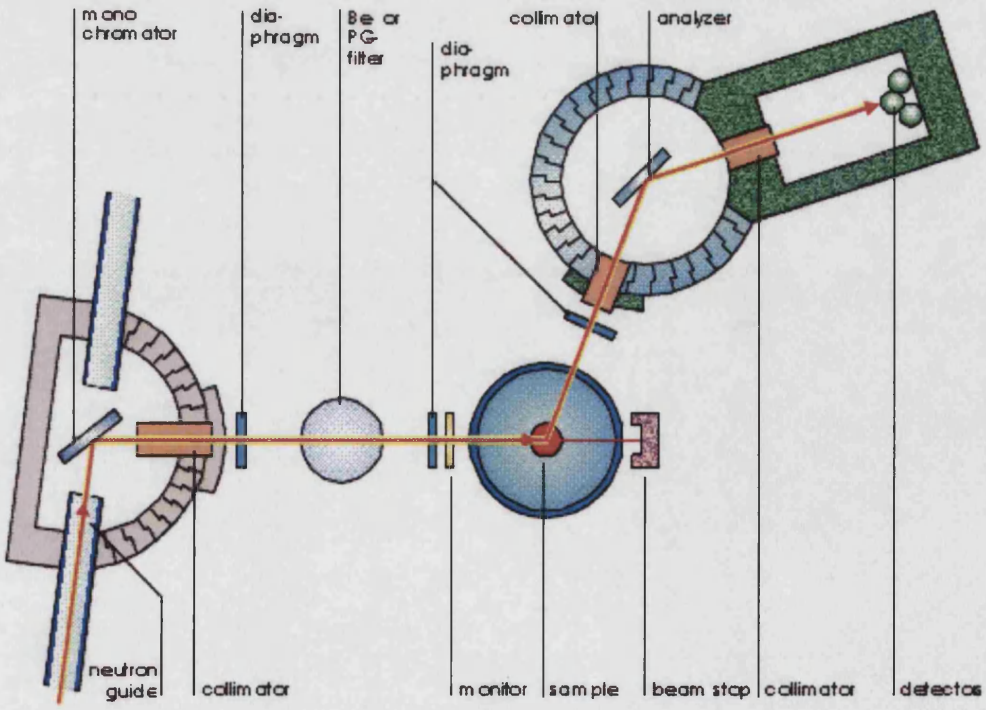

Figure 4.3 Schematic layout of the V2 triple-axis spectrometer taken from the HMI website.

4.3.2 Time of flight spectrometers: HET

The HET (High Energy Transfer) spectrometer is situated at the ISIS facility in the UK[2], which is the world's most powerful pulsed spallation source. A high energy (800 MeV) bunch of protons produced in a synchrotron impacts onto a heavy metal (tantalum) target with a power of 160 kW, leaving some of the nuclei within the target in a highly excited state. These unstable nuclei evaporate nucleons (mainly neutrons), some of which leave the target, while others go on to trigger further reactions.

Each high-energy proton delivered to the target produces approximately 15 neutrons resulting in a flux of approximately 2×10^{16} neutrons per second. These neutrons are too high in energy to be used experimentally so they must be slowed down to usable energies. This is achieved by using a 316 K H_2O moderator, since hydrogen has a high scattering cross section.

The neutrons travel down an 11.82 m flight path to the sample position, where they are scattered into a set of detector banks (shown in Figure 4.4). At low scattering angles, from 2.6° to 7.2°, four detector arms are arranged at 90° to each other at a distance of 4 m from the sample position. At a slightly wider angle, from 9.3° to 28.7°, eight detector arms are arranged at 45° to each other at a distance of 2.5 m from the sample position. In addition, two high angle banks are positioned at angles of 110.4° to 119.4° (4 m) and 125.4° to 138.7° (2.5 m). These latter detectors enable the phonon density of states in polycrystalline materials to be estimated.

The 2.5 and 4 m detector banks have different resolutions due to their difference in distance from the sample. Since the energy of the scattered neutron is determined from its time-of-flight, the energy resolution is proportional to $\delta t/t$. Since the error associated with δt is the same for both detector banks, the 4 m bank has better resolution as the time, t, taken for a neutron to reach it is longer.

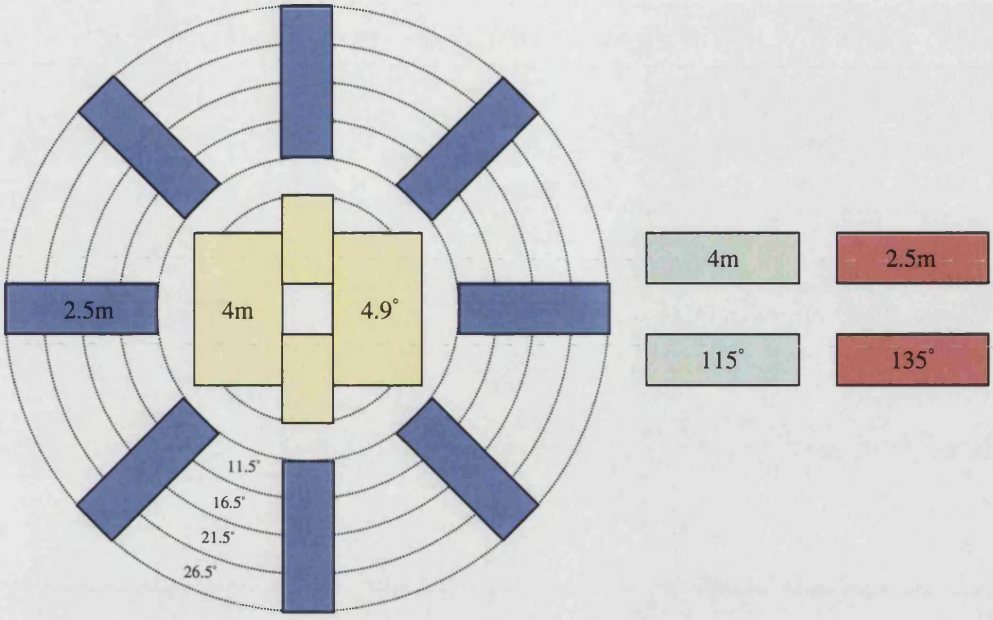

Figure 4.4 Schematic diagram of the HET detector banks. The blue and yellow detectors are the low angle banks at 2.5 and 4 m respectively, while the red and green detectors are the high angle banks at 2.5 and 4 m respectively. The average angle of each detector bank is shown.

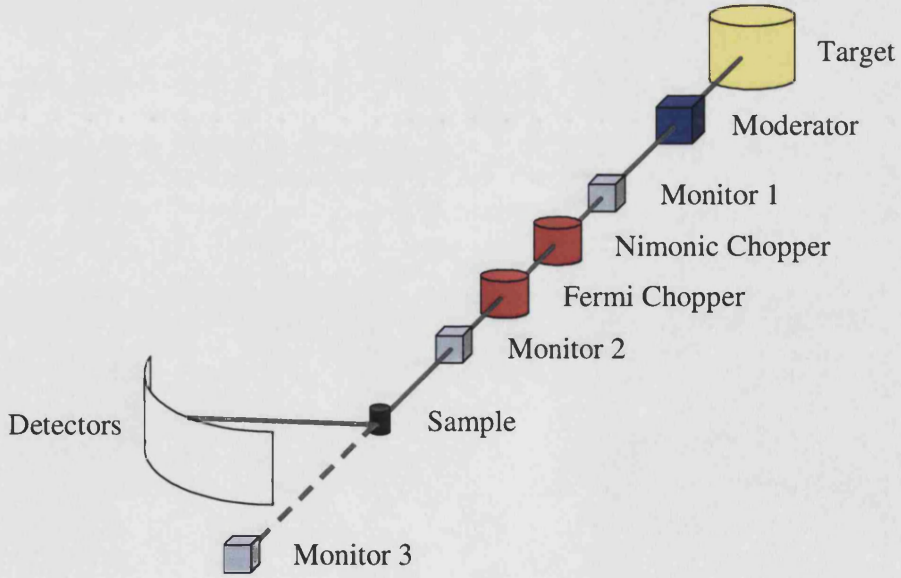

Figure 4.5 Schematic diagram of the HET layout. Neutrons from the target are moderated then pass through the choppers before being scattered from the sample into the detector banks.

In order to reduce the background noise, which arises from gamma rays generated from the spallation process and high-energy neutrons that thermalise within the spectrometer, a nimonic chopper is used to effectively close the beam tube at the moment the proton beam is incident on the target. The neutron beam is collimated to 45 x 45 mm at the sample position.

The beam is then monochromated by a Fermi chopper, which is a cylindrical drum consisting of thin sheets of highly absorbing boron interleaved with sheets of aluminium which are transparent to neutrons. The drum rotates in phase with the 50 Hz ISIS pulse such that only neutrons with the desired energy and wavelength are transmitted. To optimise transmission, the "slits" are curved in opposition to the direction of rotation. The "S" chopper used for all HET measurements produces a high flux at the expense of resolution (Figure 4.6).

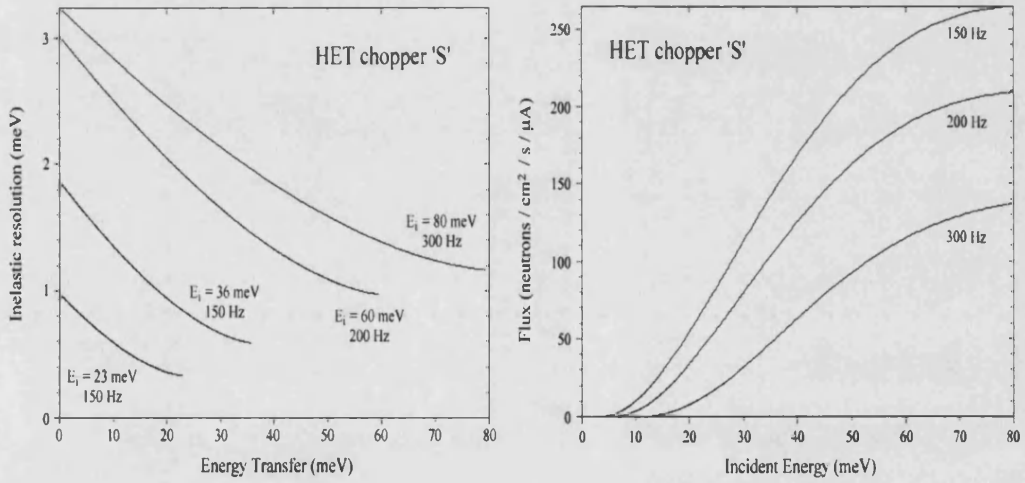

Figure 4.6 HET flux and resolution curves for different experimental arrangements.

Three monitors are installed on HET: one between the moderator and nimonic chopper, one between the Fermi chopper and sample and one in the straight through position after the sample. The time-of-flight between the latter two monitors is used to determine the incident neutron energy. In the same way, the energy of the detected neutrons is analysed by considering the time of flight over the known distance between sample and detectors. As the energy of the incident beam is known, the energy transfer at the sample can be calculated.

The beam tubes and detector banks are evacuated to a rough vacuum to reduce the background arising from air scattering. A Polycold is used to remove any moisture from the tank to ensure that ice does not build up during the experiment. The internal surfaces in the sample tank are lined with a low hydrogen B_4C resin mix which minimises the background arising from the scattering of high energy neutrons. Finally, apertures at the entrance to the sample tank can be adjusted to minimise the amount of beam falling on the sample environment apparatus.

For all the polycrystalline experiments, the arc-melted buttons were broken into small fragments to minimise the size of any crystallites in the sample and thereby reduce any preferential direction for Bragg scattering. These fragments were then placed into a thin Al foil sachet to give a sample area of 40 mm x 40 mm.

In order to convert the raw time-of-flight data (i.e. counts per second) into the scattering function $S(\mathbf{Q},\omega)$ in absolute units, measurements of the HET calibration sample are made during the experiment. This is a flat slab of vanadium measuring 2.1 x 40 x 40 mm and weighing 20.14 g. The data obtained from the scattering of a "white beam" of neutrons from the vanadium sample is used to eliminate inaccurate detectors and those containing Bragg peaks. The raw time-of-flight data is then converted into absolute units by normalising to this vanadium data and to the incident flux. *Therefore, for all of the HET data presented in this thesis, the intensities are measured in units of mb/sr/meV/U.*

4.3.2.1 Separation of magnetic and phonon scattering

In order to obtain the magnetic scattering from a sample, it is necessary to subtract the scattering due to phonon modes of the crystal lattice from the total scattering observed. The method by which the phonon contribution has been estimated is known as the *ratio method.*

The ratio method was first described by Murani[3] and makes use of the fact that any magnetic scattering is negligible at high momentum transfers, as a result of the wavevector dependence of magnetic form factors. This means that the low angle detector banks contain both magnetic and phonon contributions whereas the scattering in the high angle detector banks is almost entirely phonon based.

In order to estimate the phonon contribution at low scattering angles, a non-magnetic reference compound which has an identical crystal structure (and ideally an identical sample mass) is required. For uranium-based compounds an isostructural thorium compound is usually used. It is assumed that the phonon scattering is the same from both the sample and the reference material, so that an energy transfer dependent scaling function can be defined. The phonon scattering at low angles in the magnetic compound can then be obtained via:

$$U_{low}^{phonon} = U_{high} \times \frac{Th_{low}}{Th_{high}}$$

The ratio of the low angle to high angle data from the non-magnetic compound is usually found to lie between $\frac{1}{4}$ and $\frac{1}{5}$, so when a suitable reference material is not available a constant ratio of $\frac{1}{4.5}$ can be used to estimate the phonon contribution. The magnetic scattering of interest can finally be obtained by subtraction of this phonon contribution from the total scattering in the low angle detector bank:

$$U_{low}^{magnetic} = U_{low}^{total} - U_{low}^{phonon}$$

The ratio method was found to be the most reliable way to estimate phonon spectra in a comparison of different methods made[4].

4.4 Data analysis

For all of the fits presented in this thesis, a least squares method was used to minimise χ^2, which is defined by:

$$\chi^2 = \sum_{i=1}^{N} \frac{(I_i - I_i')^2}{(N-p)\sigma_i^2}$$

where I and I' are the measured and calculated values, σ is the standard error and $(N - p)$ is the number of degrees of freedom given by the number of data points, N, minus the number of free parameters, p.

For experimental measurements involving neutron spectrometers, the measured peaks are a convolution of the instrumental resolution and the intrinsic peak shape associated with processes occurring in the sample. The resolution of triple axis spectrometers can usually be approximated by a Gaussian peak shape in Q and ω space. Since the measured peak widths in the PrNiSn analysis were often only slightly larger than the instrumental resolution, a Gaussian model for the peak shape was used for simplicity. Future studies at a higher resolution might use a more accurate model for the peak shape, e.g. Lorentzian or Damped Harmonic Oscillator, in order to determine the lifetime of the excitation.

4.5 References

[1] V2, Hahn-Meitner Institute (http://www.hmi.de/bensc/instrumentation/instrumente/v2/v2.html)

[2] ISIS, Rutherford Appleton Laboratory (http://www.isis.rl.ac.uk/excitations/het/)

[3] A. P. Murani, Phys. Rev. B, **28** (1983) 2308

[4] E. A. Goremychkin and R. Osborn, Phys. Rev. B **47** (1993) 14280

CHAPTER 5

PrNiSn

5.1 Literature Review

PrNiSn is a member of the RTX series of compounds which have been studied comprehensively. In comparison to CeNiSn, however, relatively little work has been done on PrNiSn. The crystal structure of PrNiSn, as deduced by x-ray diffraction[1], is the orthorhombic TiNiSi-type (space group *Pnma*) with lattice parameters of a = 7.440 Å, b = 4.560 Å and c = 7.706 Å. The Pr ions have a $4f^2$ configuration and are situated on the 4*c* crystallographic sites. Neutron diffraction[2] by Beirne *et al.* confirmed the room temperature structure and the absence of long-range magnetic ordering down to 1.7 K.

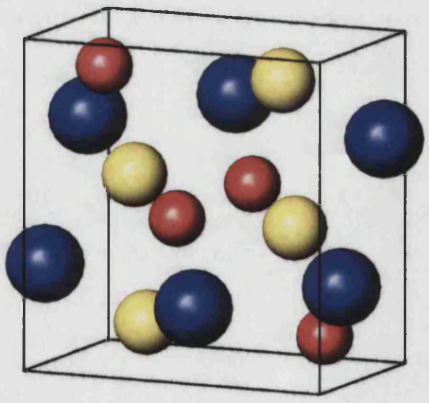

Figure 5.1 The orthorhombic unit cell of PrNiSn showing the Pr (blue), Ni (yellow) and Sn (red) atoms.

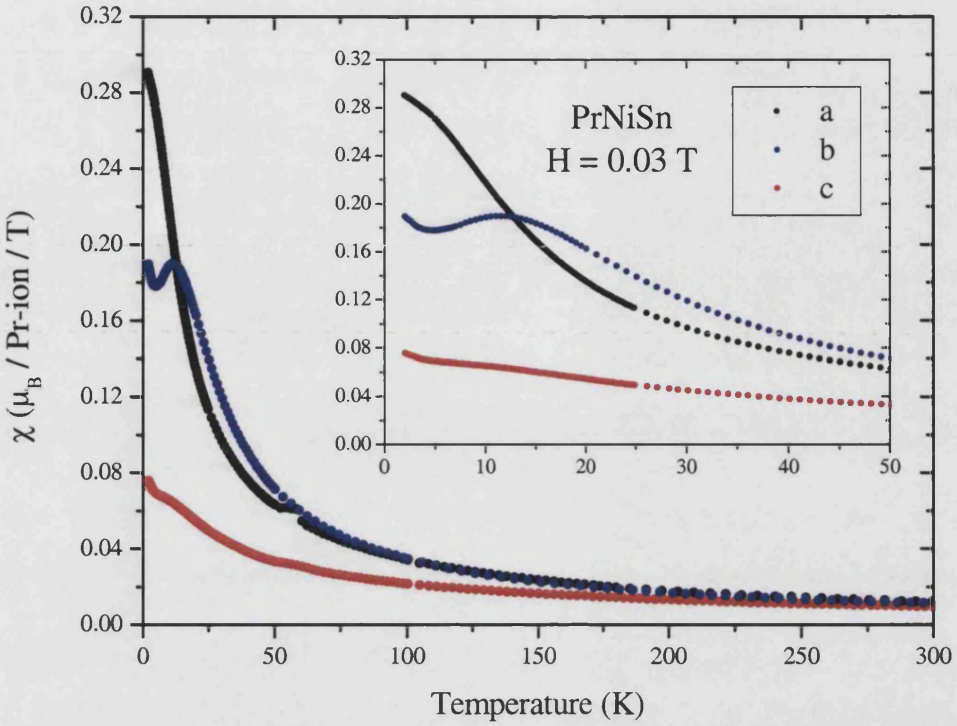

Figure 5.2 Magnetic susceptibility of PrNiSn showing Curie-Weiss behaviour down to 40 K. Inset: the low temperature data showing a local maximum and minimum along the *b*-axis.

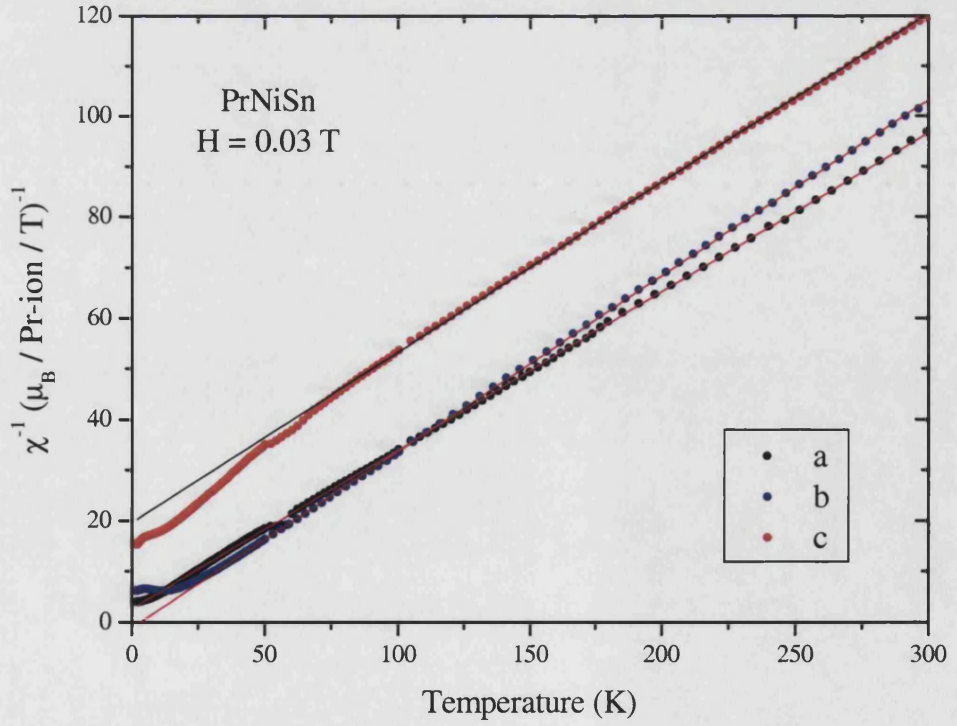

Figure 5.3 Inverse susceptibility of PrNiSn showing fits to the Curie-Weiss law using data points between 60 and 300 K.

Bulk measurements[2] were also carried out by Beirne *et al.* on a polycrystalline sample of PrNiSn. The susceptibility was found to obey the Curie-Weiss law down to 40 K, giving a Curie-Weiss temperature of θ_{CW} = -18 K and an effective moment of $\mu_{eff} = 3.58\mu_B$ (in agreement with Routsi *et al.*[3]). No magnetic transitions were observed down to a temperature of 2 K and resistivity measurements did not show any transitions down to 2 K.

Susceptibility and magnetisation measurements were also carried out on a single crystal of PrNiSn. No magnetic transitions were observed in the susceptibility data for any of the axes, but a clear maxima and minima were observed along the *b*-axis at low temperature (Inset to Figure 5.2). The values of the Curie-Weiss temperature and effective magnetic moment are shown in Table 5.1. Magnetisation measurements along the three principal axes did not reveal any transitions in fields up to 7 T, and the magnetic moments had not reached their saturation values by this field strength.

	θ_{CW} (K)	μ_{eff} (μ_B/Pr-ion)
a-axis	-7 ± 0.4	3.74 ± 0.06
b-axis	4 ± 0.4	3.56 ± 0.04
c-axis	-52 ± 1.1	3.58 ± 0.04
polycrystalline	-18 ± 0.5	3.58 ± 0.05

Table 5.1 Curie-Weiss temperatures and effective magnetic moments for single crystal and polycrystalline PrNiSn obtained by fitting to the magnetic susceptibility.

Inelastic neutron scattering on a polycrystalline sample[2] was able to show seven of the eight excitations expected from the ground state, at energy transfers of 1.8, 3.3, 5.3, 7.3, 17.2, 23.3 and 28.4 meV. Least squares fitting to this data was used to determine a set of Stevens parameters, which are listed in Table 5.2. These parameters were then used to calculate an energy level scheme which is shown in Figure 5.5.

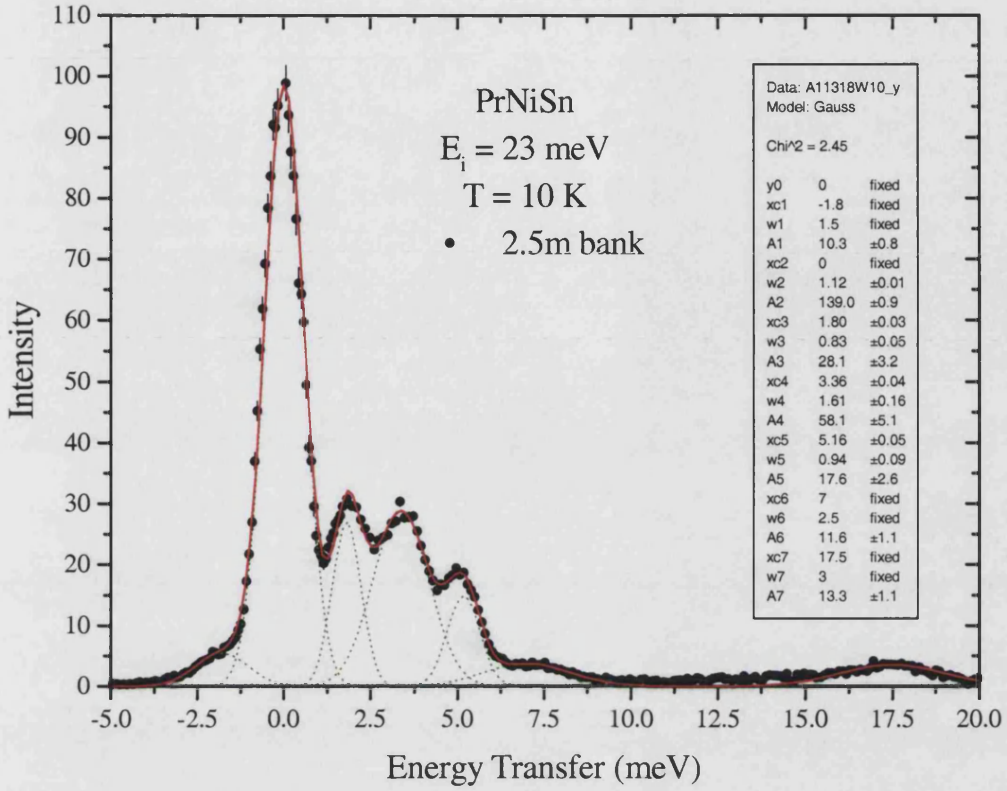

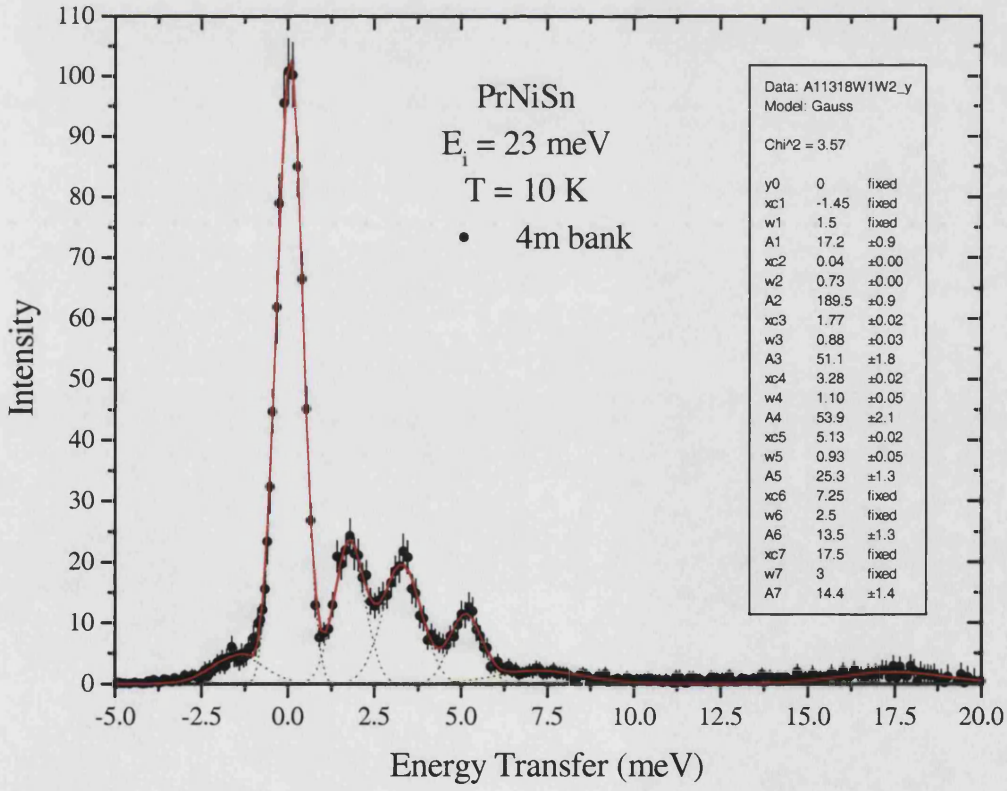

Figure 5.4 Magnetic scattering from PrNiSn in the 2.5 m and 4 m detector banks. The dotted lines are fitted gaussian peaks and the red line is the total fit (E. D. Beirne, PhD Thesis, 2002).

Parameter	meV
B_2^0	-0.225 ± 0.003
B_2^2	0.384 ± 0.004
B_4^0	(0.981 ± 0.001) x 10^{-02}
B_4^2	(-0.170 ± 0.010) x 10^{-01}
B_4^4	(-0.494 ± 0.001) x 10^{-01}
B_6^0	(-0.165 ± 0.055) x 10^{-03}
B_6^2	(-0.100 ± 0.021) x 10^{-02}
B_6^4	(-0.265 ± 0.004) x 10^{-02}
B_6^6	(-0.502 ± 0.284) x 10^{-03}

Table 5.2 Stevens parameters for PrNiSn, obtained from least squares fitting of inelastic neutron data..

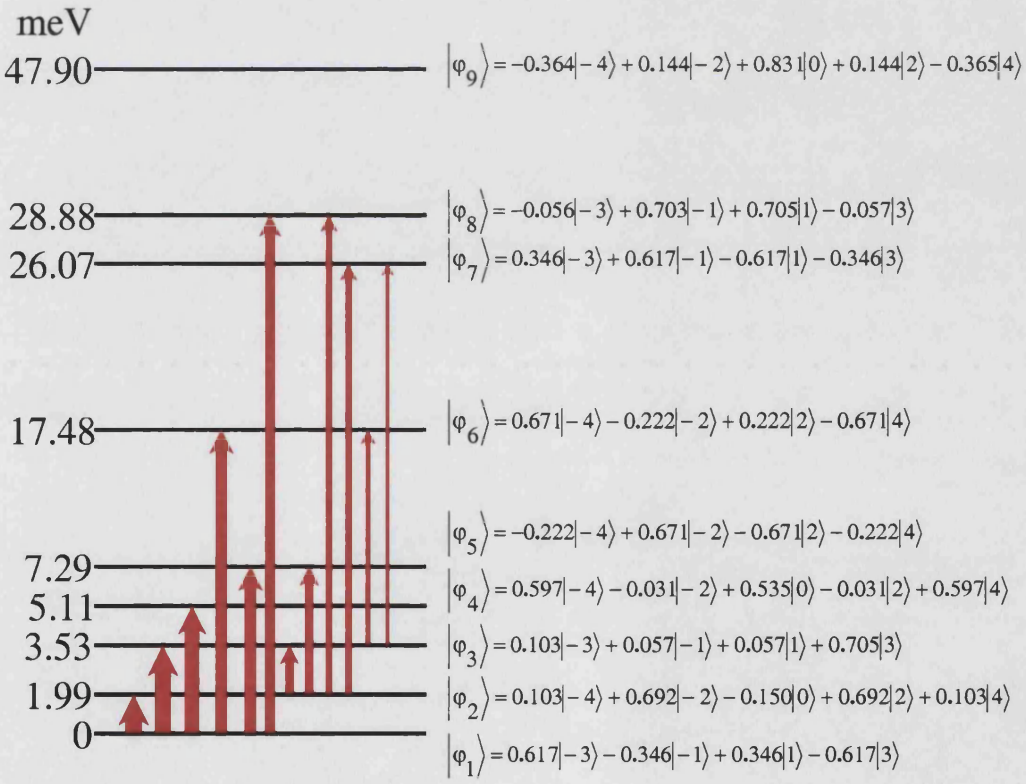

Figure 5.5 Crystal field scheme for PrNiSn deduced from the Stevens parameters obtained above. The thickness of the lines indicates the probability of the transition between levels.

In order to investigate the excitations below 10 meV, Beirne *et al.* performed inelastic neutron scattering on a single crystal of PrNiSn using the V2 diffractometer at the HMI in Berlin.

They found that two excitations exist around 3.5 meV and that both of these modes exhibit dispersion along the [0 0 **Q**] and [**Q** 0 0] directions (see Figures 5.6 and 5.7). The upper modes can be described by a nearest-neighbour interaction, but the lower modes require an additional next-nearest-neighbour interaction to be included. Since the peaks at (1 0 0) and (0 0 1) are of similar intensity, the 3.5 meV modes were determined to be polarised along the b^* direction.

An excitation at 2.4 meV was also observed, but they could not detect any dispersion of this mode along [0 0 **Q**]. Furthermore, this peak is much weaker at (1 0 0) than at (0 0 1), which indicates that the 2.4 meV mode is polarised along the a^* direction.

In this experiment, a broad region of scattering was observed at low energy around 0.5 meV. The temperature dependence of the position and area of this scattering indicated some kind of transition at around 4.5 K below which both of these values increased. Another peak at around 1.5 meV was seen at the (0 0 3) position and was determined to be unrelated to the lower energy scattering.

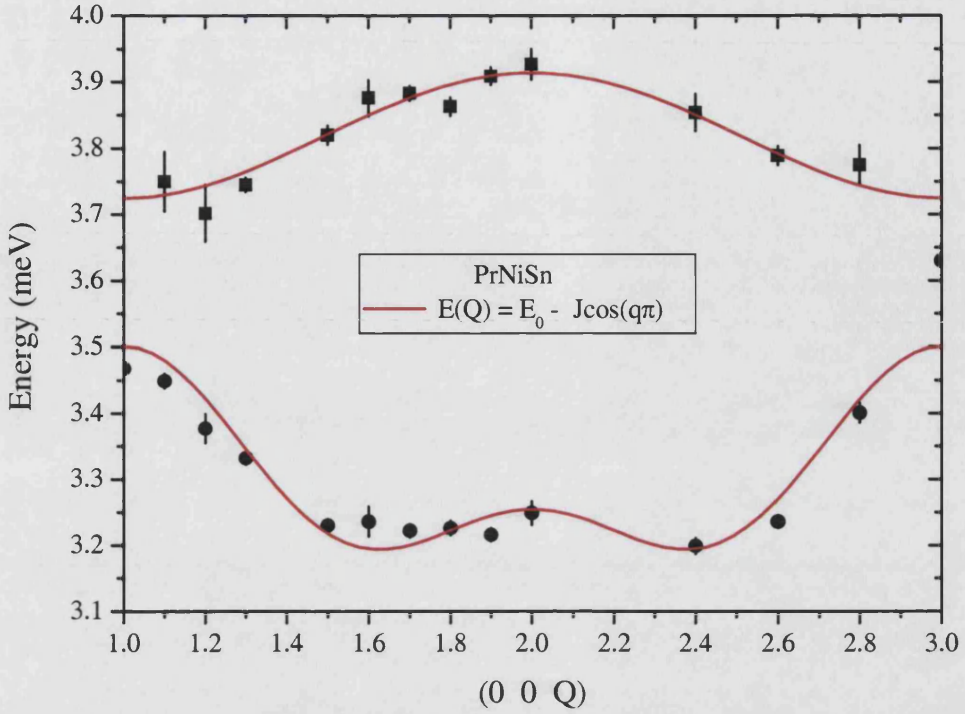

Figure 5.6 Dispersion of the 3.5 meV modes along the [0 0 **Q**] direction. The lines are fits to the singlet-singlet dispersion relation as discussed in the text (E. D. Beirne, PhD Thesis, 2002).

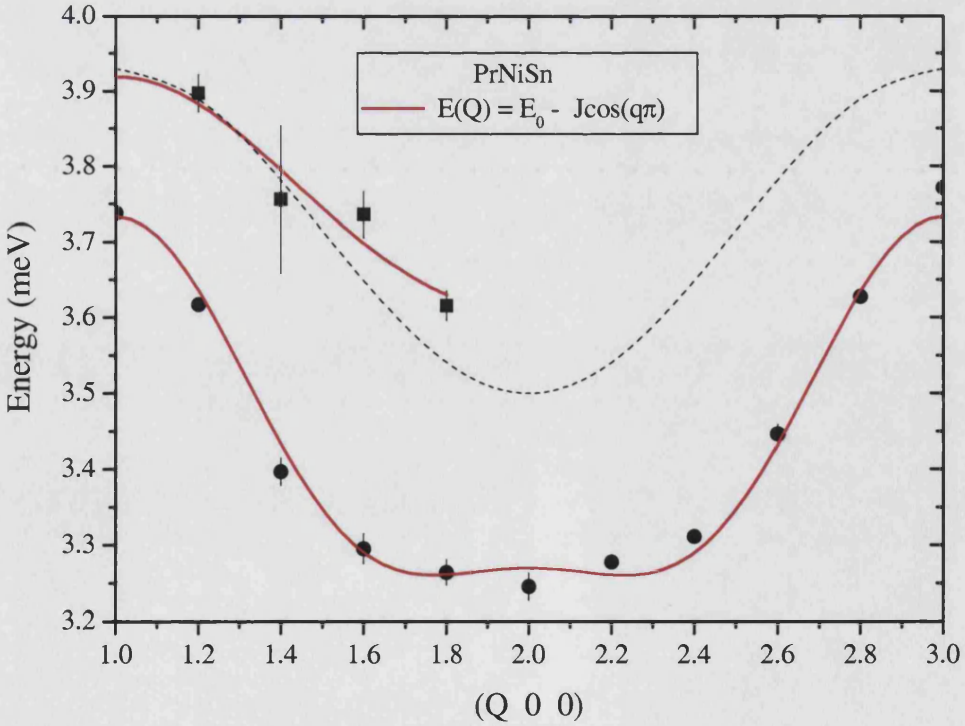

Figure 5.7 Dispersion of the 3.5 meV modes along the [**Q** 0 0] direction. The lines are fits to the singlet-singlet dispersion relation as discussed in the text (E. D. Beirne, PhD Thesis, 2002).

5.2 Experimental Procedure

The neutron diffraction measurements presented here were obtained using the V2 diffractometer at the HMI facility in Berlin. Firstly, a scan through the elastic peak of a standard Vanadium sample was performed to determine the energy resolution, which was found to be 0.195 ± 0.005 meV. The same single crystal of PrNiSn used in the previous V2 experiment was then mounted on an aluminium sample holder with the a^*-c^* plane horizontal (as shown in Figure 5.8). Cadmium was wrapped around the base to prevent scattering from the adhesive. It was then attached to a sample stick, inserted into a standard Orange (ILL-type) cryostat and cooled to a base temperature of 1.6 K.

The collimation was set to 40'-60'-60', a Be filter was placed between the sample and analyser crystal and the final wavevector, k_f, was fixed at 1.55 $Å^{-1}$. This configuration allowed a maximum energy transfer of around 6 meV. Alignment on the (2 0 0) and (0 0 2) Bragg peaks resulted in lattice parameters of a = 7.47 Å and c = 7.69 Å. The diaphragms immediately before and after the sample were then adjusted to optimise the signal by reducing background scattering from the cryostat.

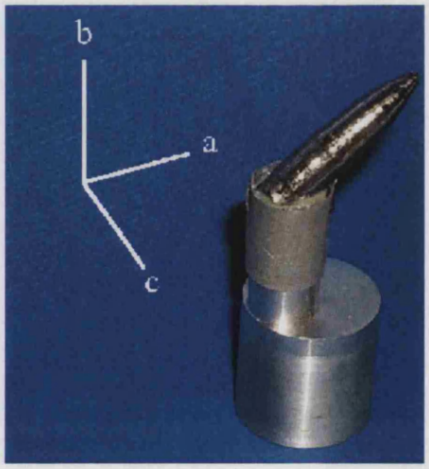

Figure 5.8 The single crystal of PrNiSn mounted with the a^*-c^* plane horizontal. Note the cadmium shielding around the base of the crystal.

Initially, broad scans covering an energy range from –0.6 to 3.95 meV were made at the (0 0 1) position. This was to look for the unusual scattering around 0.5 meV seen in the previous experiment, as well as to ensure that the 2.5 meV and 3.5 meV peaks were also present. These scans were then repeated at a temperature of 6 K.

As can be seen in Figure 5.9, no sign of the scattering around 0.5 meV was observed at either temperature. This suggests that the scattering seen previously was due to helium trapped in the cryostat, and this would also explain the apparent transition at around 4.2 K which had been observed.

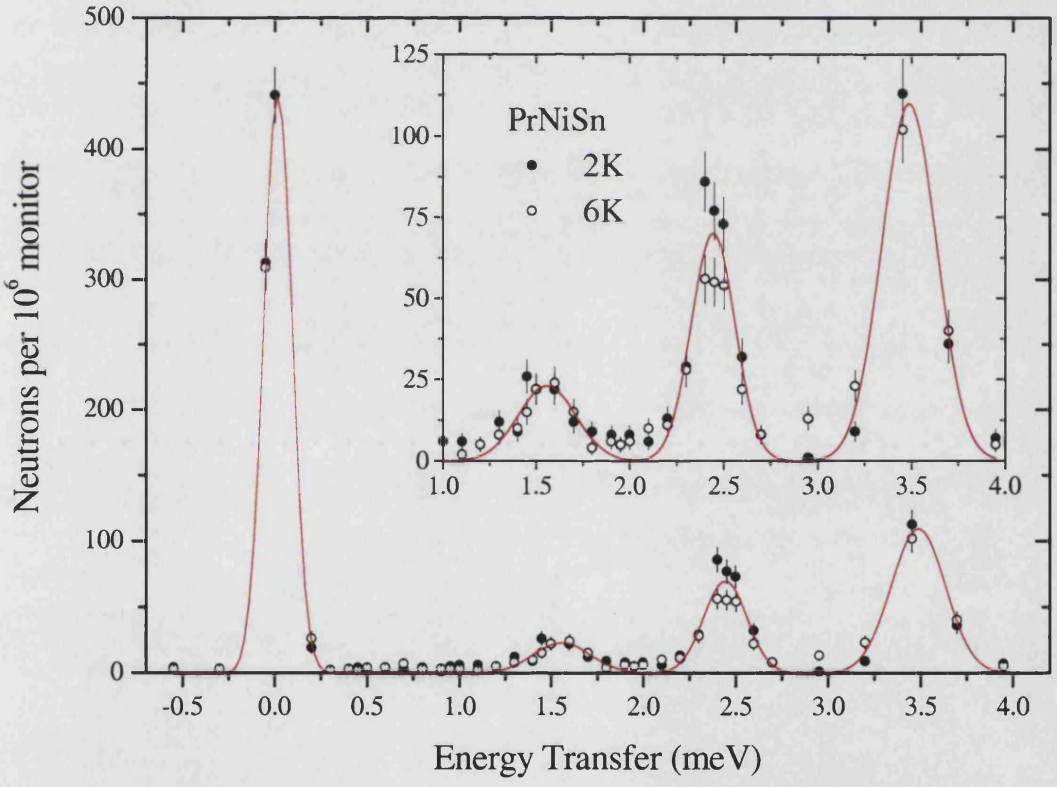

Figure 5.9 Broad energy scan at (0 0 1) showing the elastic peak and three excitations at around 1.5, 2.5 and 3.5 meV. Note the absence of the spurious scattering at low energy which was observed in the previous experiment.

However, in eliminating this spurious scattering, a further peak at 1.5 meV was revealed in addition to the peaks at 2.5 and 3.5 meV seen in the previous experiment. This peak had been observed in the previous experiment but was obscured by the spurious scattering.

In order to determine whether this 1.5 meV mode exhibited any dispersion, a series of scans were made in the [0 0 **Q**] direction between **Q** = 0.8 and 3. At the position of the most intense peak, i.e. at (0 0 2.6), a measurement was also made after heating the sample to 20 K. A few scans were then performed to look at the dispersion in the [**Q** 0 0] direction, although there was insufficient time to make a detailed study in this direction.

Next, a detailed study of the 2.5 meV peak was made to look at the dispersion of this mode along the [0 0 **Q**] direction. A similar study was made on a peak observed at 5.2 meV to obtain the dispersion of this mode along the [**Q** 0 0] direction. Measurements of this peak were also made at a few points in the [0 0 **Q**] direction. Finally, three scans were made on the 3.5 meV peak to help with fitting the theoretical model to the data obtained in the previous experiment.

The PrNiSn sample was then removed from the cryostat and the NdNiSn crystal inserted with the a^*-c^* plane horizontal. After aligning the crystal on the (2 0 0) and (0 0 2) Bragg peaks at base temperature, the temperature was raised to 6 K and preliminary measurements were made to look for excitations. No peaks were observed below 2.5 meV at either (1 0 0) or (0 0 1), but peaks were observed around 5.4 meV at the (2 0 0), (0 0 2), (3 0 0) and (0 0 3) positions.

5.3 Results & Discussion

For all of the results shown, the number of counts have been normalised to a monitor value of 10^6 counts and the errors are simply the square root of the number of counts. Typically, it would take between 300 and 600 seconds to obtain a data point.

The dispersion relation for a singlet-singlet (Ising) model, as derived by Jensen and Mackintosh[4], is given by:

$$E(\mathbf{Q}) = \sqrt{\Delta\left(\Delta - 2n_{01}M_{\alpha}^{2}J_{\alpha\alpha}(\mathbf{Q})\right)}$$

where Δ is the energy difference, n_{01} is the population difference and $M_{\alpha} = \left|\langle 1|J_{\alpha}|0\rangle\right|$ is the matrix element of J_{α} between the two states. In the limit of $\Delta >> 2n_{01}M_{\alpha}^{2}J_{\alpha\alpha}(\mathbf{Q})$, the dispersion can be approximated by:

$$E(\mathbf{Q}) = \Delta - \eta_{01}M_{\alpha}^{2}J_{\alpha\alpha}(\mathbf{Q})$$

where $J_{\alpha\alpha}(\mathbf{Q})$ is the Fourier transform of the exchange interaction, J_{α}. To fit our data, we have used the following expression:

$$E(\mathbf{Q}) = \Delta + J_1[\cos(\mathbf{Q}\pi)] + J_2[\cos(2\mathbf{Q}\pi)]$$

in which the J_1, J_2 parameters include the matrix elements and population factors. The J_1 term gives the effect of nearest-neighbour interactions, whereas the J_2 term accounts for the next-nearest-neighbour interactions.

5.3.1 1.5 meV mode

H	K	L	Centre (meV)	Step (meV)	No. of Points	Monitor (counts)	Temperature (K)
0	0	0.8	1.5	0.1	11	10^6	1.8
0	0	1	1	0.2	11	10^6	2.4
0	0	1	1.5	0.1	11	10^6	1.6
0	0	1.2	1.5	0.1	11	10^6	1.6
0	0	1.4	1.5	0.1	11	10^6	1.6
0	0	1.6	1.5	0.1	11	10^6	1.6
0	0	1.8	1.6	0.1	13	10^6	1.6
0	0	2	1.7	0.1	13	10^6	1.6
0	0	2.2	1.6	0.1	13	10^6	1.6
0	0	2.4	1.5	0.1	11	10^6	1.6
0	0	2.6	1.5	0.1	11	10^6	1.6
0	0	2.6	1.6	0.1	11	10^6	20
0	0	2.8	1.5	0.1	11	10^6	1.6
0	0	3	1.5	0.1	11	10^6	1.6
0	0	3	1	0.2	11	10^6	1.6
1	0	0	1.6	0.1	11	10^6	1.8
2	0	0	1.6	0.1	11	10^6	1.8
3	0	0	1.6	0.1	11	10^6	1.8

Table 5.3 Summary of the scans made on the 1.5 meV mode.

5.3.1.1 [0 0 Q] direction

In order to check for dispersion of the 1.5 meV mode along the [0 0 **Q**] direction, a series of scans were made at intervals of $\Delta\mathbf{Q} = 0.2$ between (0 0 0.8) and (0 0 3). The (0 0 2.6) peak is shown in Figure 5.10 and demonstrates the fitting technique using a single gaussian function. The effect of temperature on the (0 0 2.6) peak is shown in Figure 5.10. This peak was chosen as it was the position of greatest intensity in the (0 0 **Q**) series.

Increasing the temperature from 1.6 to 20 K increases the background count rate which is expected since the amount of multiple scattering will increase as the phonon population increases. The peak width and position do not change significantly but the intensity decreases considerably as the ground state is depopulated.

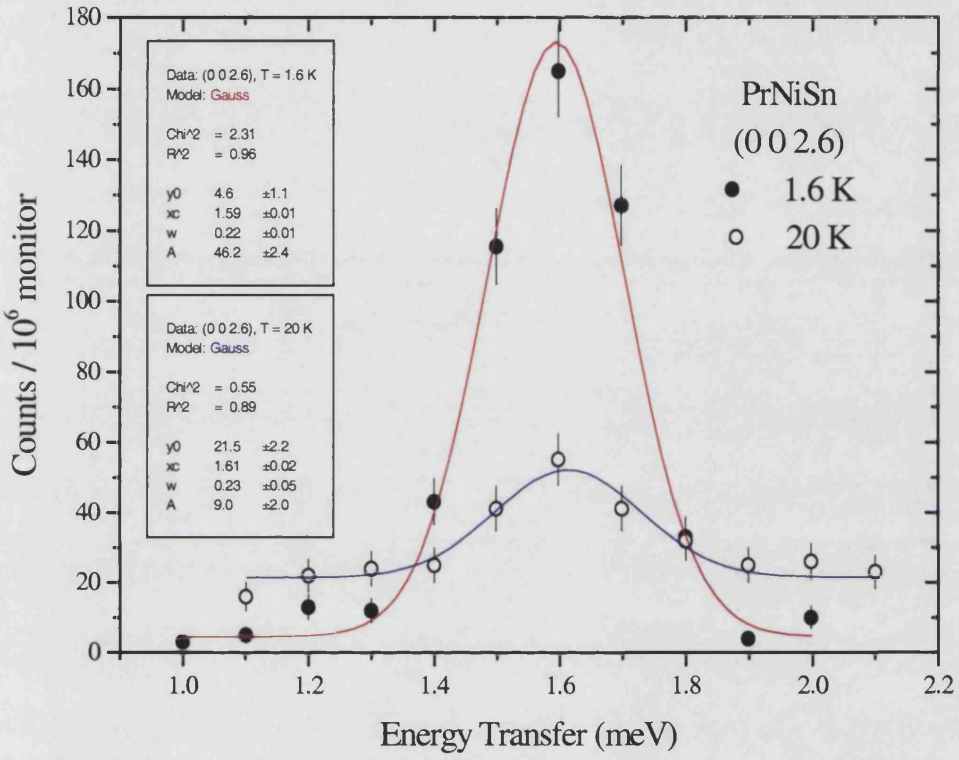

Figure 5.10 Single gaussian fits to the 1.5 meV peak at (0 0 2.6) measured at T = 1.6 and 20 K.

The complete series of scans is shown in Figure 5.11 where the dotted line is a guide to the eye to show the dispersion along [0 0 **Q**]. Plotting the central position of the fitted peaks against wavevector, **Q**, results in the data shown in Figure 5.12. The curve shown is a fit to the singlet-singlet dispersion (as discussed in Section 5.3) and the parameters obtained are shown below.

$$E(\mathbf{Q}) = \Delta + J_1 \cos(\mathbf{Q}\pi) + J_2 \cos(2\mathbf{Q}\pi)$$

Δ	J_1	J_2
1.65 ± 0.01	0.13 ± 0.01	$0 \pm$ fixed

Table 5.4 Dispersion parameters for the 1.5 meV mode. (All units are in meV.)

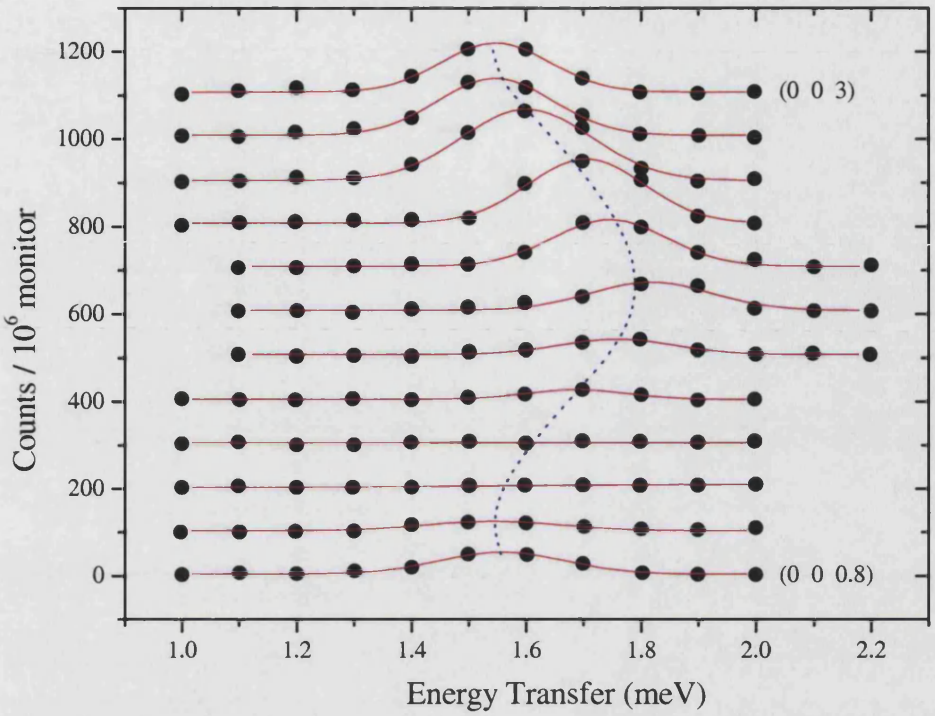

Figure 5.11 Dispersion of the 1.5 meV mode from (0 0 0.8) at the bottom to (0 0 3) at the top. Note that each scan has been offset by 100 counts and the dotted line is a guide to the eye.

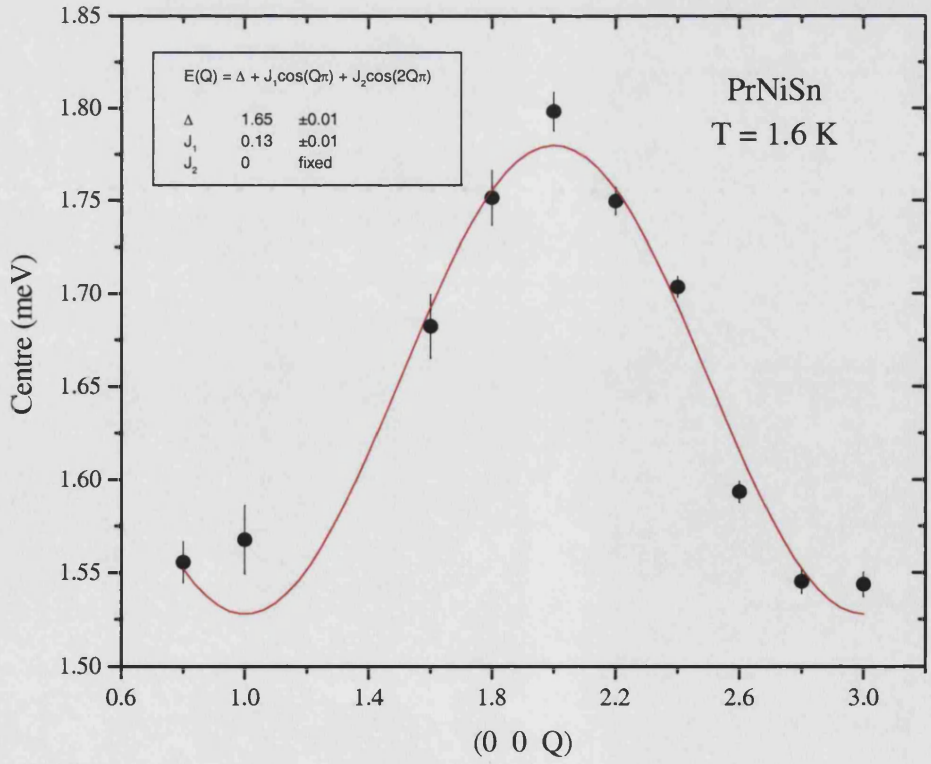

Figure 5.12 Dispersion of the 1.5 meV mode along [0 0 **Q**] and fit to the singlet-singlet model. Note that the data points at **Q** = 1.2 and 1.4 were not included in the fit.

5.3.1.2 [Q 0 0] direction

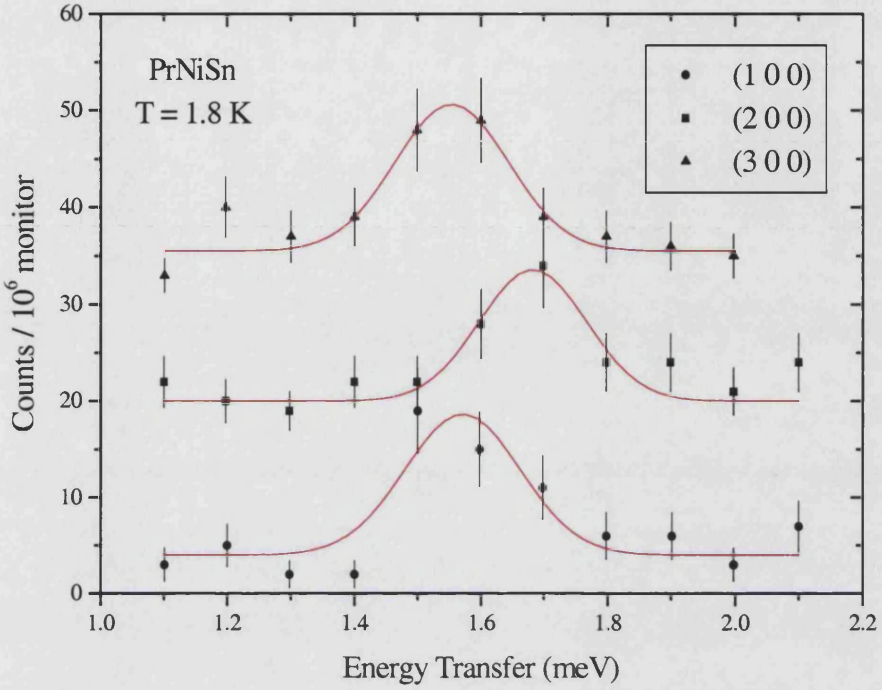

Figure 5.13 The dispersion of the 1.5 meV mode in the [**Q** 0 0] direction. Each curve has been offset by 15 counts for clarity.

The (1 0 0), (2 0 0) and (3 0 0) peaks are shown in Figure 5.13. Although a dispersion relation cannot be obtained, it is clear that the 1.5 meV excitation does indeed move as the wavevector **q** relative to the zone centre is changed. There is little variation in the peak intensities at these positions.

If we compare these peaks with the corresponding (0 0 1), (0 0 2) and (0 0 3) peaks, however, we see that there is much more dispersion and greater intensity in the [0 0 **Q**] direction (Figure 5.14). These results suggest that the 1.5 meV mode is strongly polarised along the *c*-direction.

Since nuclear Bragg peaks are found at (2 0 0) and (0 0 2) but are absent at (1 0 0) and (0 0 1), we can conclude that the zone centres are at **Q** = 2 and the zone boundaries are at **Q** = 1 and 3. Note that the modes are highest in energy at the zone centres.

5.3.1.3 Comparison of [0 0 Q] and [Q 0 0]

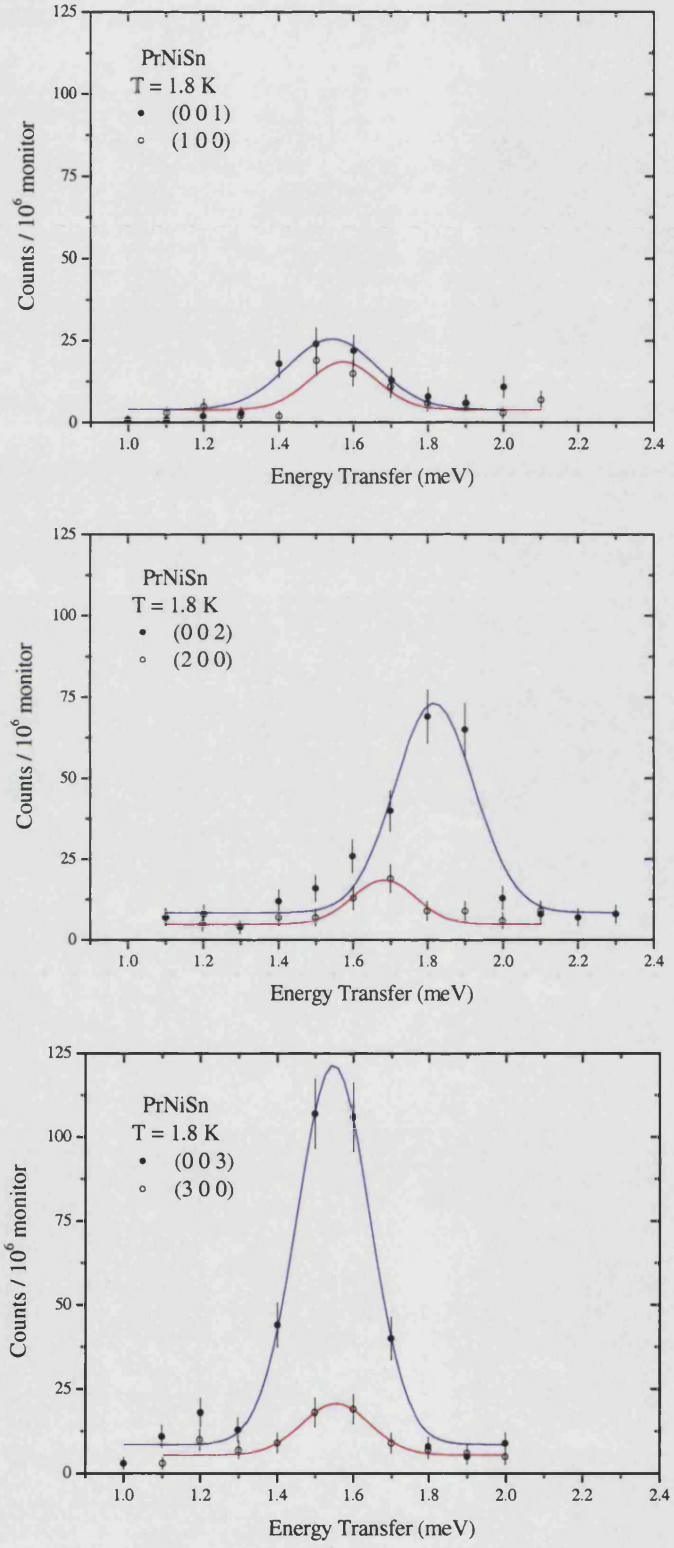

Figure 5.14 Comparison of the 1.5 meV modes at different (0 0 **Q**) and (**Q** 0 0) positions.

5.3.2 2.5 meV mode

H	K	L	Centre (meV)	Step (meV)	No. of points	Monitor (counts)	Temperature (K)
0	0	1	1.7	0.25	19	10^6	2
0	0	1	1.5	0.1	25	10^6	2
0	0	1.2	2.6	0.1	11	10^6	1.8
0	0	1.4	2.6	0.1	11	10^6	1.8
0	0	1.6	2.6	0.1	11	10^6	1.8
0	0	1.8	2.6	0.1	11	10^6	1.8
0	0	1.8	2.55	0.05	15	10^6	1.7
0	0	2	2.6	0.1	11	10^6	1.8
0	0	2	2.55	0.1	7	10^6	1.7
0	0	2.2	2.5	0.05	15	2×10^6	1.7
0	0	2.4	2.5	0.05	15	2×10^6	1.6
0	0	2.6	2.5	0.05	15	2×10^6	1.6
0	0	2.8	2.45	0.05	15	2×10^6	1.6
0	0	3	2.6	0.1	11	10^6	1.8
0	0	3.2	2.45	0.05	15	10^6	1.6
0	0	3.2	2.45	0.05	9	10^6	1.6

Table 5.5 Summary of the scans made on the 2.5 meV mode.

5.3.2.1 [0 0 Q] direction

The dispersion of the 2.5 meV mode along the [0 0 **Q**] direction was investigated by a series of scans made at intervals of $\Delta\mathbf{Q} = 0.2$ between (0 0 1) and (0 0 3.2). The (0 0 1.4) peak is shown in Figure 5.15 and demonstrates the fitting technique using a single gaussian function. The complete series of scans is shown in Figure 5.16 where the dotted line is a guide to the eye to show the dispersion along [0 0 **Q**].

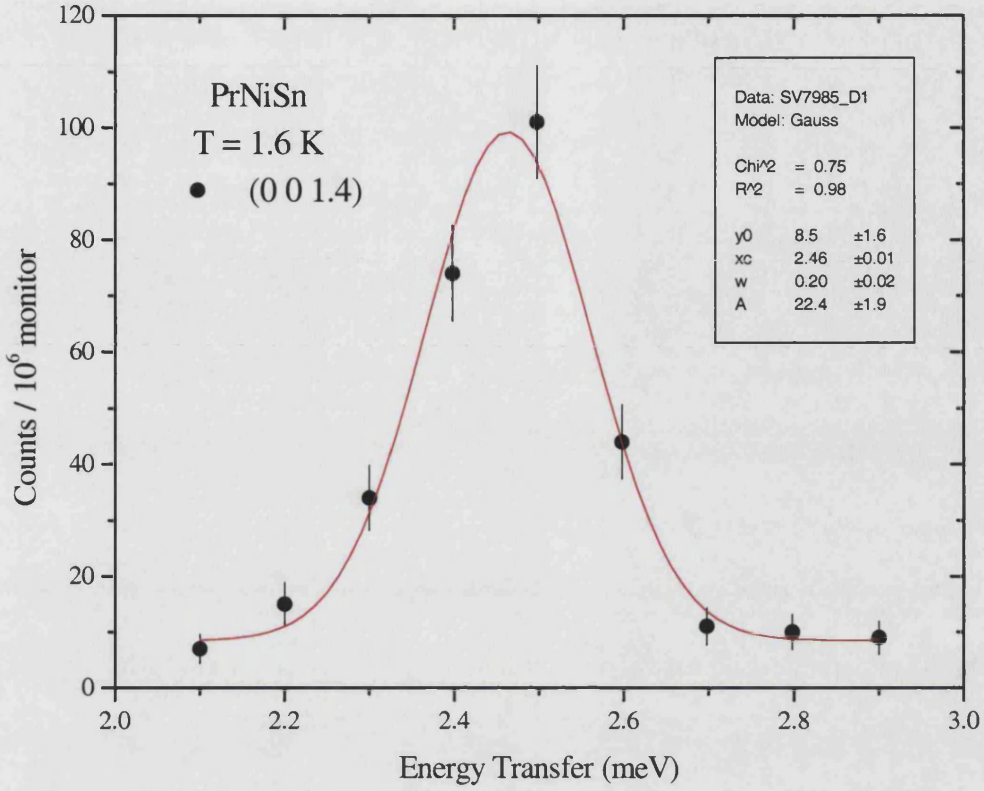

Figure 5.15 An example of the single gaussian fitting technique for the data at (0 0 1.4).

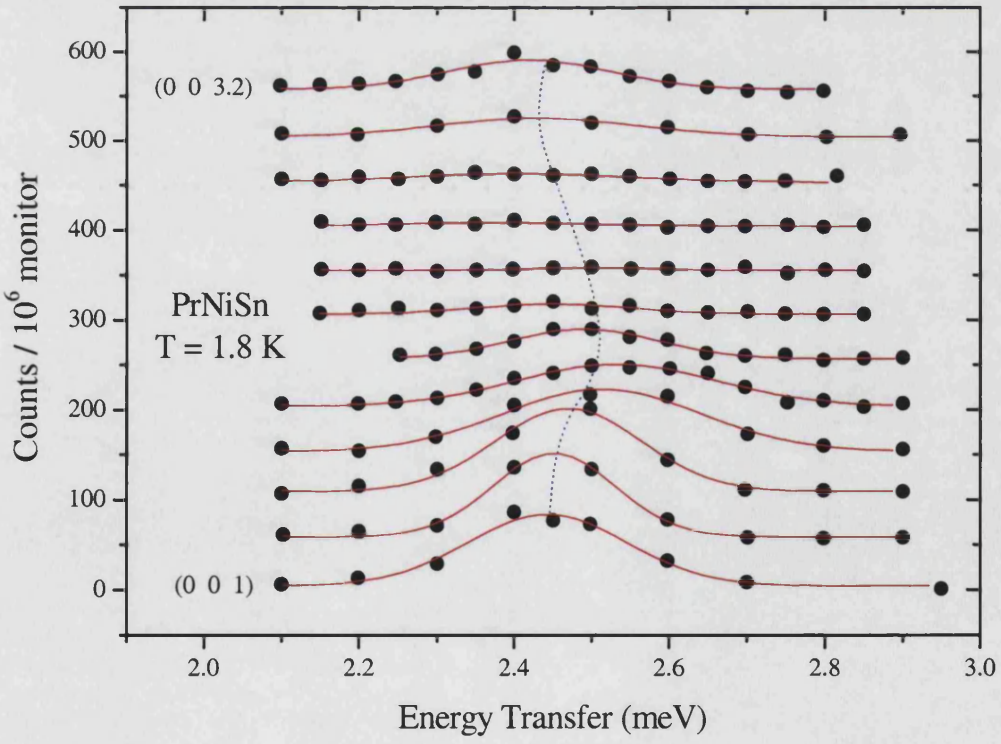

Figure 5.16 Dispersion of the 2.5 meV mode from (0 0 1) at the bottom to (0 0 3.2) at the top. Note that each scan has been offset by 50 counts and that the dotted line is a guide to the eye.

Plotting the central position of the fitted peaks against wavevector, **Q**, results in the data shown in Figure 5.17. The red curve shows a fit to the singlet-singlet dispersion (as discussed in Section 5.3) but it does not model the data very well. The maxima and minima of the dispersion appear to be shifted away from the integer lattice positions, so a further fit was made using the same dispersion relation but with an extra parameter – a phase factor, δ. This fit is shown by the dotted blue line in Figure 5.17.

However, after returning to the raw data it was noted that the data sets for (0 0 2.2) and (0 0 2.8) had very poor statistics. Therefore the gaussian fits of these data sets were repeated but with their positions fixed by eye. The resulting data is shown in Figure 5.18 along with a fit to the singlet-singlet dispersion relation. This method appears to validate a dispersion model which is commensurate with the reciprocal lattice and which does not require an additional phase factor. The parameters obtained from this fit (which does not take into account the fixed data points) are given below.

$$E(\mathbf{Q}) = \Delta + J_1 \cos(\mathbf{Q}\pi) + J_2 \cos(2\mathbf{Q}\pi)$$

Δ	J_1	J_2
2.48 ± 0.01	0.04 ± 0.01	0 ± fixed

Table 5.6 Dispersion parameters for the 2.5 meV mode. (All units are in meV.)

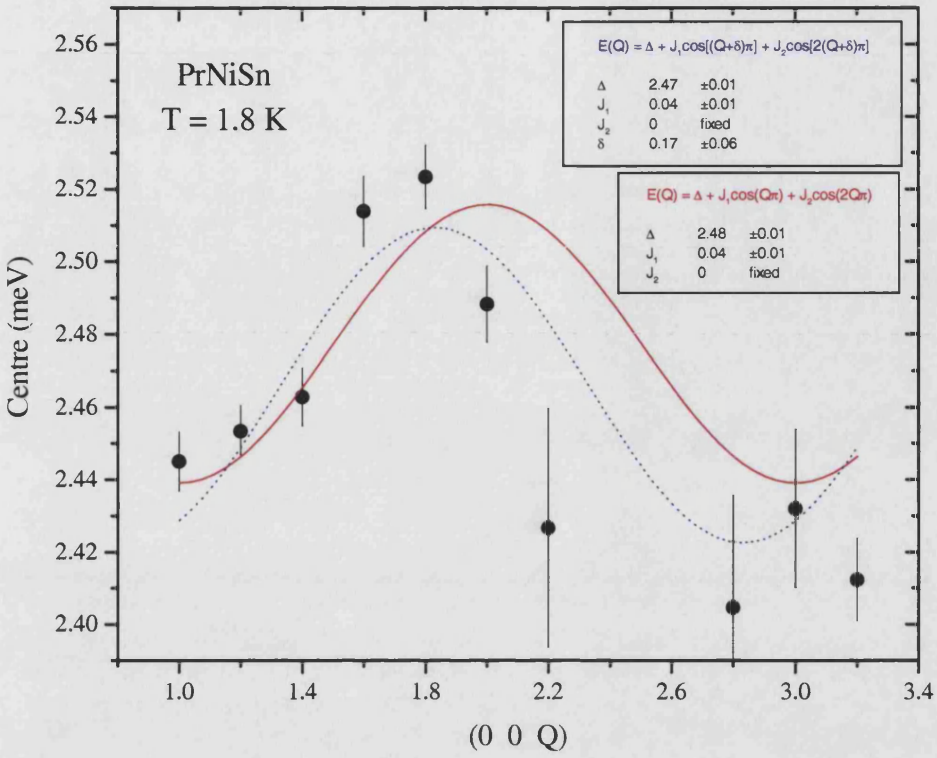

Figure 5.17 Dispersion of the 2.5 meV mode along [0 0 **Q**]. The red line is a fit to the singlet-singlet model. The blue line is the same fit but includes a phase factor, δ.

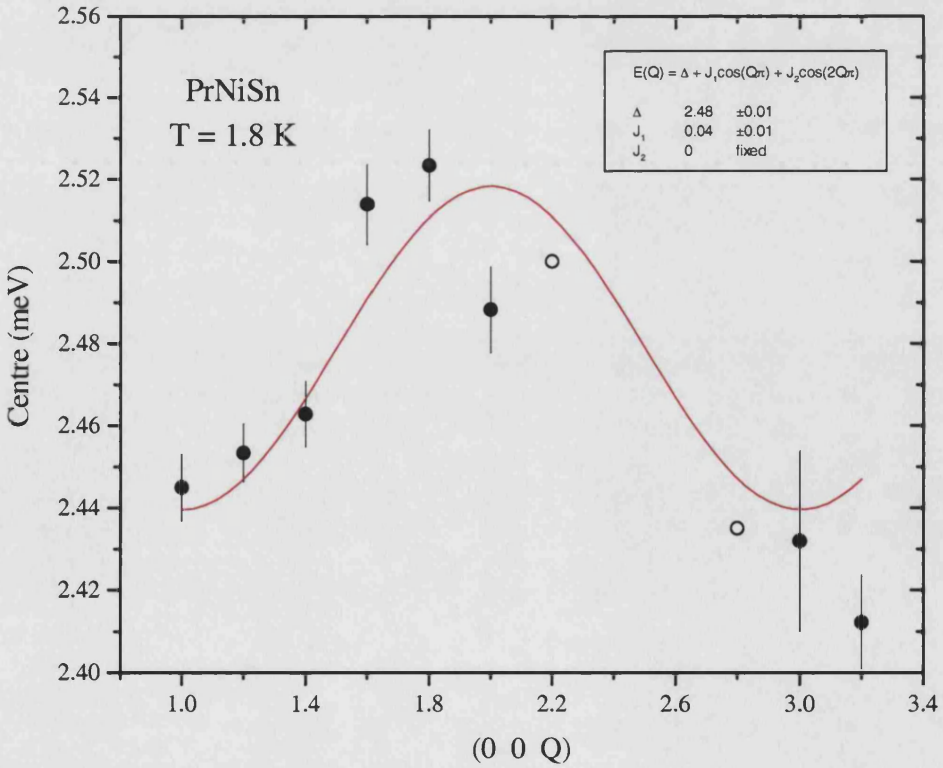

Figure 5.18 Dispersion of the 2.5 meV mode along [0 0 **Q**] and fit to the singlet-singlet model.

5.3.3 3.5 meV mode

H	K	L	Centre (meV)	Step (meV)	No. of Points	Monitor (counts)	Temperature (K)
2	0	0	3.45	0.1	7	2×10^6	1.6
2	0	0	3.4	0.1	15	2×10^6	1.6
2.25	0	0	3.55	0.1	9	2×10^6	1.6
2.25	0	0	3.4	0.1	15	2×10^6	1.6
2.5	0	0	3.6	0.05	25	2×10^6	1.7

Table 5.7 Summary of the scans made on the 3.5 meV mode.

5.3.3.1 [Q 0 0] direction

In order to determine whether the upper mode along the (**Q** 0 0) direction follows the theoretical curve predicted from the dispersion of the other 3.5 meV modes, scans were made at three positions along the curve using long counting times and a small step size to improve the statistics. It is immediately obvious that the peak shapes cannot be described by only one or two gaussians, since at the very least there is a central peak with further peaks either side. Figures 5.19 and 5.20 show fits using three and four gaussian peaks. In both cases, the widths of the gaussians have been fixed to be the instrumental resolution of 0.2 meV (as obtained from measurements on the vanadium standard sample).

The (2 0 0) peak is fitted equally well using three or four gaussians, with a large central peak and smaller peaks either side. Again, fits to the (2.25 0 0) peak are adequate in both cases, although the three gaussian fit appears to fit the upper energy part slightly better. Finally, the fits to the (2.5 0 0) peak are essentially identical since two of the gaussians in the four gaussian fit can be superimposed to leave just three gaussians. Note here that there are strong correlations between the various fitting parameters, i.e. a change in one parameter will have a large affect on the remaining ones. This usually means that there are an excessive number of parameters in the fit. Thus, although the 3.5 meV peaks appear to consist of more than two modes, it cannot be determined whether three or four modes are present.

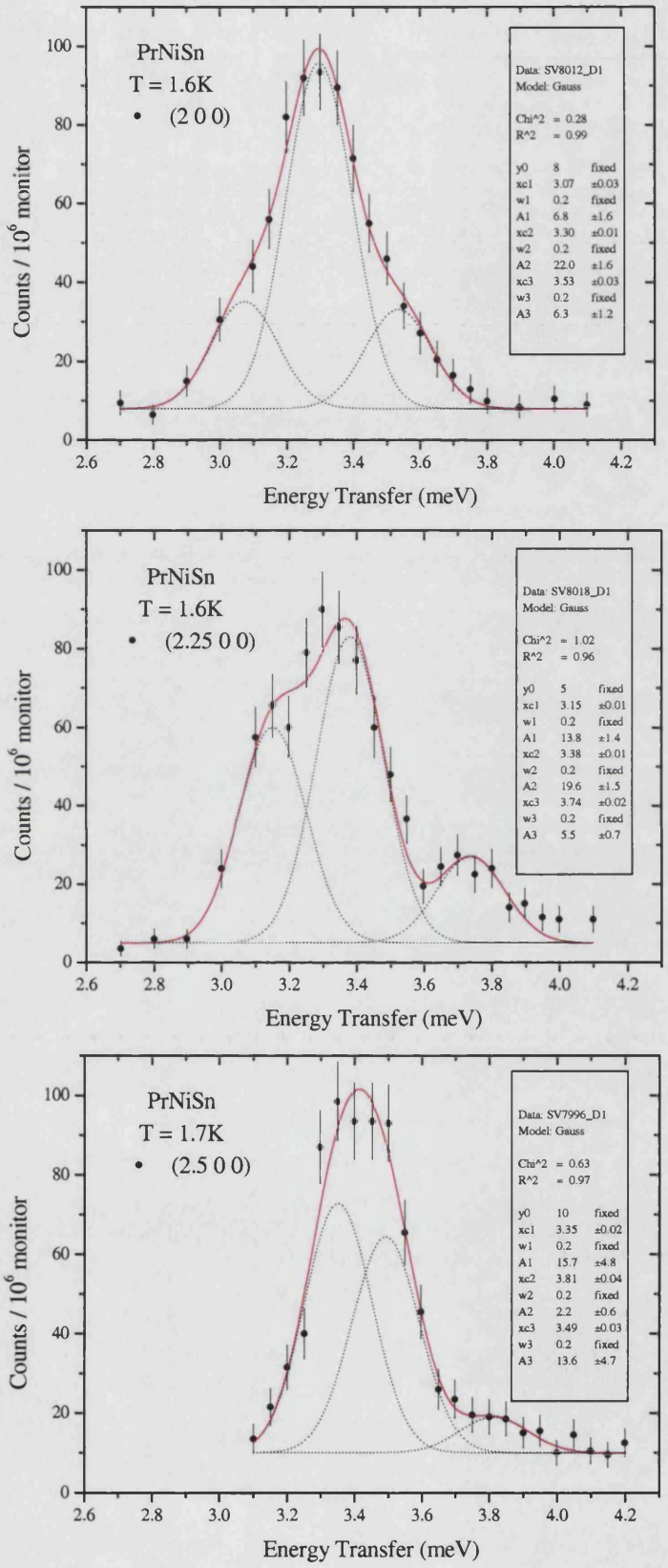

Figure 5.19 Three gaussian fit to the 3.5 meV peak at various positions along the [**Q** 0 0] direction. The solid line is the total fit and the dotted lines are the individual gaussians.

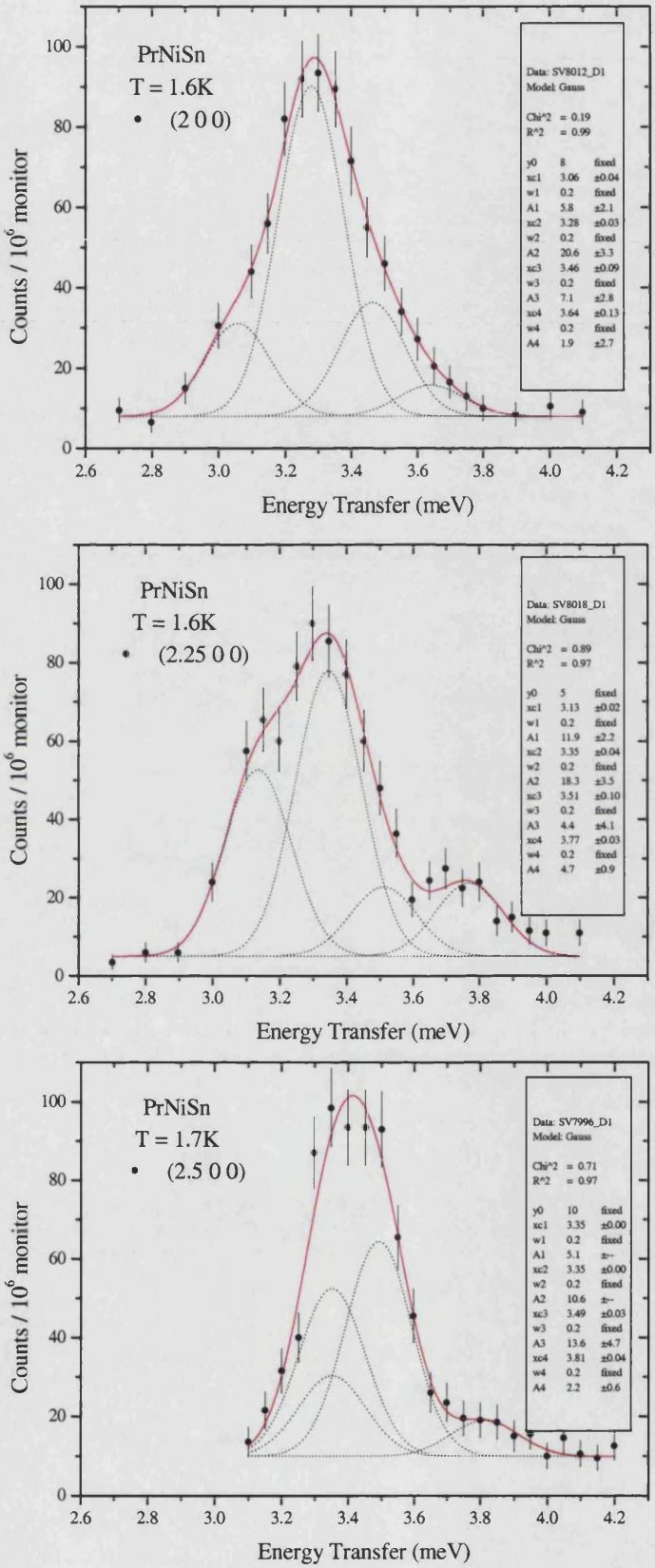

Figure 5.20 Four gaussian fit to the 3.5 meV peak at various positions along the [**Q** 0 0] direction. The solid line is the total fit and the dotted lines are the individual gaussians.

In order for a comparison to be made with the previous data on the 3.5 meV excitation, however, fits to the new data were made using two gaussians only. One of the peaks was fitted to the intense lower energy part and the other fitted to the weaker higher energy shoulder. An example of one of the two gaussian fits is shown in Figure 5.21. In addition to this, the previous V2 data was refitted to ensure that the same fitting method was used for all of the available data.

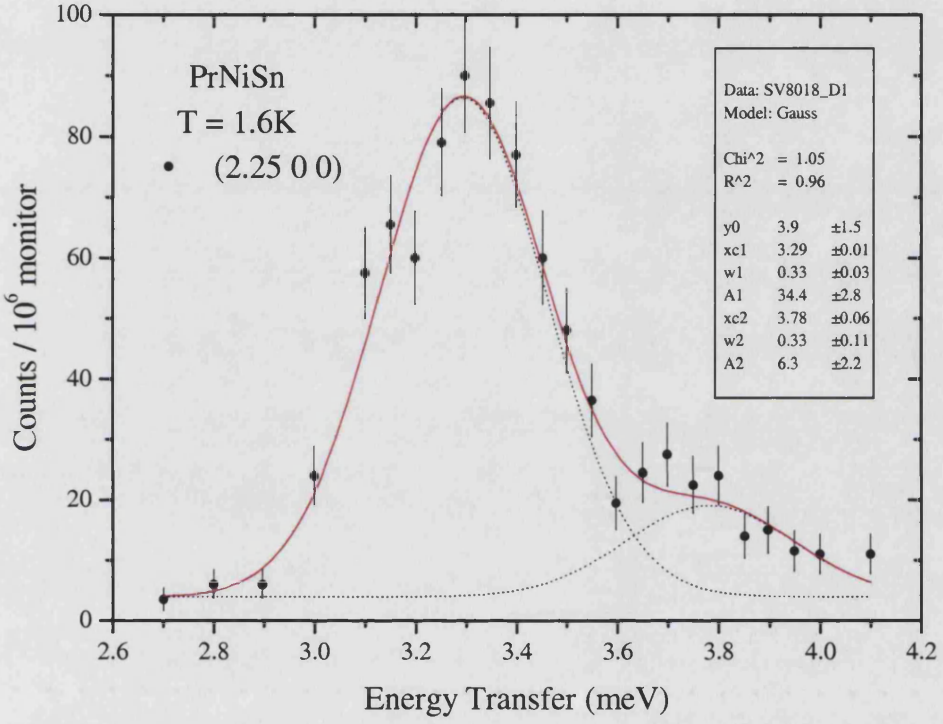

Figure 5.21 Two gaussian fit to the 3.5 meV peak at (2.25 0 0)

5.3.3.2 Comparison of [0 0 Q] and [Q 0 0]

The dispersion relations obtained from the refitted data, as well as the new measurements, are shown in Figures 5.22 and 5.23. In both symmetry directions a next-nearest-neighbour interaction must be included in order to fit the data satisfactorily. However, in the [0 0 **Q**] direction the two modes are out-of-phase with each other whereas in the [**Q** 0 0] direction the two modes move in-phase.

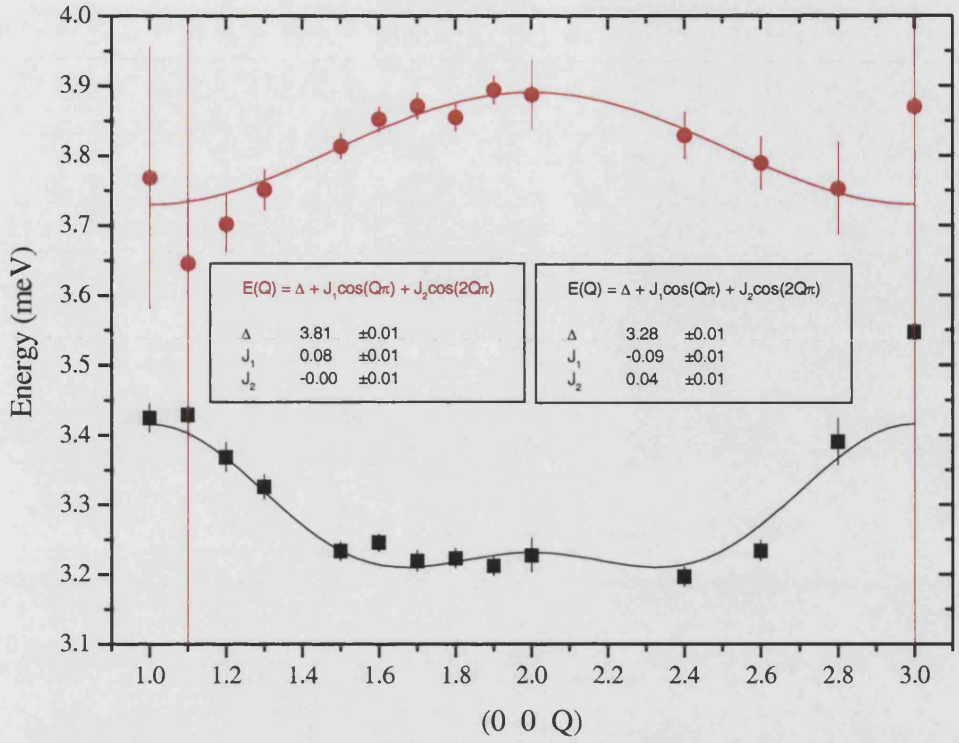

Figure 5.22 Dispersion of the 3.5 meV modes along [0 0 **Q**] and fit to the singlet-singlet model.

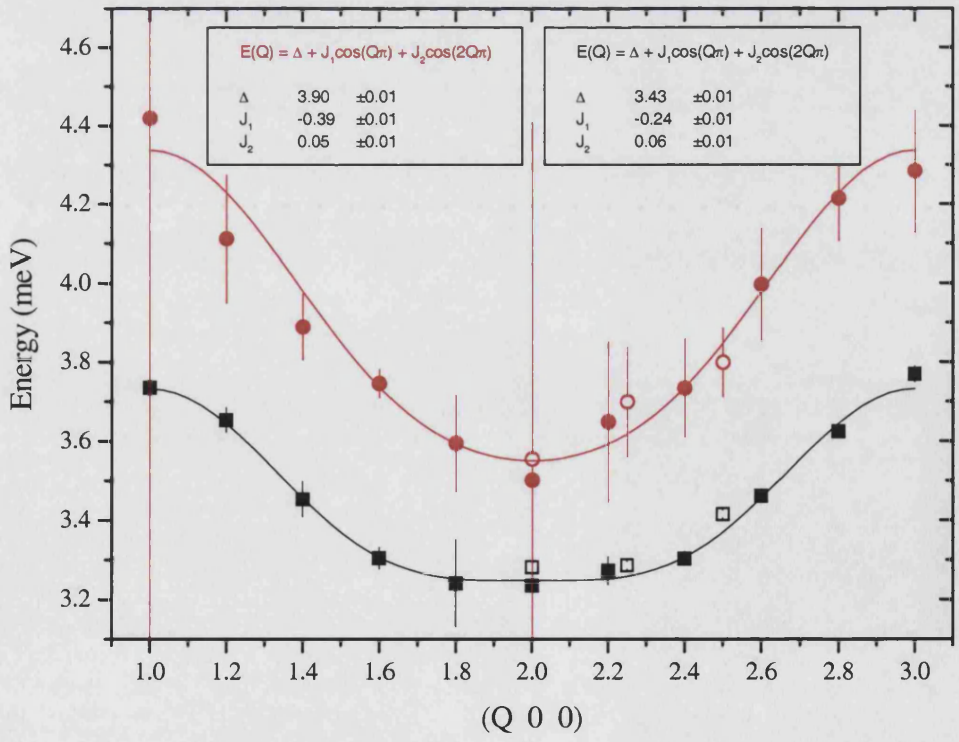

Figure 5.23 Dispersion of the 3.5 meV modes along [**Q** 0 0] and fit to the singlet-singlet model. Note that the open points are the data taken in the experiment reported in this thesis.

5.3.4 5.2 meV mode

H	K	L	Centre (meV)	Step (meV)	No. of Points	Monitor (counts)	Temperature (K)
0	0	1.5	5.4	0.2	7	10^6	1.7
0	0	2	5.4	0.2	9	10^6	1.7
0	0	2	5.2	0.2	13	10^6	1.7
0	0	3	5.4	0.25	5	10^6	1.7
1.5	0	0	5.2	0.2	7	10^6	1.8
1.5	0	0	5.2	0.1	17	2×10^6	1.6
1.75	0	0	5.2	0.1	15	2×10^6	1.6
2	0	0	5.4	0.2	7	10^6	1.7
2	0	0	5.2	0.1	15	2×10^6	1.6
2.25	0	0	5.2	0.1	15	2×10^6	1.6
2.5	0	0	5.2	0.1	17	2×10^6	1.6
2.75	0	0	5.2	0.2	9	2×10^6	1.6
3	0	0	5.2	0.2	7	10^6	1.8
3	0	0	5.2	0.1	15	2×10^6	1.6

Table 5.8 Summary of the scans made on the 5.2 meV mode.

5.3.4.1 [Q 0 0] direction

Measurements of the 5.2 meV mode were made at various positions along the [**Q** 0 0]. A typical gaussian fit to the data is shown in Figure 5.24 for the (3 0 0) position. The complete series of measurements direction is shown in Figure 5.25. It can be seen this mode exhibits very little dispersion.

5.3.4.2 [0 0 Q] direction

The statistics of the data in the [0 0 **Q**] direction are very poor, although tentative fits have been made. The peak positions are further away from the 5.18 meV line compared to the [**Q** 0 0] direction, but from the data it is not possible to determine whether this apparent dispersion is real or not.

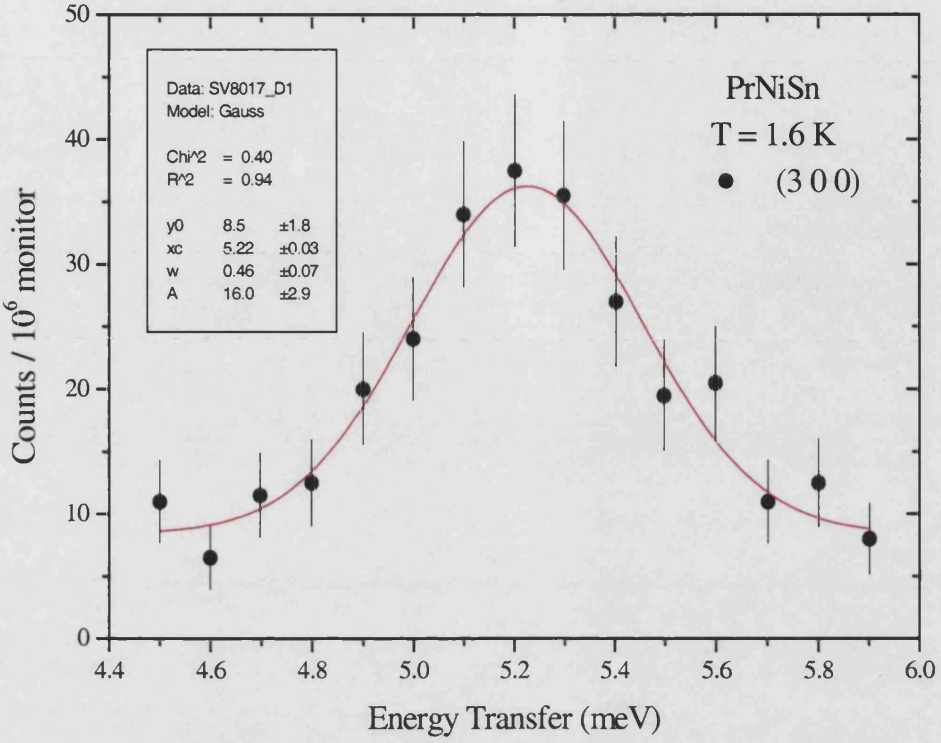

Figure 5.24 An example of the single gaussian fitting technique for the data at (3 0 0).

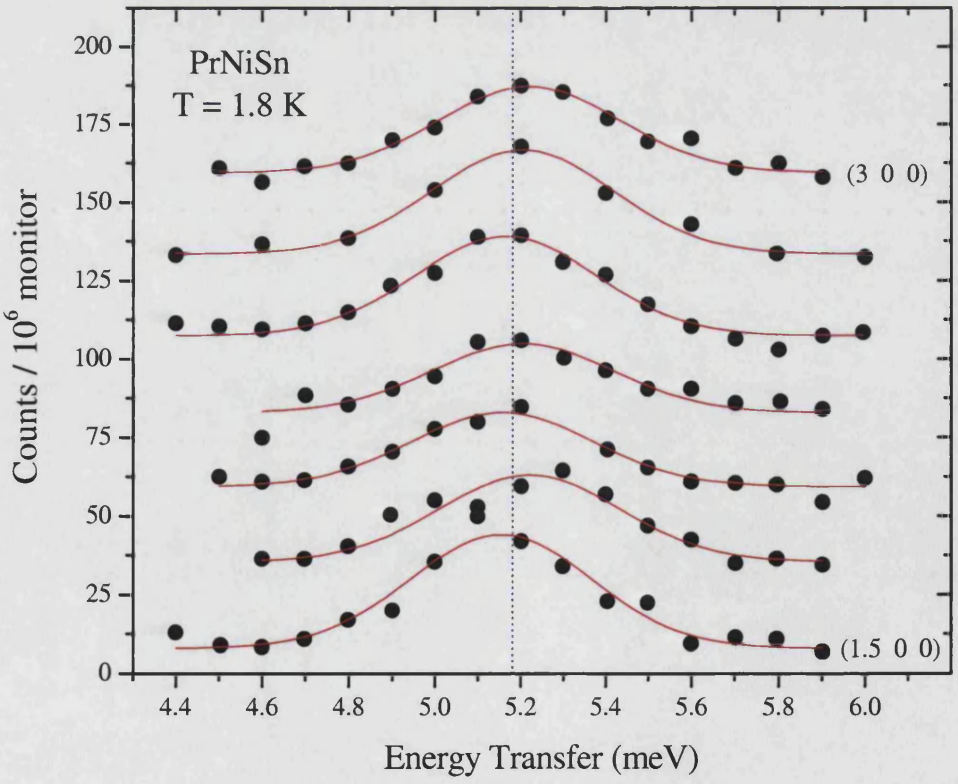

Figure 5.25 Dispersion of the 5.2 meV mode from (1.5 0 0) at the bottom to (3 0 0) at the top. Note that each scan has been offset by 25 counts and that there is little dispersion.

5.3.5 Summary of polarisations and dispersion

The amplitude of the 1.5 meV mode reaches a maximum of around 170 counts along the [0 0 **Q**] direction, compared to a maximum of around 15 counts in the [**Q** 0 0] direction. This suggests that the 1.5 meV mode is polarised along the *c*-axis. The dispersion along [0 0 **Q**] is due to nearest-neighbours only and is centred at (2 0 0).

The 2.5 meV mode may also be polarised along the *c*-axis since the peak amplitude at (0 0 1) is 80 counts compared to only 5 counts at the (1 0 0) position. More measurements along the [**Q** 0 0] direction are required to clarify this however. Again, it exhibits a nearest-neighbour dispersion along [0 0 **Q**] and appears to be centred at (0 0 2).

In contrast, the 3.5 meV modes have similar amplitudes along both the [0 0 **Q**] and [**Q** 0 0] directions, reaching a maximum of around 125 counts in both directions. This indicates that the 3.5 meV modes are polarised along the *b*-axis. The dispersion of the two modes along the [0 0 **Q**] and [**Q** 0 0] directions both require additional next-nearest-neighbour terms, although this coupling is not as strong as the nearest-neighbour coupling.

Finally, the 5.2 meV mode appears to be weakly polarised along the *a*-axis, since the maximum amplitude along the [0 0 **Q**] direction is negligible and that along the [**Q** 0 0] direction is only around 35 counts. It does not seem to exhibit dispersion along either of the [0 0 **Q**] or [**Q** 0 0] directions.

Summaries of the dispersion relations obtained along the [0 0 **Q**] and [**Q** 0 0] directions are shown in Figures 5.26 and 5.27, respectively.

5.3.5.1 Dispersion along the [0 0 Q] direction

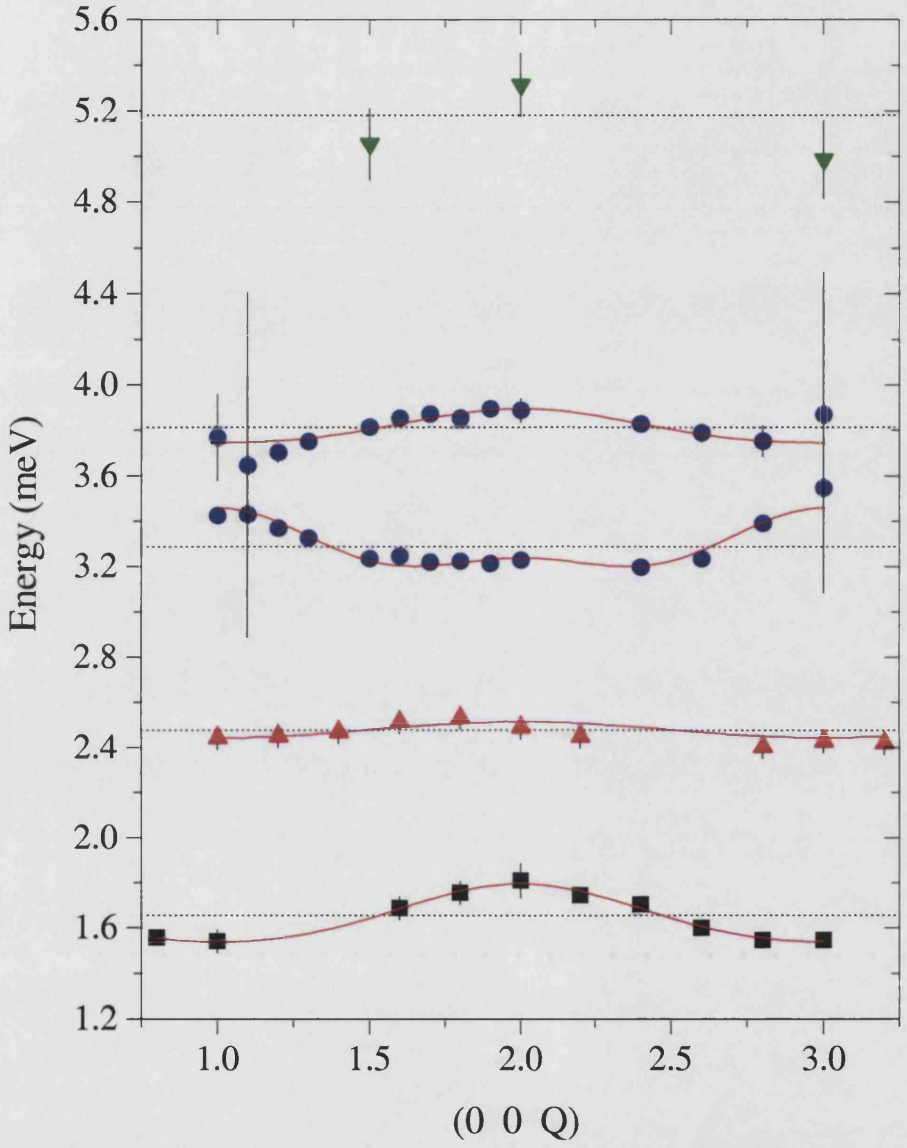

Figure 5.26 Comparison of the dispersion of the different modes in PrNiSn along [0 0 **Q**].

$$E(\mathbf{Q}) = \Delta + J_1 \cos(\mathbf{Q}\pi) + J_2 \cos(2\mathbf{Q}\pi)$$

Δ	J_1	J_2
1.65 ± 0.01	0.13 ± 0.01	-
2.48 ± 0.01	0.04 ± 0.01	-
3.28 ± 0.01	-0.09 ± 0.01	0.04 ± 0.01
3.81 ± 0.01	0.08 ± 0.01	0.00 ± 0.01
5.18 ± fixed	-	-

Table 5.9 Dispersion parameters for the [0 0 **Q**] direction. (All units are in meV.)

5.3.5.2 Dispersion along the [Q 0 0] direction

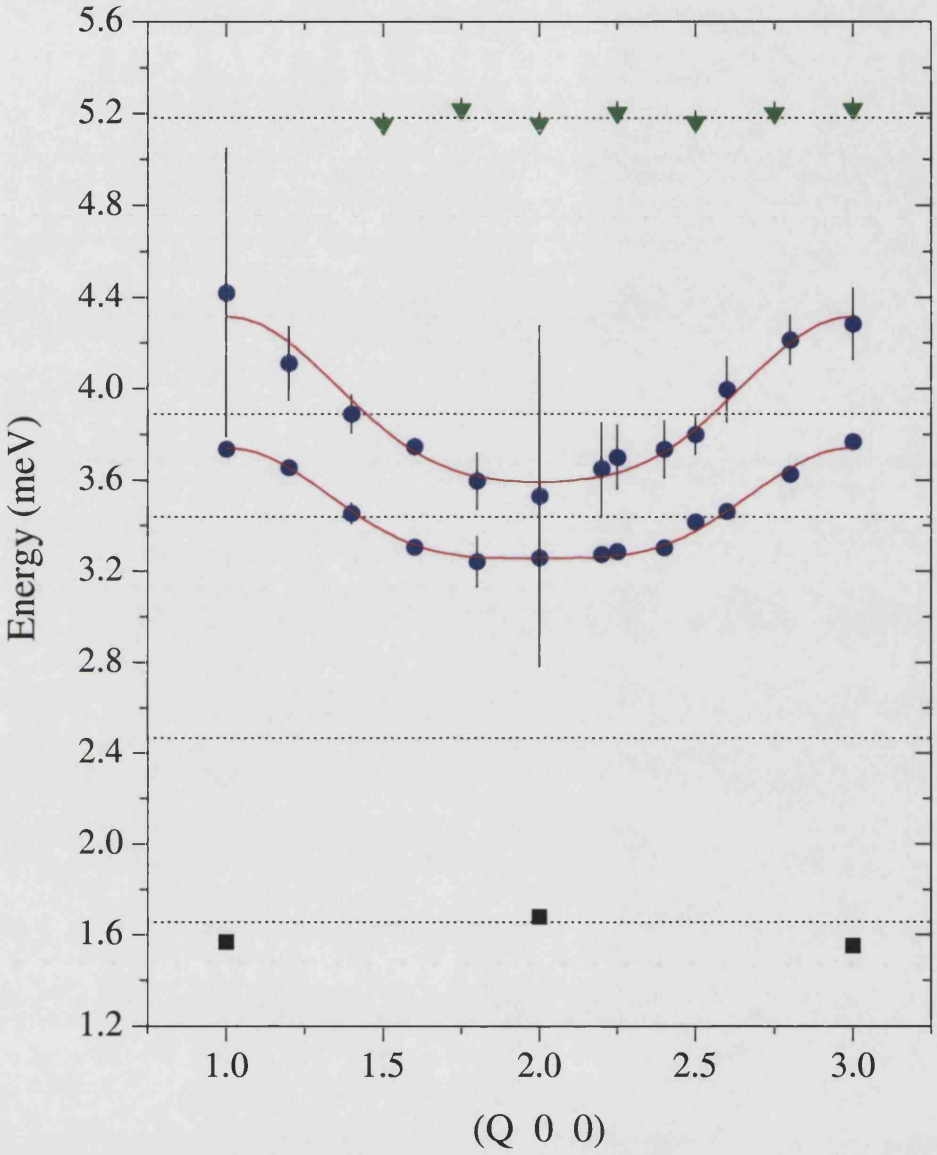

Figure 5.27 Comparison of the dispersion of the different modes in PrNiSn along [**Q** 0 0].

$$E(\mathbf{Q}) = \Delta + J_1 \cos(\mathbf{Q}\pi) + J_2 \cos(2\mathbf{Q}\pi)$$

Δ	J_1	J_2
1.65 ± fixed	-	-
2.48 ± fixed	-	-
3.43 ± 0.01	-0.24 ± 0.01	0.06 ± 0.01
3.90 ± 0.01	-0.39 ± 0.01	0.05 ± 0.01
5.18 ± fixed	-	-

Table 5.10 Dispersion parameters for the [**Q** 0 0] direction. (All units are in meV.)

Numerous attempts were made at refitting the HET data in order to obtain an energy level scheme with levels at 1.5 and 2.5 meV. Then, after discussions with Prof. Jens Jensen, we found that it is likely that, just as the two modes at 3.3 and 3.8 meV arise from the predicted 3.5 meV level, so the 1.5 and 2.5 meV modes may arise from the level predicted at 2 meV.

This view was prompted by the data at (0 0 1) and (0 0 3) which was taken at T = 2 K. As can be seen in Figure 5.28, the modes at 1.5 and 2.5 meV seem to have an anti-phase relationship with the peak at 1.5 meV being much more intense at (0 0 3) whilst the 2.5 meV peak is more intense at (0 0 1). If this is the case, then the level at 2 meV calculated from the HET data fits in extremely well.

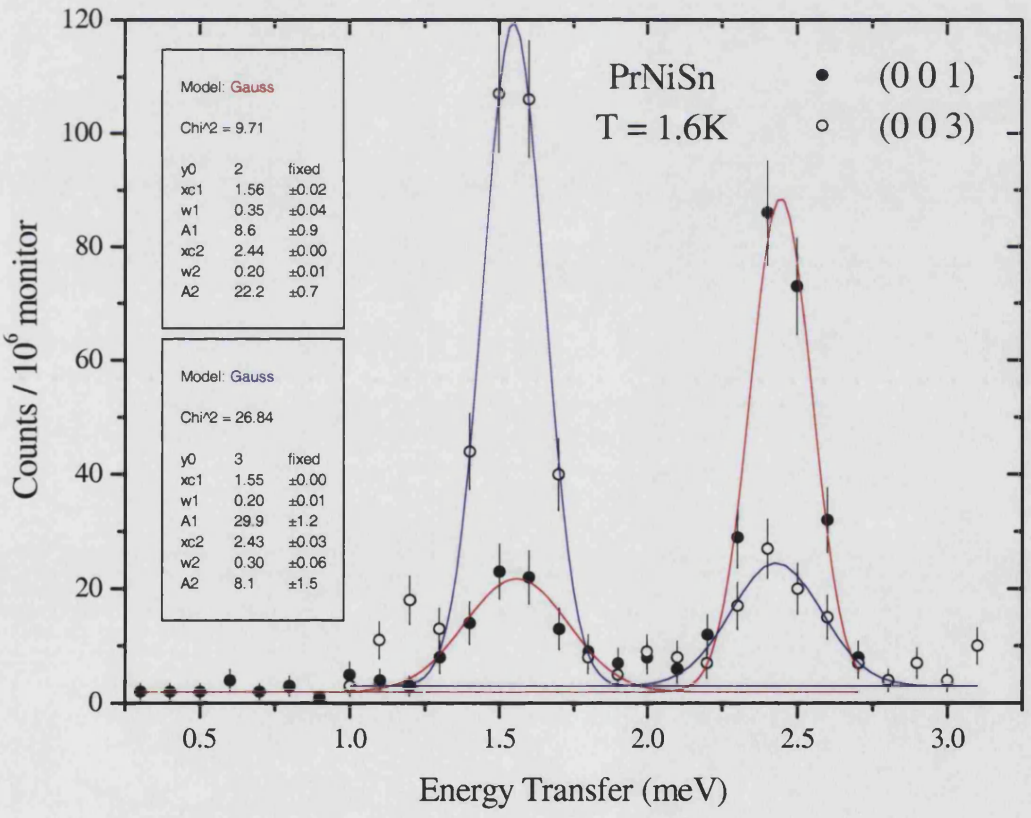

Figure 5.28 Comparison of the 1.5 meV and 2.5 meV modes at (0 0 1) and (0 0 3). Note the anti-phase relationship between the two modes.

Since there are 4 atoms per unit cell in PrNiSn, we can assume that there should be 4 different modes for each energy level. This is because all of the atoms in the unit cell have the same site symmetry, which means that each experiences the same crystalline electric field

If we look at the phase relationship between one of the atoms and the remaining three, we can visualise the different modes as either *acoustic* (where the atoms are *in-phase*) or *optic* (where the atoms are *out-of-phase*). This means that we would expect there to be four possible modes for each energy level as shown below.

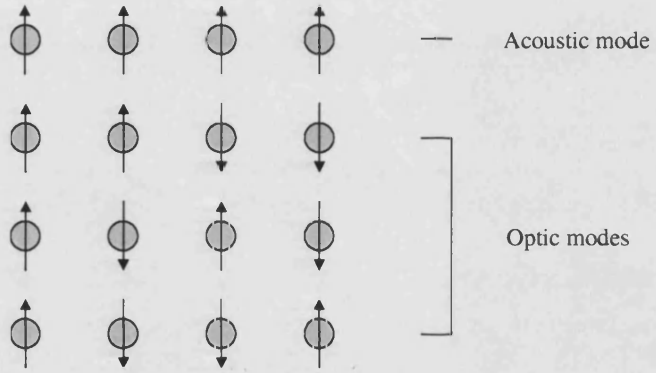

This assumes that all of the atoms act independently and in this case we would have a nearest-neighbour coupling of:

$$J = J_s \pm J_a \pm J_b \pm J_c$$

where J_s is the coupling between a given ion and the equivalent in the next unit cell, and J_a, J_b, J_c are the coupling between the same ion and the remaining three ions in the unit cell.

If, however, there are two sublattices, *a* and *b*, each comprising two atoms of the unit cell we would expect to see only two modes, i.e. one acoustic and one optic.

If we assume that this is the case for PrNiSn, then the J_1 and J_2 parameters we have obtained are related to the inter- and intra-sublattice couplings via:

$$J_1 = J_{1aa} \pm J_{1ab} \quad \text{and} \quad J_2 = J_{2aa} \pm J_{2ab}$$

Then, assuming that the acoustic branch in each direction is the lower energy of the two modes (which is usual for acoustic modes) we obtain the following couplings along [0 0 **Q**] for the 3.5 meV level:

$$\begin{aligned} J_{1aa} &= -0.01 \pm 0.01 \\ J_{1ab} &= -0.09 \pm 0.01 \end{aligned} \quad \text{and} \quad \begin{aligned} J_{2aa} &= +0.02 \pm 0.01 \\ J_{2ab} &= +0.02 \pm 0.01 \end{aligned}$$

and similarly along [**Q** 0 0] for the 3.5 meV level, we obtain:

$$\begin{aligned} J_{1aa} &= -0.32 \pm 0.01 \\ J_{1ab} &= +0.08 \pm 0.01 \end{aligned} \quad \text{and} \quad \begin{aligned} J_{2aa} &= +0.06 \pm 0.01 \\ J_{2ab} &= +0.01 \pm 0.01 \end{aligned}$$

where J_{1aa} and J_{2aa} are the couplings between atoms on the same sublattice, respectively, and J_{1ab} and J_{2ab} are the couplings between atoms on different sublattices. From this we can see that the nearest-neighbours tend to couple antiferromagnetically, whereas the next-nearest-neighbours tend to couple ferromagnetically. Note the strong antiferromagnetic coupling, J_{1aa}, between nearest-neighbour atoms on the same lattice in the [**Q** 0 0] direction.

5.4 Calculations

Using a FORTRAN program written by the author and the Stevens parameters deduced from fitting to the inelastic polycrystalline data, calculations of the susceptibility, magnetisation and heat capacity were performed along each of the main symmetry directions. In the calculations shown in Figures 5.29, 5.31 and 5.32, the z-, y- and x-axes correspond to the a-, b- and c-directions, respectively. Comparisons to the experimental susceptibility are shown in Figure 5.33.

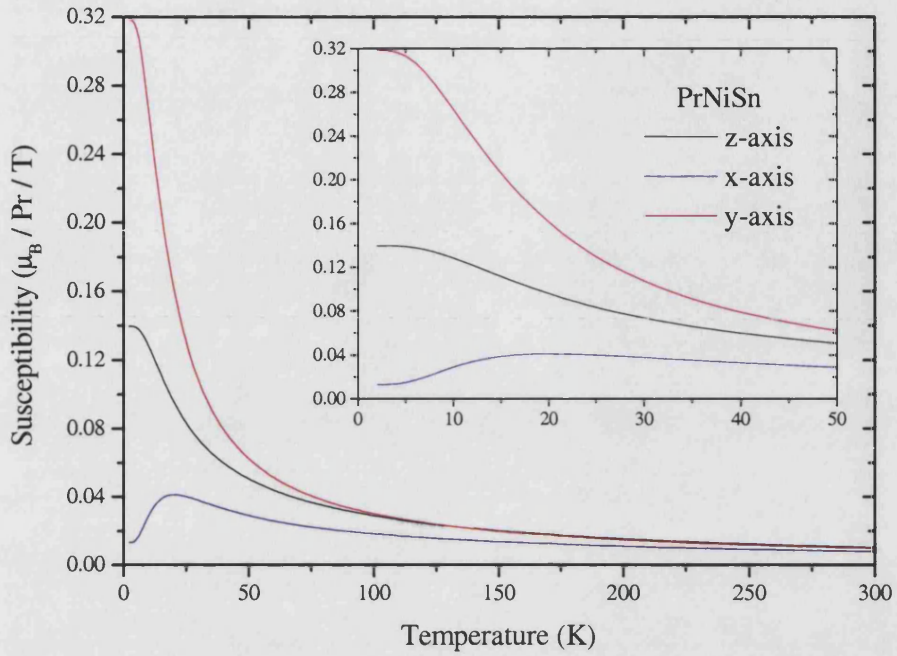

Figure 5.29 Calculation of the susceptibility of PrNiSn using the CEF Hamiltonian and Stevens parameters discussed in the text.

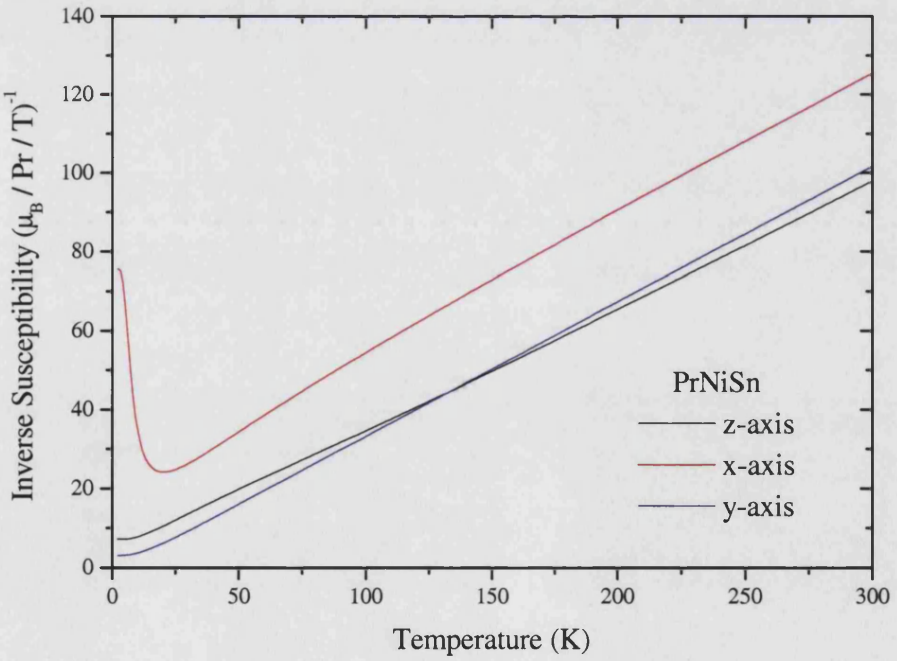

Figure 5.30 Calculation of the inverse susceptibility of PrNiSn using the CEF Hamiltonian and Stevens parameters discussed in the text.

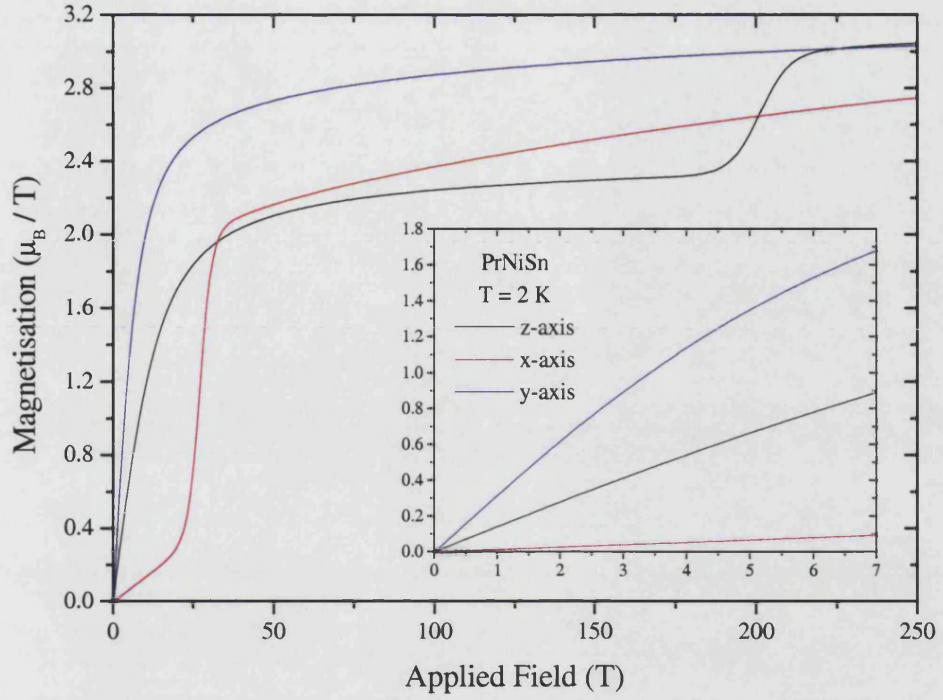

Figure 5.31 Calculation of the magnetisation of PrNiSn using the CEF Hamiltonian and Stevens parameters discussed in the text.

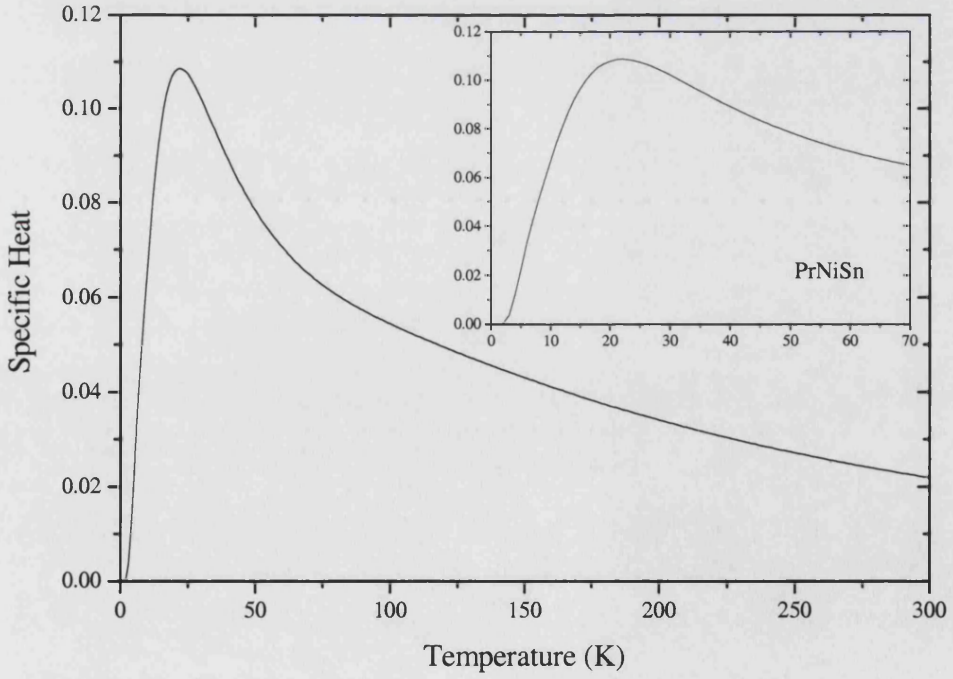

Figure 5.32 Calculation of the heat capacity of PrNiSn using the CEF Hamiltonian and Stevens parameters discussed in the text.

5.4.1 Comparison with experiment

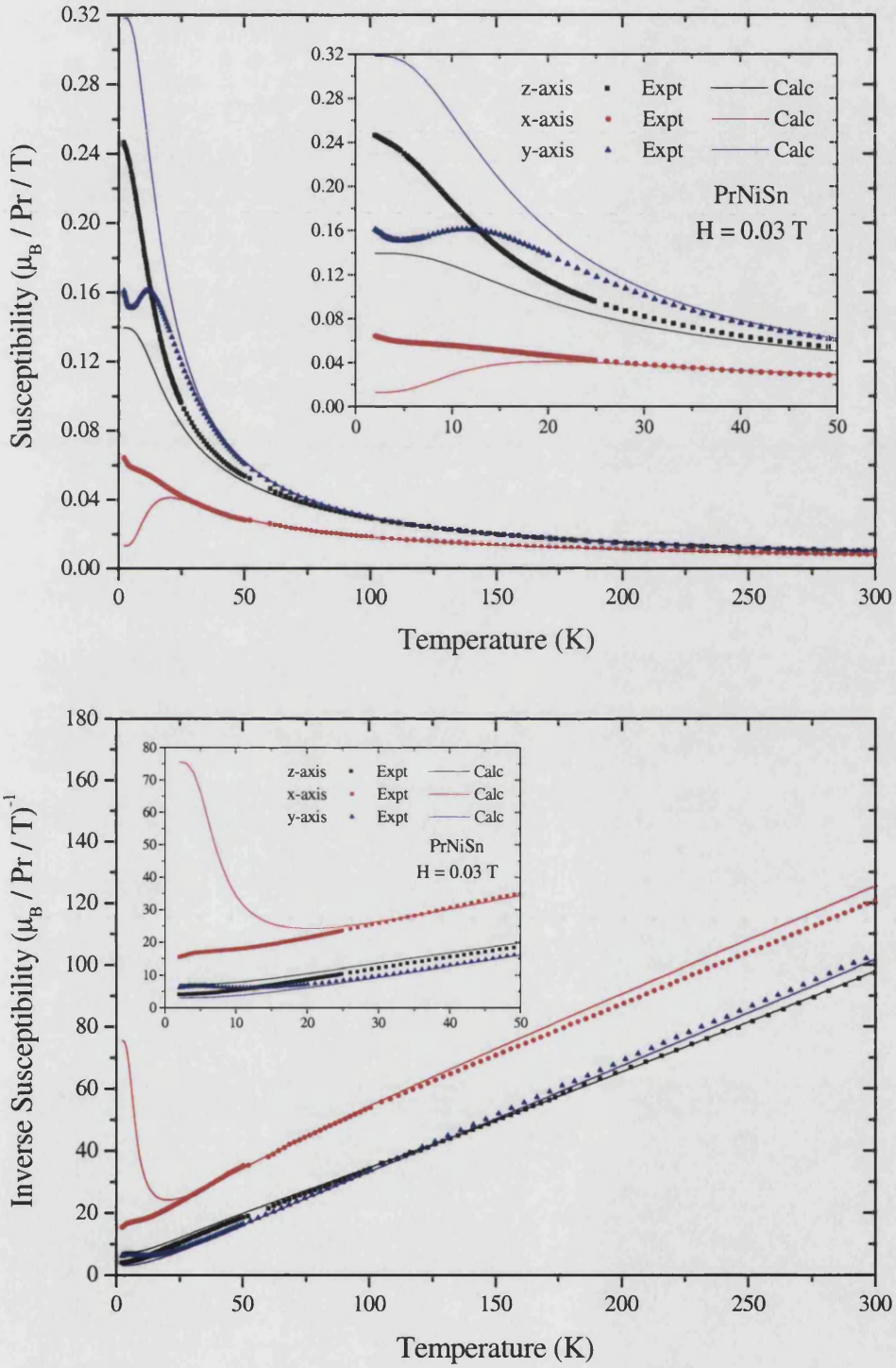

Figure 5.33 Comparison of the experimental and calculated values for the susceptibility and inverse susceptibility of PrNiSn. The calculated curves were obtained using the Stevens parameters determined by FOCUS.

5.5 NdNiSn

From inelastic neutron scattering performed on polycrystalline NdNiSn, excitations were observed around energies of 5.4, 11.4, 16 and 24.2 meV. Thus, using the same V2 setup as for PrNiSn we would expect to be able to see the level at 5.3 meV and an absence of any excitations below this energy.

Preliminary measurements on a single crystal of NdNiSn revealed no excitations below 2.5 meV at either (1 0 0) or (0 0 1) (see Figure 5.34). However, an excitation at around 5.5 meV is visible in both the [0 0 **Q**] and [**Q** 0 0] directions (see Figures 5.35 and 5.36). There is a slight shift in the peak between (2 0 0) and (3 0 0) but less of a shift between (0 0 2) and (0 0 3).

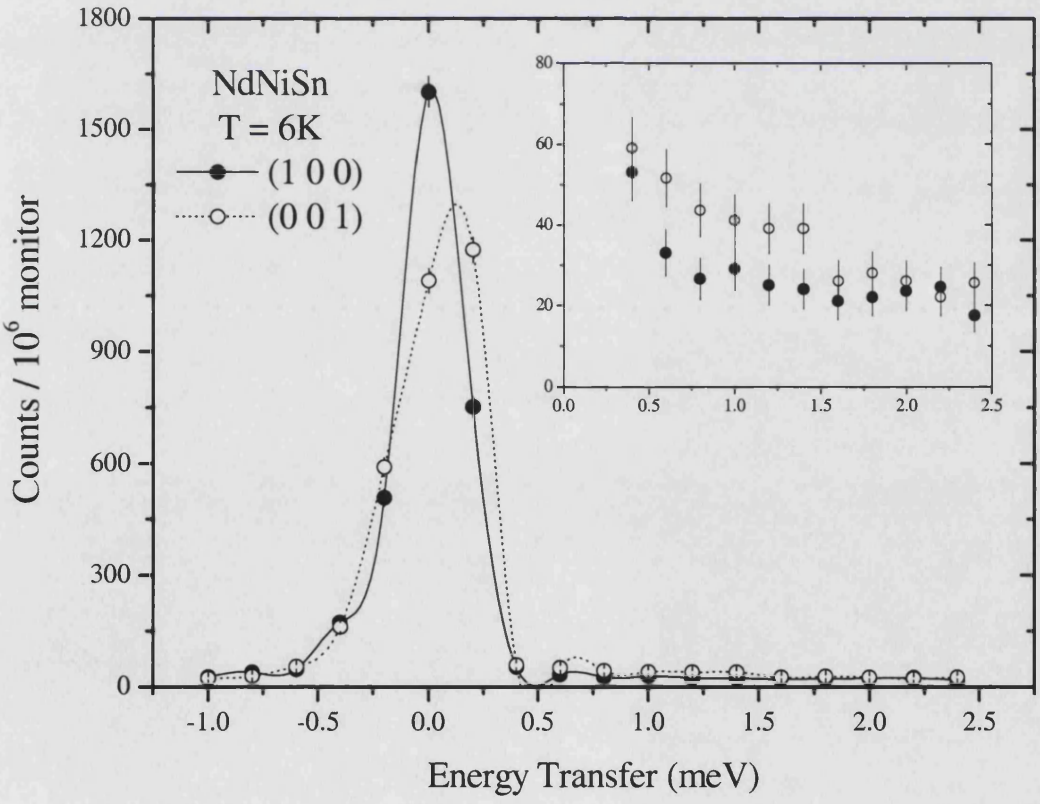

Figure 5.34 Inelastic neutron scattering from NdNiSn at (1 0 0) and (0 0 1) with a spline fit as a guide to the eye. Inset: close-up of the scattering below 2.5 meV.

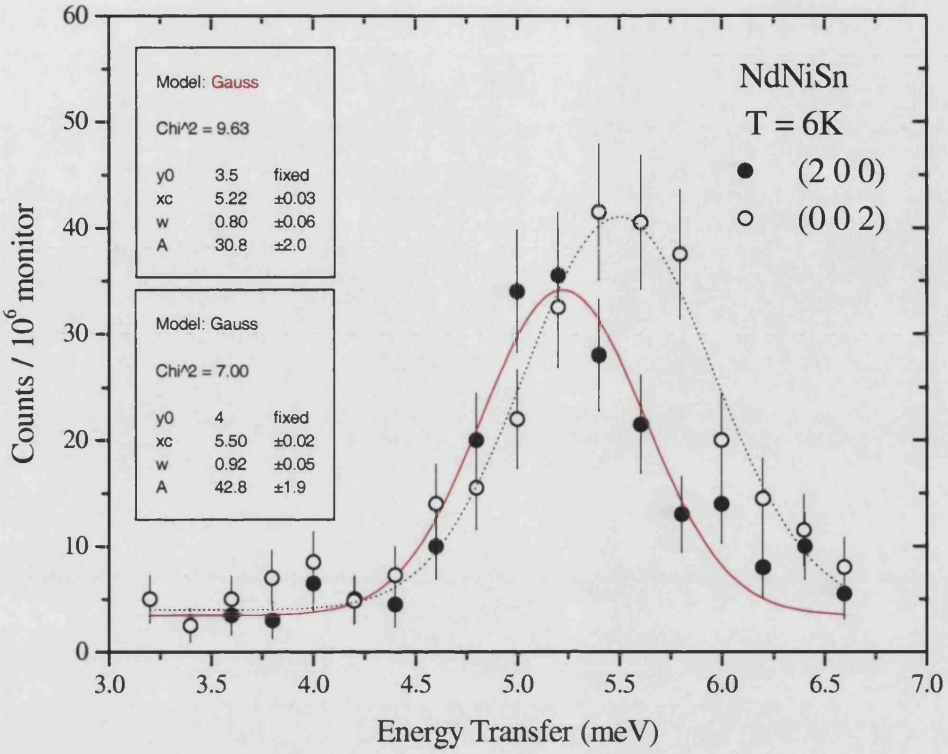

Figure 5.35 The 5.5 meV excitation observed in NdNiSn at (2 0 0) and (0 0 2).

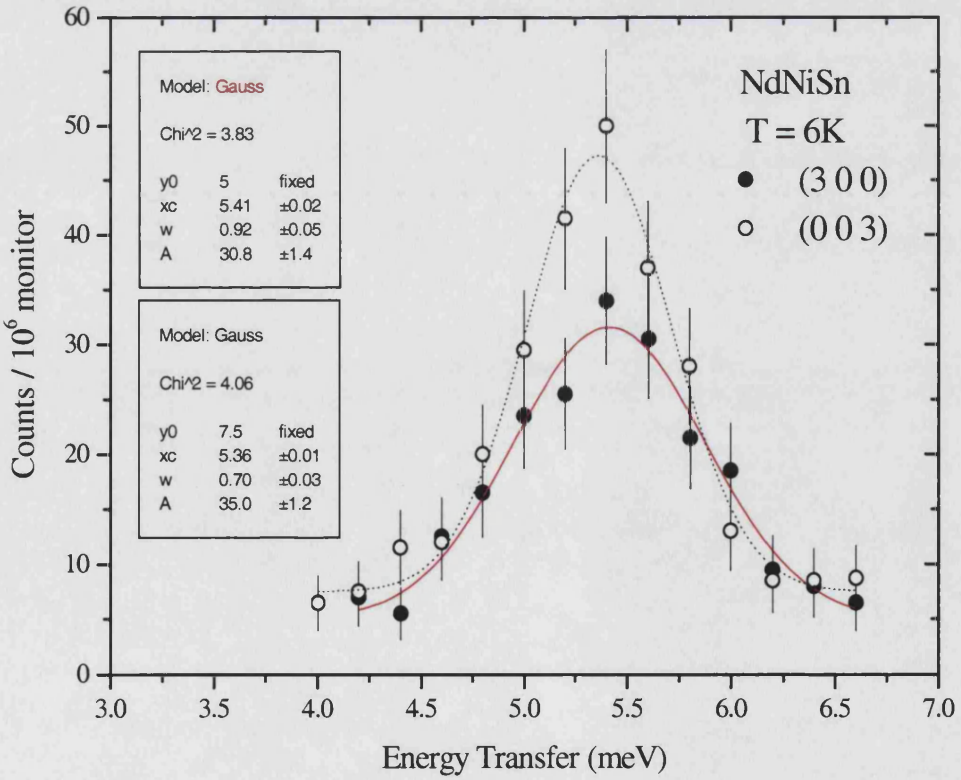

Figure 5.36 The 5.5 meV excitation observed in NdNiSn at (3 0 0) and (0 0 3).

5.6 Conclusions

The inelastic magnetic response of PrNiSn has been measured at various positions in reciprocal space. Four excitations have been found at energy transfers of approximately 1.5, 2.5, 3.5 and 5.2 meV at the (0 0 1) position. Measurements of the dispersion of these modes have been made along the [0 0 **Q**] and [**Q** 0 0] directions.

The 1.5 meV mode exhibits a nearest-neighbour type dispersion along the [0 0 **Q**] direction with an amplitude of 0.13 meV and a period of two units commensurate with the reciprocal lattice. It is strongly polarised along the c^* axis.

The mode at 2.5 meV also exhibits a nearest-neighbour type dispersion in the [0 0 **Q**] direction, but with a smaller amplitude of 0.04 meV. The dispersion also appears to be commensurate with the reciprocal lattice.

An antiphase relationship between the 1.5 meV and 2.5 meV modes suggests that they arise from the 2 meV level predicted from the calculations. A similar assessment of the coupling between nearest-neighbours as for the 3.5 meV level may be possible, but measurements of the dispersion along the [**Q** 0 0] direction would be required to determine these couplings.

Our additional measurements on the 3.5 meV excitation seem to confirm the results deduced from the previous experiment by Beirne *et al.* At least three modes exist at this energy range. Since there are four Pr ions in the unit cell, four modes are expected which is compatible with our measurements.

The dispersion of the upper and lower modes in the [**Q** 0 0] direction are dominated by a nearest-neighbour interaction, whereas their dispersion along the [0 0 **Q**] direction is weaker and requires an additional next-nearest-neighbour interaction. The modes in the [**Q** 0 0] direction are in-phase, whereas the modes in the [0 0 **Q**] direction are out-of-phase.

The 5.2 meV mode is weak with a slight polarisation along the a^* axis. It does not seem to undergo any dispersion along the [**Q** 0 0] direction, remaining at a roughly constant energy transfer of about 5.18 meV.

Preliminary measurements have been made on a single crystal of NdNiSn. The crystal is of poor metallurgical quality, nevertheless excitations have been observed at 5.5 meV at (**Q** 0 0) and (0 0 **Q**) positions with **Q** = 2 and 3.

5.7 References

[1] Rossi *et al.*, J. Less-Common Metals, **107** (1985) 99

[2] E. D. Beirne, PhD Thesis, University College London (2002)

[3] Routsi *et al.*, J. Mag. Mag. Mat, **110** (1992) 317 and **117** (1992) 79

[4] J. Jensen and A. Mackintosh, Rare Earth Magnetism, Oxford Science (1991)

CHAPTER 6

UPdSn

6.1 Literature Review

Following a systematic study of the magnetic properties of various ternary uranium-based compounds by Palstra *et al.*[1], more detailed studies on UPdSn have since been performed. The crystal structure of UPdSn is the ordered ternary GaGeLi-type structure (space group $P6_3mc$) as deduced from neutron[2] and x-ray[3] diffraction experiments. The lattice parameters are a = 4.61 Å and c = 7.31 Å, giving an inter-uranium distance $d_{U\text{-}U} = c/2$ = 3.66 Å, which is above the Hill limit beyond which the localisation of 5*f* moments is expected for uranium compounds.

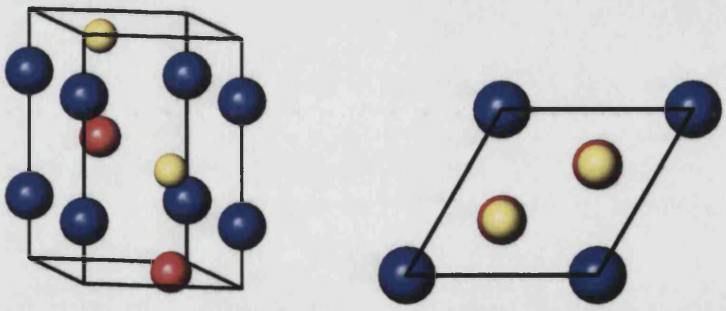

Figure 6.1 The hexagonal GaGeLi-type crystal structure of UPdSn.

Measurements of magnetic susceptibility and magnetisation on single crystals of UPdSn were also performed by de Boer *et al.* (Figure 6.2 a–d). Both are strongly anisotropic, with the hexagonal c axis response being much weaker than the a and b axes. Two distinct anomalies at around 25 and 38 K are seen in the susceptibility data with the higher one attributed to antiferromagnetic ordering. A low temperature spin-flop transition takes place just above B = 3 T.

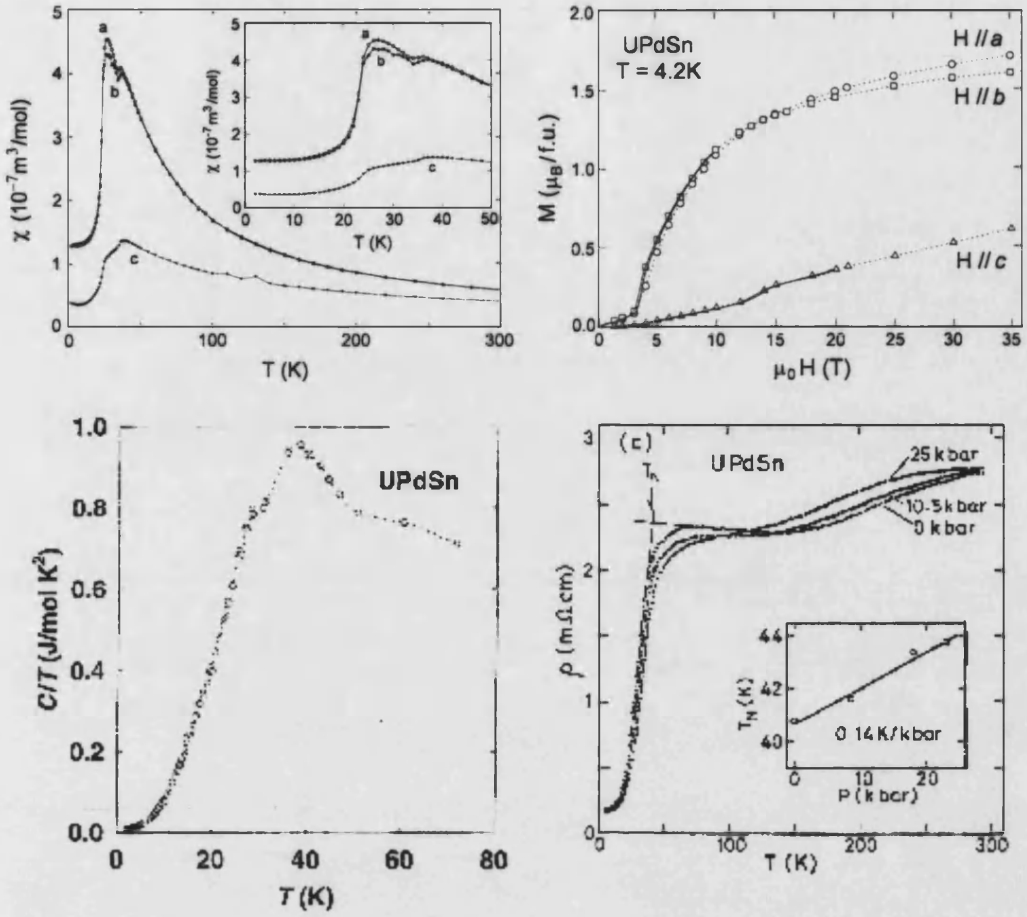

Figure 6.2 Measurements of (a) magnetic susceptibility, (b) magnetisation, (c) specific heat and (d) resistivity for UPdSn.

The effective magnetic moment has been deduced to be $\mu_{eff} = 3.31\mu_B$ and the Curie temperatures to be θ_a = -2.5 K and θ_b = -113 K. The specific heat behaviour of UPdSn is shown in Figure 6.2c and the magnetic transitions are reflected in the shoulder at 27 K and broad maximum at 38 K. Extrapolating to zero temperature gives a very low value of $\gamma \approx 5$ mJ/molK^2, which is of the same order as the localised 5*f* electron compound UPd_3.

Single crystal neutron diffraction experiments in a magnetic field were performed[4,5] by Nakotte *et al.* The complete magnetic phase diagram they obtained is displayed in Figure 6.3 and shows the zero field transitions at 40 and 25 K as well as the low temperature spin flop transition at 3 T.

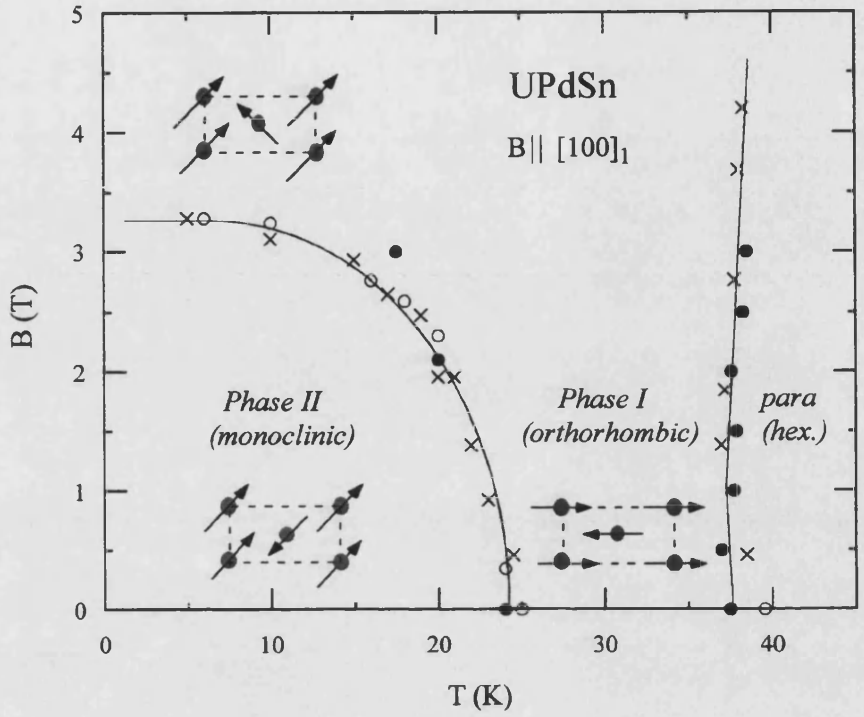

Figure 6.3 The magnetic phase diagram for UPdSn determined from neutron diffraction experiments with a field applied along the *a* axis.

The most recent experiments performed on UPdSn are those of zero-field muon spin relaxation (μSR) by Noakes *et al.*[6] They found that the paramagnetic signal (PM) begins to be replaced near 42 K by another signal which indicates an inhomogeneous magnetic freezing process. Oscillations indicating long-range magnetic ordering appear at 40 K (AFM I), but a remnant of the paramagnetic signal persists until 37 K. Then, below 27 K, a higher frequency signal grows at the expense of the original one until, at 22 K, the entire sample has the second type of long-range ordering (AFM II). The observation that fluctuations exist above the ordering temperatures suggests that the two magnetic transitions are second order.

6.2 Experimental Procedure

The problem of multiple phases is well-known in UTX compounds. To try and obtain a single-phase sample and to ensure high metallurgical quality single crystals were grown, since the number of defects is lower than in a polycrystalline sample. The six single crystals of UPdSn were grown by Heinz Nakotte and colleagues in the University of Amsterdam and were sent to us with their *c*-axes aligned. Unfortunately, due to the large amount of varnish used to fix them in place, the background scattering was too strong. The varnish was therefore cleaned off the crystals by soaking them in acetone. The crystals weighing 5.81 g were then wrapped in aluminium foil and clamped between cadmium strips so that their *c*-axes were approximately parallel (since there was insufficient time to align them accurately). This arrangement was attached to the sample stick so that the crystals lay horizontally (see Figure 6.4) and the CCR was then connected.

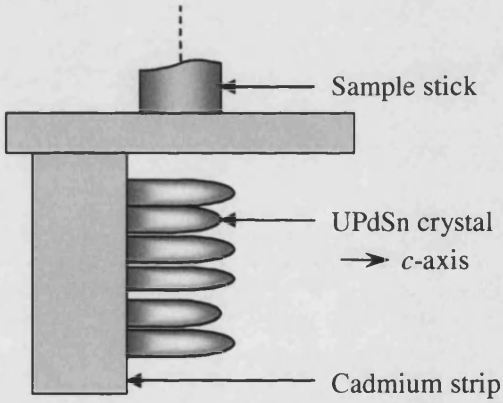

Figure 6.4 Schematic diagram of the arrangement of the UPdSn single crystals.

An initial scan was made with an incident energy of 100 meV at a temperature of 66 K. Measurements were then made at various temperatures using 80 meV neutrons. A scan using 42 meV neutrons was then performed to look for evidence of low energy excitations. Following this, measurements at 23 meV were taken at various temperatures above and below the 25 K transition. Finally, high incident energy (800 meV) neutron measurements were made at low (50 K) and high (300 K) temperatures in order to look for intermultiplet excitations.

Run number	Incident Energy (meV)	Chopper Speed (Hz)	Sample Temp (K)	Total μA hr	Sample
11944	White beam	-	300		Vanadium
11991	23	150	10	2000	UPdSn
12013	23	150	22	1000	UPdSn
12014	23	150	28	411	UPdSn
11989	42	150	10	2000	UPdSn
11984	80	300	10	2000	UPdSn
11992	80	300	19	2000	UPdSn
12012	80	300	22	1000	UPdSn
11983	80	300	28	2000	UPdSn
11993	80	300	35	2000	UPdSn
11986	80	300	41	2000	UPdSn
11987	80	300	50	2000	UPdSn
11982	80	300	66	2000	UPdSn
11988	80	300	100	2000	UPdSn
11996	80	300	200	1680	UPdSn
11981	100	150	66	2790	UPdSn
11995	800	600	50	1500	UPdSn
11997	800	600	300	3400	UPdSn

Table 6.1 Summary of the first set of scans performed on UPdSn.

Following this initial experiment, further beam time was scheduled to look at low energy excitations below 30 meV. In this experiment, neutrons with an incident energy of 36 meV were used to look at the low energy magnetic scattering above and below the two transition temperatures. During this experiment, a 5.77 g polycrystalline sample of ThPdSn was also measured at energies of 36, 80 and 800 meV so that phonon subtractions could be made more accurately.

Run number	Incident energy (meV)	Chopper speed (Hz)	Sample temp (K)	Total μA hr	Sample
12292	White beam	-	300		Vanadium
12332	36	150	6	2000	UPdSn
12333	36	150	28	1846	UPdSn
12335	36	150	50	2000	UPdSn
12336	36	150	19	1893	UPdSn
12337	36	150	6	2000	ThPdSn
12338	36	150	50	1400	ThPdSn
12339	36	150	19	1400	ThPdSn
12340	80	300	50	1000	ThPdSn
12341	800	600	50	570	ThPdSn

Table 6.2 Summary of the second set of scans performed on UPdSn.

6.3 Results & Discussion

The initial E_i = 100 meV scan revealed a strong, broad peak of magnetic scattering centred around an energy transfer of 40 meV. We therefore repeated the measurement at a lower incident energy of 80 meV to improve resolution. The resolution at 40-50 meV with E_i = 80 meV is ~1.4 meV compared to a resolution of ~1.9 meV with E_i = 100 meV. A series of such measurements were then carried out at various temperatures above and below each of the transitions.

In order to estimate the scattering due to phonons, the data from the high angle banks was initially scaled down by a factor of 4.5. Following the subsequent measurements on ThPdSn, the phonon contribution was determined using the ratio method. The procedure used to obtain this contribution is outlined in Chapter 4. The ratio obtained in this way is close to 1/5 over a wide range and lies between 1/5 and 1/4 in the 10 to 60 meV range. Outside this region the ratio begins deviate severely, as shown by the fourth order polynomial fit. Therefore only the magnetic data between 10 and 60 meV can be considered as reliable.

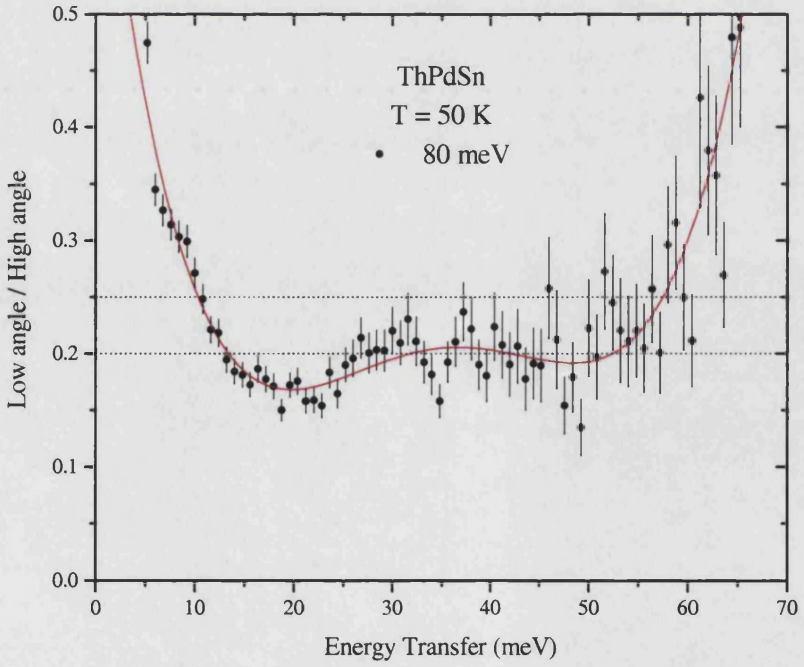

Figure 6.5 The ratio of the low angle to high angle scattering from ThPdSn with E_i = 80 meV. The line is the polynomial fit used to estimate the phonon contribution from the UPdSn data.

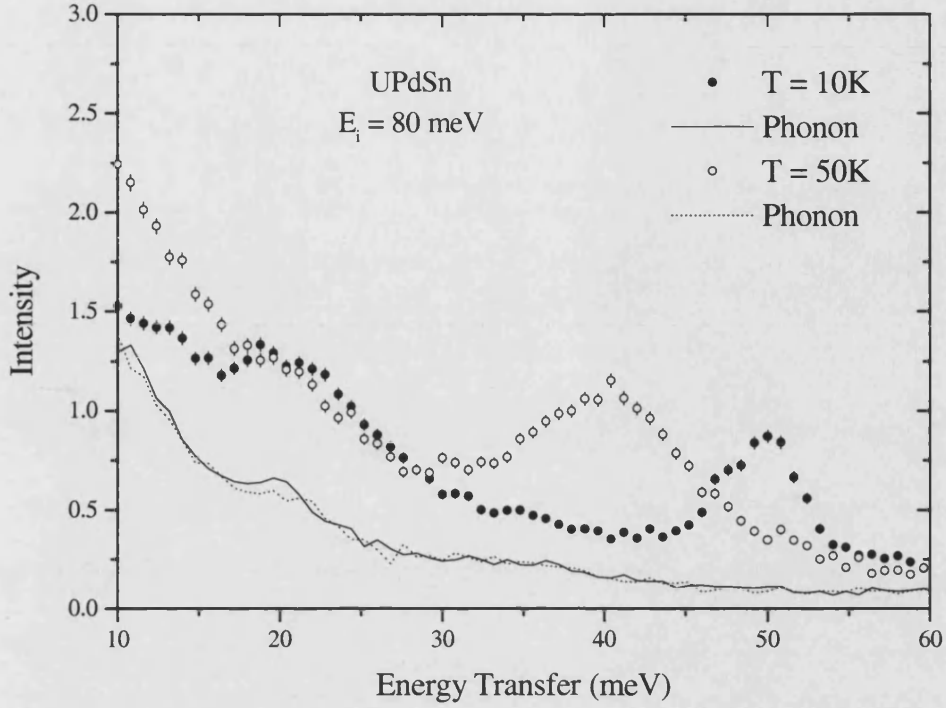

Figure 6.6 The total scattering from UPdSn at 10 and 50 K using neutrons with an incident energy of 80 meV. Note that the phonon scattering has been estimated by the ratio method

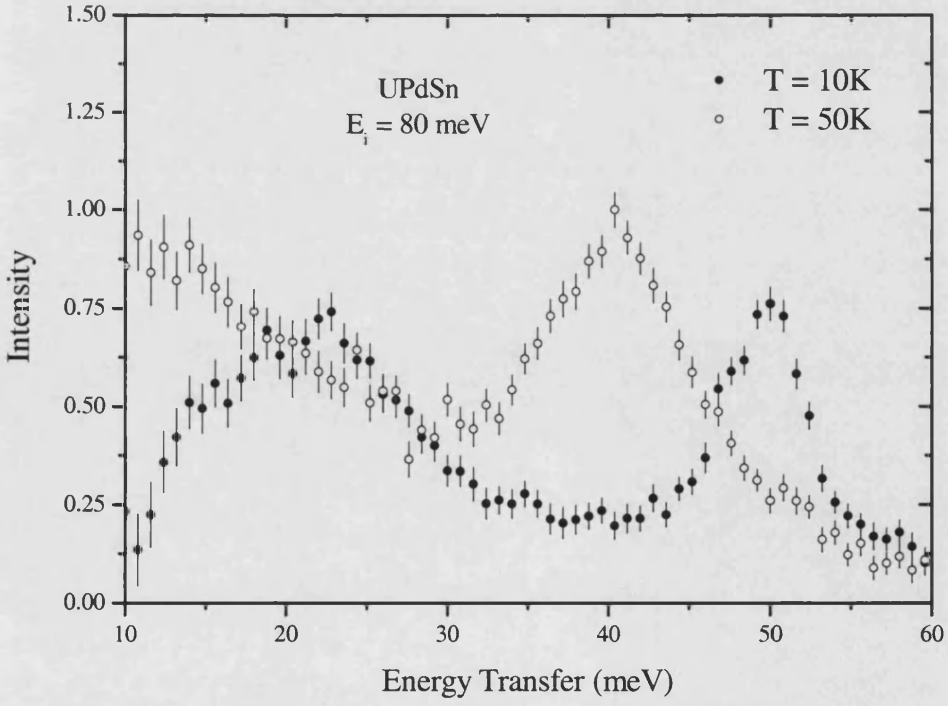

Figure 6.7 The magnetic scattering from UPdSn at 10 and 50 K using neutrons with an incident energy of 80 meV, obtained by subtracting the phonon contribution from the total scattering.

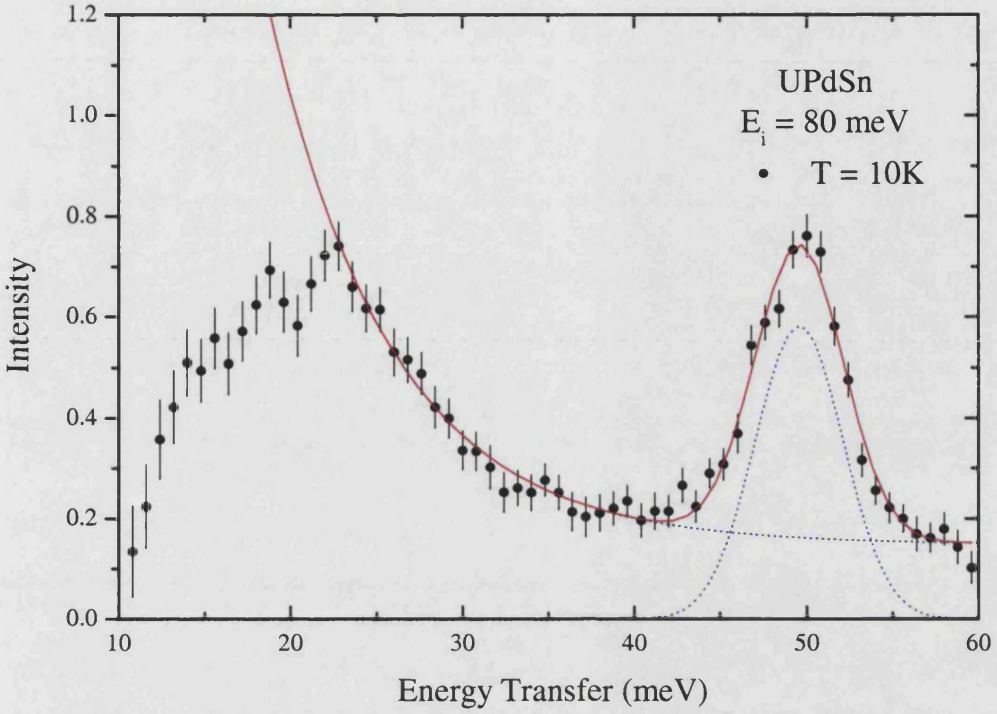

Figure 6.8 The magnetic scattering of UPdSn at T=10 K fitted to a single Gaussian and an exponentially decreasing background.

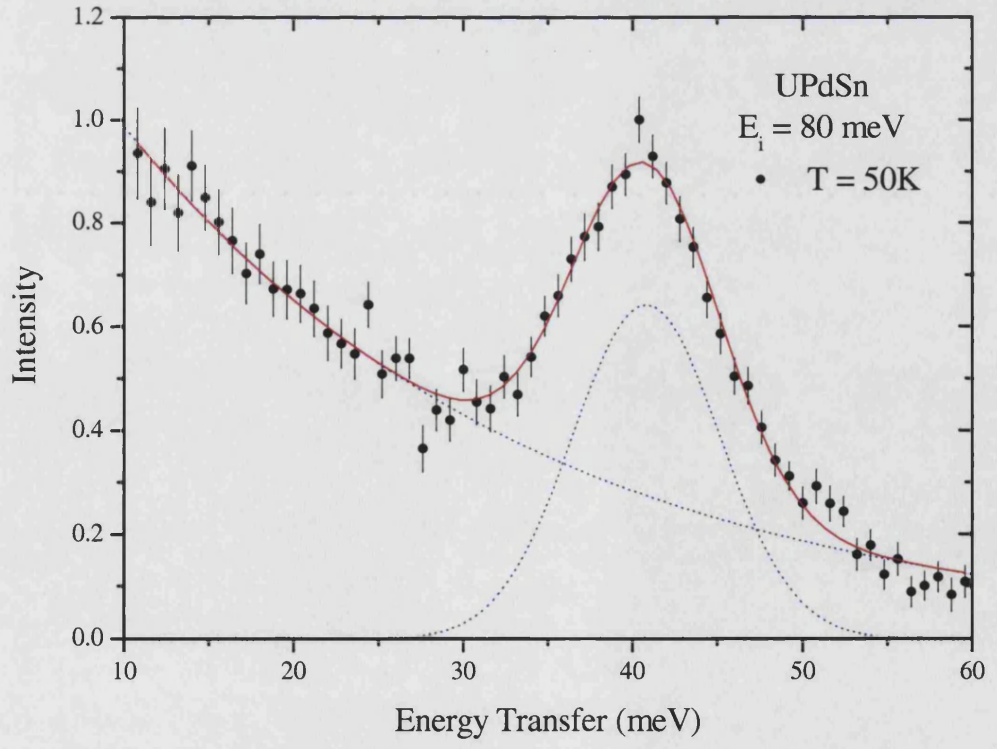

Figure 6.9 The magnetic scattering of UPdSn at T=50 K fitted to a single Gaussian and an exponentially decreasing background.

As can be seen in Figures 6.6 and 6.7, the peak shifts by a significant amount (~10 meV) on cooling from 50 to 10 K. Note that it is unlikely that the scattering at T = 10 K disappears at low energy transfers and that this effect is probably due to limitations in the ratio method subtraction around the elastic peak.

In order to determine the peak position and intensity, a single gaussian was fitted to the peak. Since the instrumental resolution is asymmetric, an exponential decay was used to approximate the background due to the elastic peak tail (see Figures 6.8 and 6.9 for an example of the fitting technique). The temperature dependence of the peak positions and intensities is shown in Figure 6.10.

On cooling from 100 to 10 K, the peak shifts from an energy transfer of 39 meV to an energy transfer of 50 meV with distinct changes around the two transition temperatures (shown by dotted lines). The integrated intensity decreases on cooling and this is due to the reduction of the peak width, not the peak height.

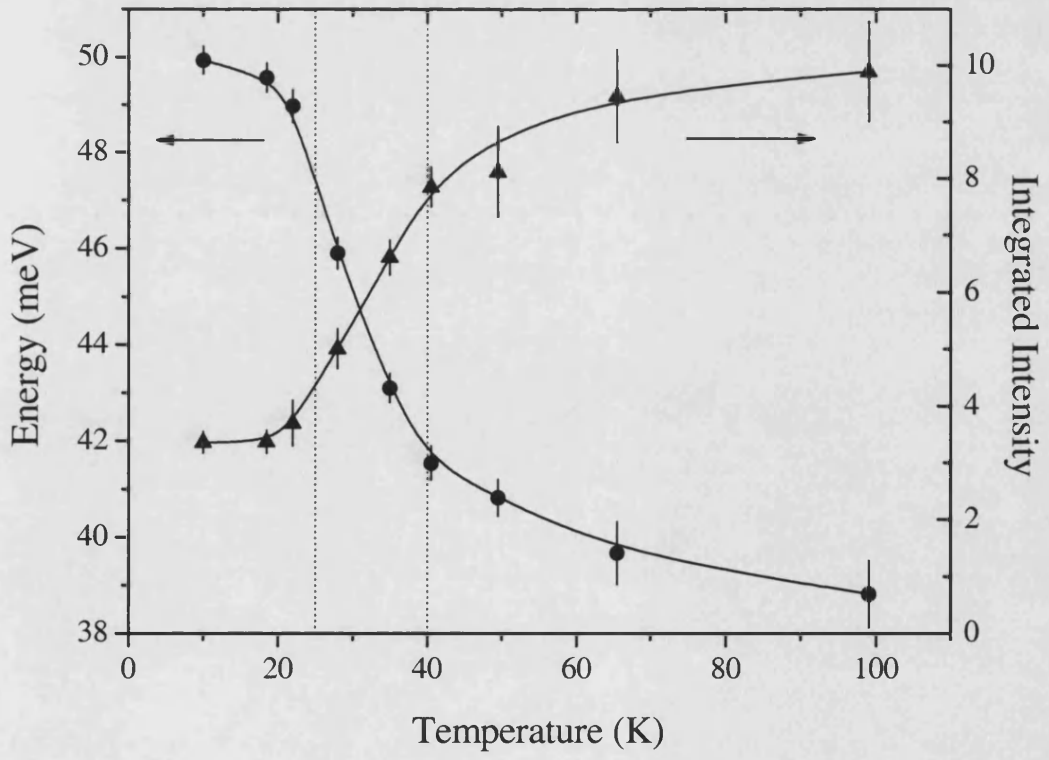

Figure 6.10 Temperature dependence of the energy transfer and integrated intensity of the 40-50 meV excitation. The transition temperatures of 25 and 40 K are shown by dotted lines.

The low energy magnetic scattering is shown in Figure 6.12 with distinct peaks visible at approximately 7 and 13 meV. This data, however, was obtained by scaling down the high angle data by a constant factor of 4. As can be seen in Figure 6.11, the ratio determined for an incident neutron energy of 36 meV varies considerably with energy transfer. Its value deviates significantly below 5 meV and above 25 meV, so only data within this range can be considered to be reliable. The ratio does not change with temperature so the average ratio was used for all of the temperature scans.

Using the ThPdSn data to obtain the phonon contribution via the ratio method results in the data shown in Figure 6.13. This method of analysis results in a broad band of magnetic scattering and a smearing out of the distinct features obtained by the previous method.

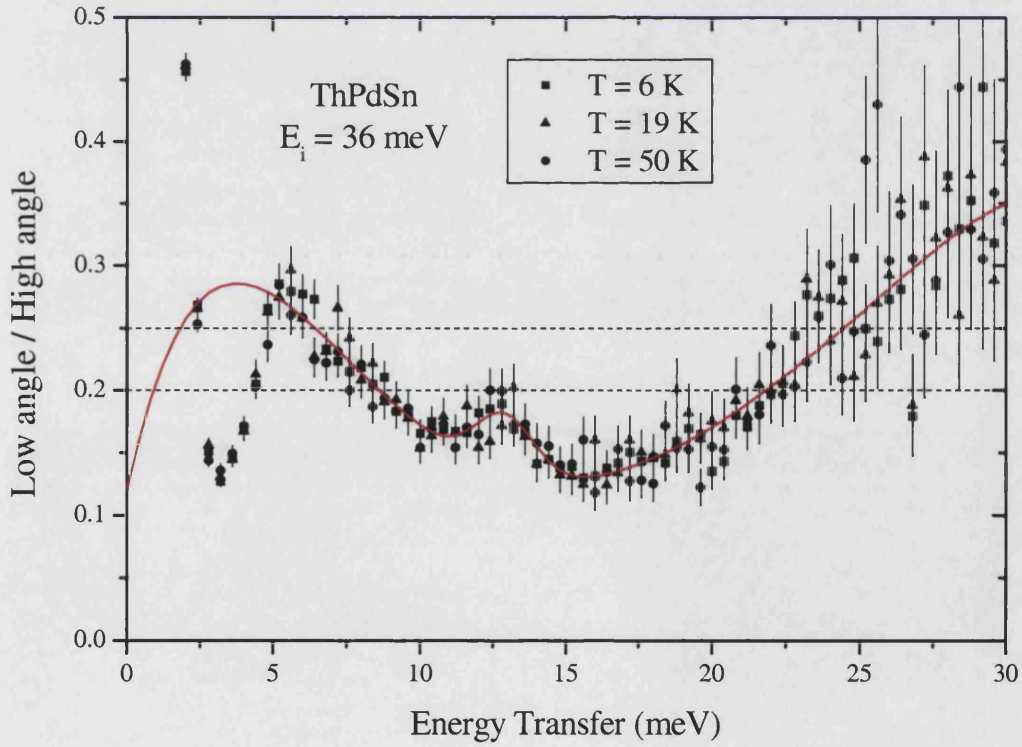

Figure 6.11 The ratio of low angle to high angle scattering from ThPdSn with E_i = 36 meV. The line is the polynomial plus gaussian fit used to estimate the phonon contribution .

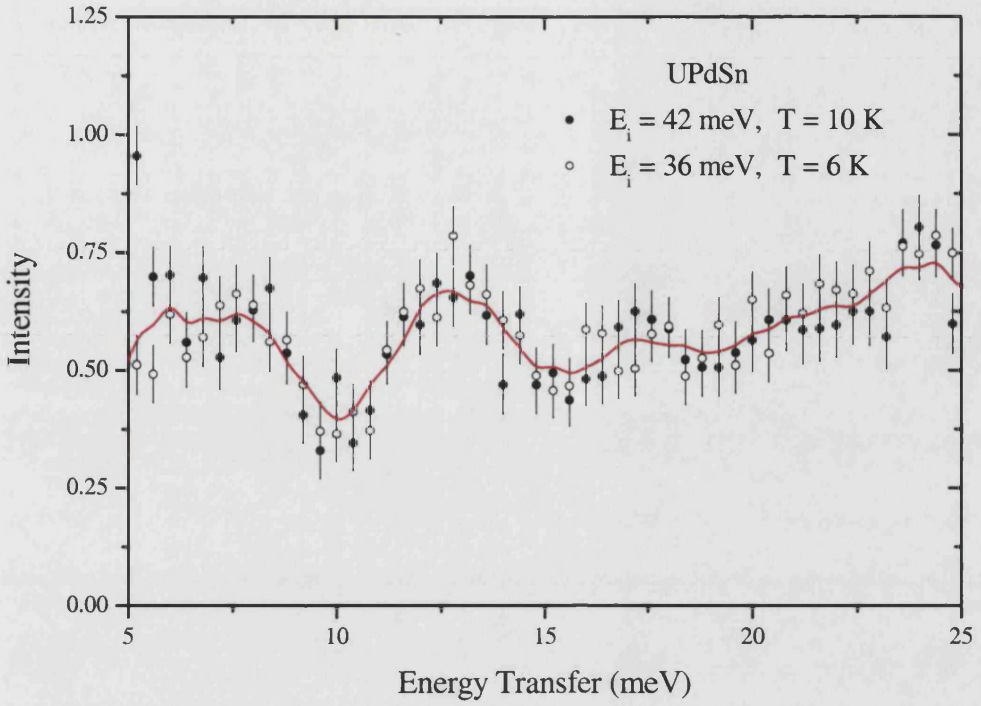

Figure 6.12 The low energy scattering from UPdSn obtained by subtracting the phonon contribution (calculated by scaling the high angle data by 0.25) from the total scattering.

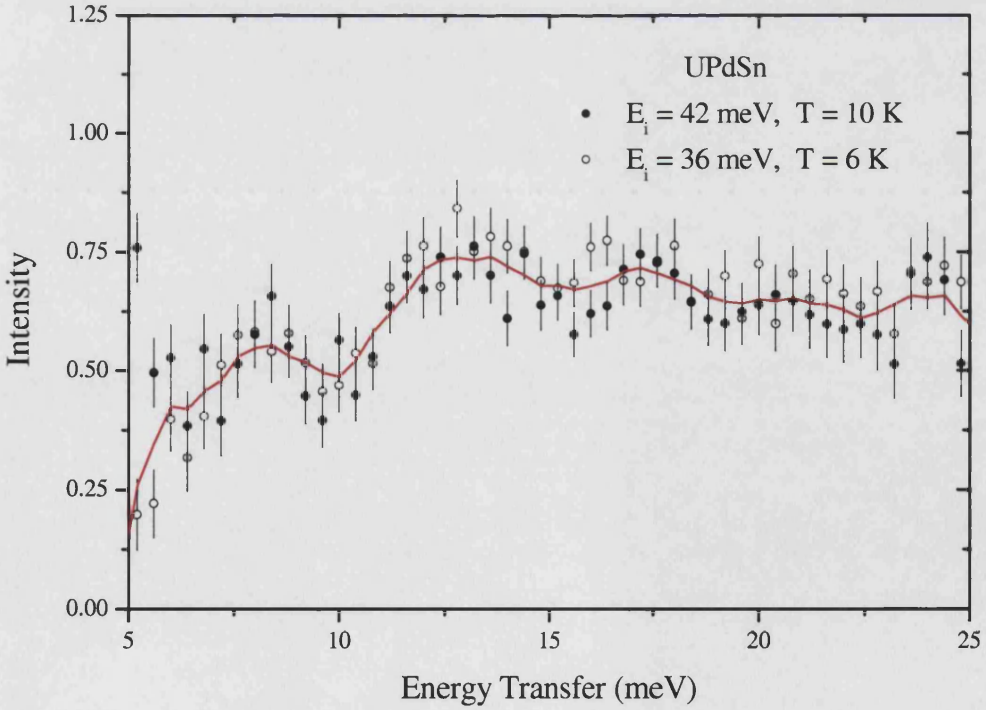

Figure 6.13 The low energy scattering from UPdSn obtained by subtracting the phonon contribution (calculated by the ratio method) from the total scattering.

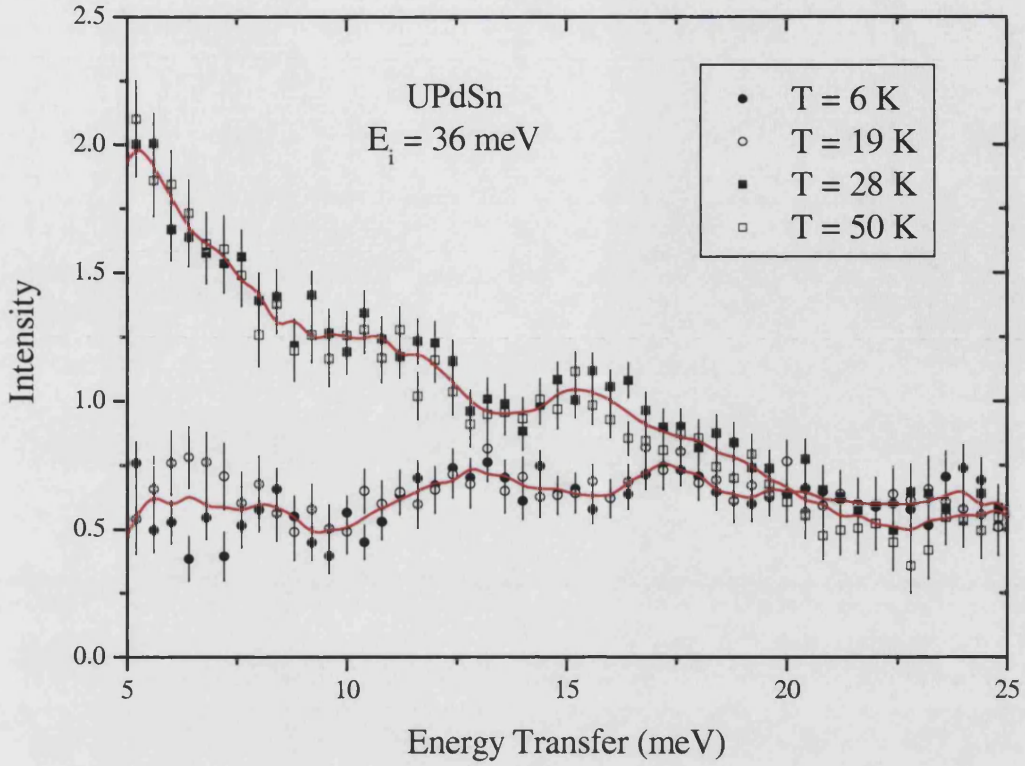

Figure 6.14 Temperature dependence of the low energy magnetic scattering from UPdSn obtained by subtracting the phonon contribution (calculated via the ratio method). The lines are the smoothed averages of the low and high temperature data.

The temperature dependence of the low energy magnetic scattering is shown in Figure 6.14. There is little difference between the scattering at 6 and 19 K, but raising the temperature above the lower transition temperature produces significant quasielastic scattering below 15 meV. On heating above the second transition temperature, there is again little change. This suggests that the low energy magnetic scattering is associated with the lower temperature transition.

Such a temperature dependence of the scattering could be envisaged as a change in the ground state doublet wavefunction at the 25 K transition. Above the transition temperature the J_z matrix element within the ground state may be large, producing significant quasielastic scattering. Below the transition, however, the ground state may split and the modified wavefunctions may not couple via J_z as intensely.

6.4 Calculations

6.4.1 Paramagnetic phase

The electronic configuration of UPdSn is $5f^2$ and, by applying Hund's rules, this gives $L = 5$, $S = 1$. Therefore $J = L - S = 4$ and there are $(2J + 1) = 9$ degenerate energy levels. The potential due to the hexagonal crystal symmetry splits the levels into three singlets and three doublets and, since UPdSn orders magnetically, the ground state must be one of these doublets.

The hexagonal symmetry means we have B_2^0, B_4^0, B_6^0 and B_6^6 contributions to the CEF Hamiltonian. Without the B_6^6 term there would be no mixing between the states and we would have a simple $|0\rangle, |\pm1\rangle, |\pm2\rangle, |\pm3\rangle, |\pm4\rangle$ level scheme. However, we find that the B_6^6 term results in the following scheme:

$$|0\rangle$$

$$1/\sqrt{2}|+3\rangle + 1/\sqrt{2}|-3\rangle$$

$$1/\sqrt{2}|+3\rangle - 1/\sqrt{2}|-3\rangle$$

$$|\pm1\rangle$$

$$\left.\begin{array}{l}\alpha|\pm4\rangle + \beta|\mp2\rangle \\ \beta|\pm4\rangle + \alpha|\mp2\rangle\end{array}\right\} \text{ where } \alpha^2 + \beta^2 = 1$$

If we assume that the $\alpha|\pm4\rangle + \beta|\mp2\rangle$ state is the ground state, $|g\rangle$, then it can be seen that $|\langle g|J_z|g\rangle| = 4\alpha^2 - 2\beta^2$. Now we know that:

$$C_z = \chi_z T = \frac{g^2\mu_B^2 N}{k_B}|\langle g|J_z|g\rangle|^2 = 2.39\,|\langle g|J_z|g\rangle|^2$$

where $N = 6.022 \times 10^{23}$ is the number of magnetic ions per mole.

Thus, by comparing this expression with the experimental heat capacity in the z-direction, we find that $|\langle g|J_z|g\rangle| = 2.06$, leading to the result:

$$\alpha = \pm 0.82 \quad \text{and} \quad \beta = \pm 0.57$$

Using $B_2^0 = \dfrac{5k(\theta_a - \theta_c)}{6(J+\frac{1}{2})(J+\frac{3}{2})} = 0.42$ meV, the result $B_6^6 = \pm\frac{77}{8}B_6^0$ and by choosing the following suitable values for B_4^0 and B_6^0:

$$B_2^0 = 0.4200\,\text{meV} \qquad B_6^0 = -0.0010\,\text{meV}$$

$$B_4^0 = -0.0345\,\text{meV} \qquad B_6^6 = 0.0100\,\text{meV}$$

we obtain the energy levels, wavefunctions and relative transition intensities from the ground state shown in Table 6.3. The transition intensity is calculated via:

$$\langle f|J_T|i\rangle^2 = \tfrac{2}{3}\left[\langle f|J_z|i\rangle^2 + \langle f|J_x|i\rangle^2 + \langle f|J_y|i\rangle^2\right]$$

Level (meV)	Wavefunction	Degeneracy	Transition Intensity	Operator
0.00	$0.820\|\pm 4\rangle - 0.573\|\mp 2\rangle$	Doublet	4.127	J_z
8.54	$\|\pm 1\rangle$	Doublet	1.476	J_x, J_y
15.11	$\|0\rangle$	Singlet	0.000	-
40.57	$0.573\|\pm 4\rangle + 0.820\|\mp 2\rangle$	Doublet	7.936	J_z
78.20	$\frac{1}{\sqrt{2}}\|+3\rangle - \frac{1}{\sqrt{2}}\|-3\rangle$	Singlet	2.488	J_x, J_y
128.60	$\frac{1}{\sqrt{2}}\|+3\rangle + \frac{1}{\sqrt{2}}\|-3\rangle$	Singlet	0.004	J_x, J_y

Table 6.3 The energy levels, wavefunctions and transition intensities in the paramagnetic phase obtained using the Stevens parameters discussed in the text.

Note that in the paramagnetic state at 50 K, only the ground state will be significantly populated (since k_BT = 4.31 meV) so there are no transitions between any of the other levels. From the calculations, we expect to see in the paramagnetic phase (i.e. T > 50 K) transitions from the ground state to the levels at energies of 8.5, 41 and 78 meV due to J_x and/or J_y coupling between them. In addition, we expect a significant amount of quasielastic scattering within the ground state itself.

If we look at the experimental data, the transition at 41 meV is clearly shown. However, there is no evidence for a peak at 78 meV although this could be due to the poor statistics of the HET data at high energy transfers. A further measurement using 130 meV incident neutrons would allow the presence of such a transition to be determined. In the paramagnetic phase, we indeed observe a large quasielastic response as predicted and this may have swamped the predicted level at 8.5 meV.

6.4.2 Ordered phase

From the Curie-Weiss theory, the effective internal field generated when ordering occurs is given by:

$$B_{eff} = \frac{J_{ex}}{ng^2\mu_B^2} ng\mu_B J = \frac{3k_BT_N}{g\mu_B(J+1)}$$

Thus the energy associated with the transition at T_N = 40 K can be estimated by an internal magnetic field of ~45 T. In an applied field of this magnitude, the energy levels and wavefunctions are changed significantly. The variation of the energy levels with applied field is shown in Figure 6.15.

Although the splitting between the ground state and the 40 meV level has increased in a field of 45 T, the observed splitting of 50 meV in the ordered phase is only reached in a field of 60 T. This suggests that the exchange interaction between the magnetic moments in UPdSn may be smaller than predicted by the Curie-Weiss model.

Applied field	0 T	60 T		
Direction of field	-	along z	along x	along y
Energy Level (meV)	0	0	0	0
	0	10.90	0.38	1.16
	8.54	12.69	5.97	6.18
	8.54	18.25	11.06	11.45
	15.11	22.04	23.05	23.40
	40.57	48.88	42.95	43.22
	40.57	49.09	43.23	43.65
	78.20	83.79	80.85	81.20
	128.60	136.88	131.14	131.48

Table 6.4 Summary of the energy levels, wavefunctions and transition intensities in the paramagnetic and ordered phases obtained using the Stevens parameters discussed in the text.

Table 6.4 lists the energy levels in zero field and in a field of 60 T applied along the three principal axes. In zero field (which corresponds to the paramagnetic state), there is an energy level at around 40 meV above the ground state which agrees with the neutron data at 50 K.

In an applied field of 60 T (which corresponds to the ordered state), the nine-fold degeneracy is completely lifted. With the field along the z-direction there are states at around 49 meV, and with the field along the x- and y-directions there are states around 6 and 11 meV (as shown in Figure 6.15). Both of these results seem to agree well with the intensities of the neutron data at $T = 6$ and 10 K .

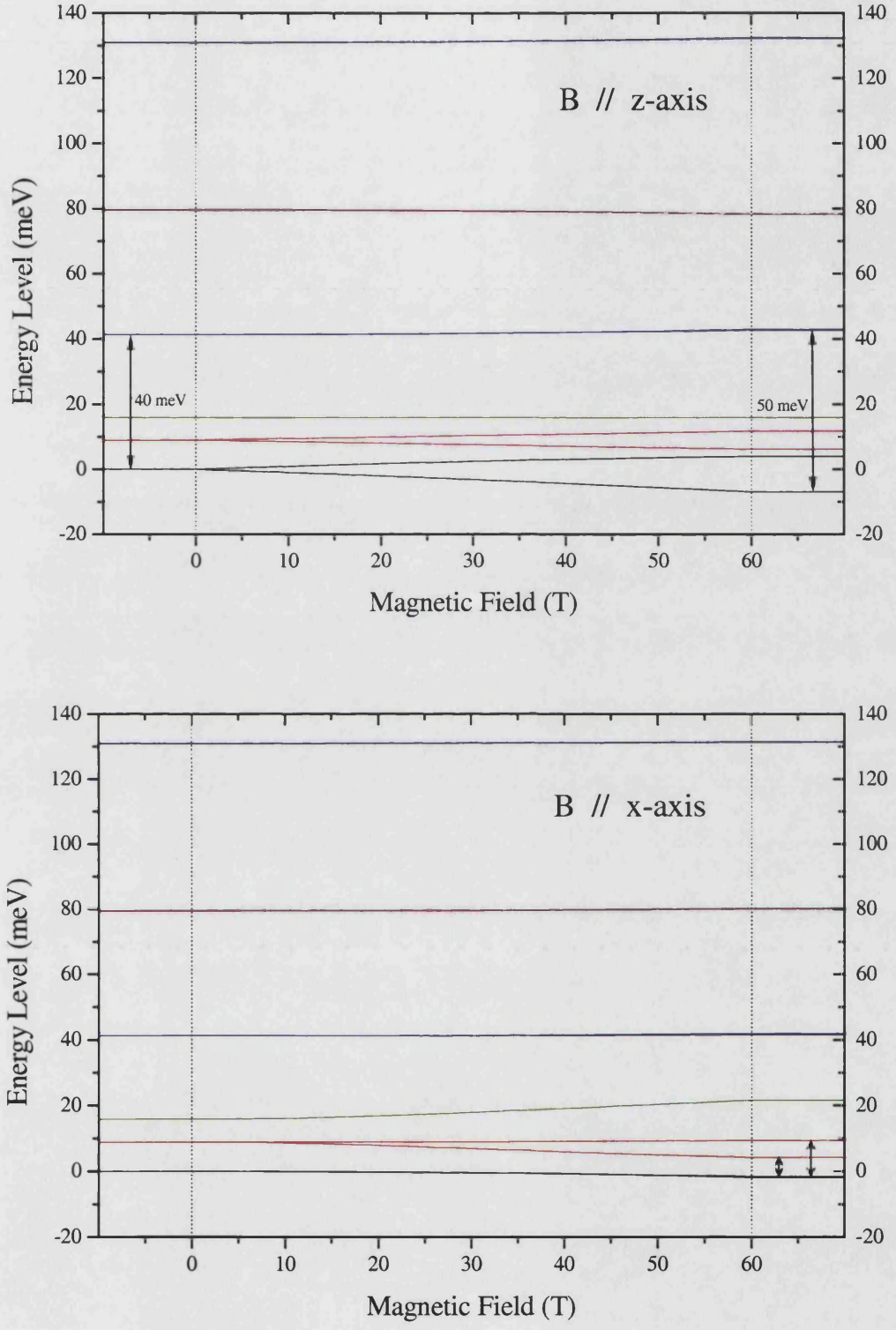

Figure 6.15 The change of energy levels in UPdSn as the internal magnetic field is increased from 0 to 60 T in the (top) *z*-direction and (bottom) *x*-direction. Note that for clarity, the levels below and above the two dotted lines are those in a constant field of 0 T and 60 T, respectively. The possible transitions observed in the neutron data are shown by arrows.

$B = 0$ T		Eigenvectors								
		$\|-4\rangle$	$\|-3\rangle$	$\|-2\rangle$	$\|-1\rangle$	$\|0\rangle$	$\|+1\rangle$	$\|+2\rangle$	$\|+3\rangle$	$\|+4\rangle$
Eigenvalues (meV)	0.00	0	0	-0.573	0	0	0	0	0	0.820
	0.00	0.820	0	0	0	0	0	-0.573	0	0
	8.54	0	0	0	0	0	1.000	0	0	0
	8.54	0	0	0	1.000	0	0	0	0	0
	15.11	0	0	0	0	1.000	0	0	0	0
	40.57	0	0	0.820	0	0	0	0	0	0.573
	40.57	0.573	0	0	0	0	0	0.820	0	0
	78.20	0	-0.707	0	0	0	0	0	0.707	0
	128.60	0	0.707	0	0	0	0	0	0.707	0

J_z intensity		Final State (meV)								
		0.00	0.00	8.54	8.54	15.11	40.57	40.57	78.20	128.60
Initial State (meV)	0.00	4.127	0	0	0	0	7.936	0	0	0
	0.00	0	4.127	0	0	0	0	7.936	0	0
	8.54	0	0	1.000	0	0	0	0	0	0
	8.54	0	0	0	1.000	0	0	0	0	0
	15.11	0	0	0	0	0	0	0	0	0
	40.57	7.936	0	0	0	0	0.001	0	0	0
	40.57	0	7.936	0	0	0	0	0.001	0	0
	78.20	0	0	0	0	0	0	0	0	9.000
	128.60	0	0	0	0	0	0	0	9.000	0

$J_{x,y}$ intensity		Final State (meV)								
		0.00	0.00	8.54	8.54	15.11	40.57	40.57	78.20	128.60
Initial State (meV)	0.00	0	0	0	1.476	0	0	0	2.488	0.004
	0.00	0	0	1.476	0	0	0	0	2.488	0.004
	8.54	0	1.476	0	0	5.000	0	3.024	0	0
	8.54	1.476	0	0	0	5.000	3.024	0	0	0
	15.11	0	0	5.000	5.000	0	0	0	0	0
	40.57	0	0	0	3.024	0	0	0	0.262	2.746
	40.57	0	0	3.024	0	0	0	0	0.262	2.746
	78.20	2.488	2.488	0	0	0	0.262	0.262	0	0
	128.60	0.004	0.004	0	0	0	2.746	2.746	0	0

Table 6.5 Calculated eigenvalues, eigenvectors and J_z and $J_{x,y}$ transition intensities in zero field.

B_z = 60 T		Eigenvectors								
		$\|-4\rangle$	$\|-3\rangle$	$\|-2\rangle$	$\|-1\rangle$	$\|0\rangle$	$\|+1\rangle$	$\|+2\rangle$	$\|+3\rangle$	$\|+4\rangle$
Eigenvalues (meV)	0.00	0	0	-0.432	0	0	0	0	0	0.902
	10.90	-0.681	0	0	0	0	0	0.732	0	0
	12.69	0	0	0	0	0	1.000	0	0	0
	18.25	0	0	0	1.000	0	0	0	0	0
	22.04	0	0	0	0	1.000	0	0	0	0
	48.88	0	0	0.902	0	0	0	0	0	0.432
	49.09	0.732	0	0	0	0	0	0.681	0	0
	83.79	0	-0.586	0	0	0	0	0	0.811	0
	136.88	0	0.811	0	0	0	0	0	0.586	0

J_z intensity		Final State (meV)								
		0.00	10.90	12.69	18.25	22.04	48.88	49.09	83.79	136.88
Initial State (meV)	0.00	8.291	0	0	0	0	5.468	0	0	0
	10.90	0	0.618	0	0	0	0	8.954	0	0
	12.69	0	0	1.000	0	0	0	0	0	0
	18.25	0	0	0	1.000	0	0	0	0	0
	22.04	0	0	0	0	0	0	0	0	0
	48.88	5.468	0	0	0	0	0.773	0	0	0
	49.09	0	8.954	0	0	0	0	1.473	0	0
	83.79	0	0	0	0	0	0	0	0.888	8.112
	136.88	0	0	0	0	0	0	0	8.112	0.888

$J_{x,y}$ intensity		Final State (meV)								
		0.00	10.90	12.69	18.25	22.04	48.88	49.09	83.79	136.88
Initial State (meV)	0.00	0	0	0	0.840	0	0	0	2.272	0.008
	10.90	0	0	2.410	0	0	0	0	2.803	0
	12.69	0	2.410	0	0	5.000	0	2.090	0	0
	18.25	0.840	0	0	0	5.000	3.660	0	0	0
	22.04	0	0	5.000	5.000	0	0	0	0	0
	48.88	0	0.000	0	3.660	0	0	0	0.243	2.977
	49.09	0	0	2.090	0	0	0	0	0.183	2.514
	83.79	2.272	2.803	0	0	0	0.243	0.183	0	0
	136.88	0.008	0	0	0	0	2.977	2.514	0	0

Table 6.6 Calculated eigenvalues, eigenvectors and J_z and $J_{x,y}$ transition intensities in a field of 60 T applied along the z-axis.

B_x = 60 T		Eigenvectors								
		$\|-4\rangle$	$\|-3\rangle$	$\|-2\rangle$	$\|-1\rangle$	$\|0\rangle$	$\|+1\rangle$	$\|+2\rangle$	$\|+3\rangle$	$\|+4\rangle$
Eigenvalues (meV)	0.00	0.455	-0.001	-0.367	-0.355	-0.257	-0.355	-0.367	-0.001	0.455
	0.38	0.528	0.052	0.405	0.234	0	-0.234	-0.405	-0.052	-0.528
	5.97	0.359	0.004	-0.176	0.459	0.509	0.459	-0.176	0.004	0.359
	11.06	-0.249	-0.018	-0.053	0.659	0	-0.659	0.053	0.018	0.249
	23.05	-0.107	-0.006	-0.044	-0.388	0.82	-0.388	-0.044	-0.006	-0.107
	42.95	0.390	0.052	0.575	-0.115	0.056	-0.115	0.575	0.052	0.390
	43.23	0.398	-0.038	-0.574	0.104	0	-0.104	0.574	0.038	-0.398
	80.85	-0.024	0.704	-0.063	0.005	0	-0.005	0.063	-0.704	0.024
	131.14	-0.031	0.705	-0.042	0.002	0	0.002	-0.042	0.705	-0.031

J_z intensity		Final State (meV)								
		0.00	0.38	5.97	11.06	23.05	42.95	43.23	80.85	131.14
Initial State (meV)	0.00	0	1.348	0	1.683	0	0	4.910	0	0
	0.38	1.348	0	2.095	0	0.500	6.451	0	0	0.001
	5.97	0	2.095	0	0.006	0	0	2.697	0	0
	11.06	1.683	0	0.006	0	0.083	1.116	0	0	0
	23.05	0	0.500	0	0.083	0	0	0.101	0	0
	42.95	0	6.451	0	1.116	0	0	0.013	0	0
	43.23	4.910	0	2.697	0	0.101	0.013	0	0	0.027
	80.85	0	0	0	0	0	0	0	0	8.968
	131.14	0	0.001	0	0	0	0	0.027	8.968	0

$J_{x,y}$ intensity		Final State (meV)								
		0.00	0.38	5.97	11.06	23.05	42.95	43.23	80.85	131.14
Initial State (meV)	0.00	3.680	0.426	3.179	0.158	0.033	0.421	1.010	3.151	0.000
	0.38	0.426	1.247	1.977	0.957	0.058	0.430	0.313	4.196	0.001
	5.97	3.179	1.977	1.972	3.687	0.996	1.183	0.527	1.651	0.029
	11.06	0.158	0.957	3.687	0.068	6.909	2.142	2.483	0.650	0.058
	23.05	0.033	0.058	0.996	6.909	7.251	2.215	1.741	0.048	0.064
	42.95	0.421	0.430	1.183	2.142	2.215	0.081	0.033	0.587	5.327
	43.23	1.010	0.313	0.527	2.483	1.741	0.033	0.182	0.561	5.401
	80.85	3.151	4.196	1.651	0.650	0.048	0.587	0.561	0.184	0.005
	131.14	0.000	0.001	0.029	0.058	0.064	5.327	5.401	0.005	0.119

Table 6.7 Calculated eigenvalues, eigenvectors and J_z and $J_{x,y}$ transition intensities in a field of 60 T applied along the x-axis.

6.5 Conclusions

Inelastic neutron scattering has been performed on a polycrystalline sample of UPdSn. A well defined excitation likely to be due to a transition between crystalline electric field levels has been observed at around 40 meV in the paramagnetic phase. The temperature dependence of this excitation has been followed down to $T = 10$ K.

The peak shifts upwards in energy as the temperature decreases, reaching an energy of around 50 meV at the lowest temperature measured. The temperature dependence is smooth, but has noticeable changes in gradient at the two transition temperatures of $T_N = 25$ and 40 K. Such a smooth variation is not expected for first order magnetic ordering transitions. However, the μSR data of Noakes *et al.*, which suggests that the two transitions are second order, may help to explain this.

By comparison of the experimental specific heat with that expected from calculations on a set of CEF energy levels, values for the Stevens parameters have been deduced. These parameters predict energy levels in the paramagnetic phase which are consistent with the excitations we have observed in this experiment.

The effect of magnetic ordering on the energy levels and associated wavevectors has been estimated by assuming a mean field interaction acts below the transition temperature. Thus, the energy levels and wavefunctions in the ordered phase have been obtained and a comparison made with experiment. The calculated energy levels in the ordered phase are consistent with our $T = 6$ and 10 K data when the mean field reaches approximately 60 T. This value of the field is, however, larger than the value predicted by the Curie-Weiss mean field theory, and may point towards a reduced interaction between the *f* electrons.

The observation of crystal field levels and the agreement between experiment and calculations based on a CEF level scheme are strong evidence that the 5*f* electrons in UPdSn are well localised, which is rare in uranium intermetallic compounds.

6.6 References

[1] Palstra *et al.*, J. Mag. Mag. Mat. **67** (1987) 331

[2] Robinson *et al.*, J. Mag. Mag. Mat. **98** (1991) 147

[3] de Boer *et al.*, Physica B **176** (1992) 275

[4] Nakotte *et al.*, Phys. Rev. B **47, 2** (1993) 831

[5] Nakotte *et al.*, Phys. Rev. B **58, 14** (1998) 9269

[6] Noakes *et al.*, Physica B **312-313** (2002) 292

CHAPTER 7

UCu_2Sn

7.1 Literature Review

The first experiments on UCu_2Sn were performed by Takabatake *et al.*[1] They found that the compound crystallises in the $ZrPt_2Al$-type structure (space group $P6_3/mmc$) in which the constituent atoms are stacked in layers perpendicular to the hexagonal c-axis with a sequence ...U, Cu, Sn, Cu... (Figure 7.1). The room temperature lattice parameters have been determined as $a = 4.46$ Å and $c = 8.71$ Å which gives atom separations of $d_{U\text{-}U} = 4.46$ Å, $d_{U\text{-}Sn} = 3.37$ Å and $d_{U\text{-}Cu} = 2.87$ Å. Such a uranium-uranium separation is well above the Hill limit. Hybridisation is therefore expected between localised $5f$ electrons and delocalised ligand electrons, although a direct overlap of $5f$ wavefunctions is unlikely in the U layer.

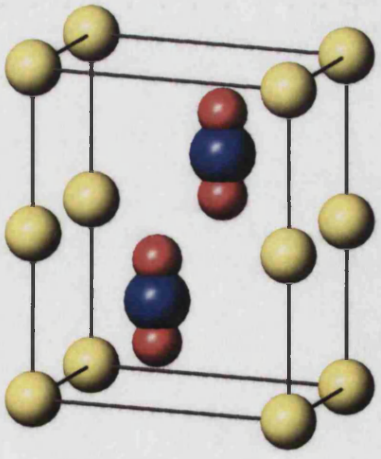

Figure 7.1 Diagram of the hexagonal unit cell for UCu_2Sn in which the atoms are stacked in layers of Sn (yellow), Cu (red), U (blue), Cu (red) along the c-axis.

The magnetic, transport and thermal properties of UCu_2Sn have been reported for both polycrystalline[1] and single crystal[2] samples. The resistivity is temperature independent above 100 K, but increases sharply upon cooling below 16.5 K. In contrast to the drop in resistivity in the polycrystalline sample upon further cooling, the resistivity saturates along the *a* and *c* axes whilst increasing along the *b* axis. This may point to a contaminated phase in the polycrystalline sample.

Above 150 K, the magnetic susceptibility displays Curie-Weiss behaviour with an effective magnetic moment of $\mu_{eff} = (3.3 \pm 0.3)\mu_B/\mathrm{U}$ and a paramagnetic Curie temperature of θ_p = -(89 ± 30) K. At low temperatures, a pronounced peak in the magnetic susceptibility occurs at around 16.5 K. High field magnetisation measurements show a spin-flop-like behaviour at B = 23.5 T at a temperature of 4.2 K. The specific heat exhibits a sharp λ-type anomaly at 16.5 K which releases a magnetic entropy of $R\ln 2$ (Figure 7.2). This means that there are at least two levels below an energy scale of ~1.5 meV and suggests that the paramagnetic ground state is a doublet. The electronic specific heat coefficient was determined to be γ = 60 $\mathrm{mJ/K^2molU}$ from the low temperature behaviour.

These bulk measurements strongly suggest that the anomaly at 16.5 K is due to antiferromagnetic ordering. However, recent Mössbauer[3], NMR[4], μSR[5] and neutron diffraction[2] experiments have all been unable to detect any sign of antiferromagnetic ordering.

Further nuclear quadrupolar resonance (NQR) experiments[6] have suggested that the ordered state might be due to a non-magnetic phase transition, such as quadrupolar ordering. This type of ordering involves an alignment of the charge densities of the ions and is therefore strongly coupled to the lattice. Hence, fluctuations in the quadrupolar ordering affect the lattice and give rise to anomalies in the elastic constant measurements. Such measurements in UCu_2Sn have revealed a dramatic softening of the c_{66} transverse elastic modulus around 16.5 K with more than a 57% reduction in the stiffness[7].

Such a large softening of the lattice cannot be explained to arise solely from an antiferromagnetic transition, and it has been proposed that a quadrupolar ordering of the non-Kramers ground state doublet Γ_5 occurs at T_Q = 16.5 K in this compound. However, x-ray diffraction studies of UCu_2Sn have revealed neither a broadening of diffraction peaks indicative of ferroquadrupolar (FQ) ordering nor superlattice reflections indicative of antiferroquadrupolar (AFQ) ordering.

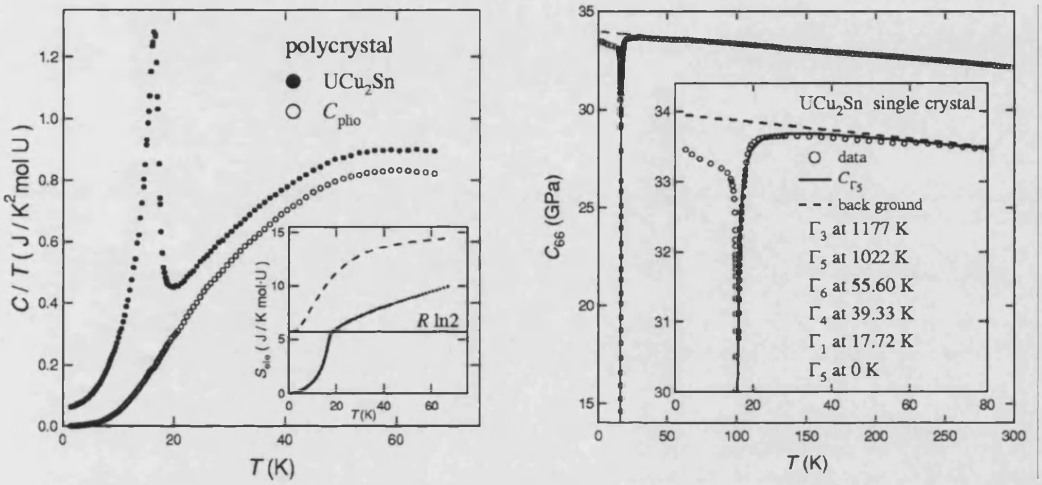

Figure 7.2 (a) Specific heat data showing the λ-type transition at T_Q. Inset: the magnetic entropy. (b) Elastic constant measurements showing a softening at T_Q. Inset: the calculated level scheme.

Suzuki *et al.* have interpreted their results in terms of a crystal field scheme and a $5f^2$ configuration. In their crystalline electric field (CEF_1) model, the ground state is Γ_5 with excited states at 1.52, 3.38, 4.79, 88.1 and 101 meV. All of these states, except that at 1.5 meV, are dipolar coupled to the ground state. The CEF_1 level scheme is shown in Figure 7.3.

Since our experiment on HET, Suzuki *et al.* have produced another set of Stevens parameters based on measurements of the specific heat, thermal expansion, susceptibility and elastic constants in a magnetic field. In the crystalline electric field (CEF_2) model deduced from these new parameters, the ground state is again Γ_5 but the excited states are now calculated to be at energies of 9.38, 28.61, 35.82, 50.39 and 75.91 meV. All of these states, except that at 35.82 meV, are dipolar coupled to the ground state. The CEF_2 level scheme is shown in Figure 7.4.

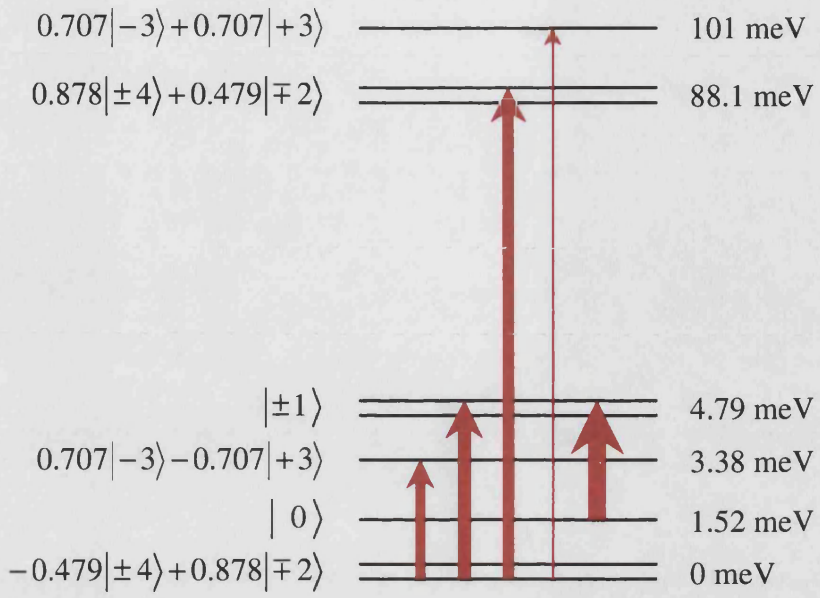

Figure 7.3 The first CEF level scheme deduced by Suzuki *et al.* from elastic constant measurements. Possible transitions for temperatures just above T_Q are indicated and the thickness of the line indicates their relative intensity.

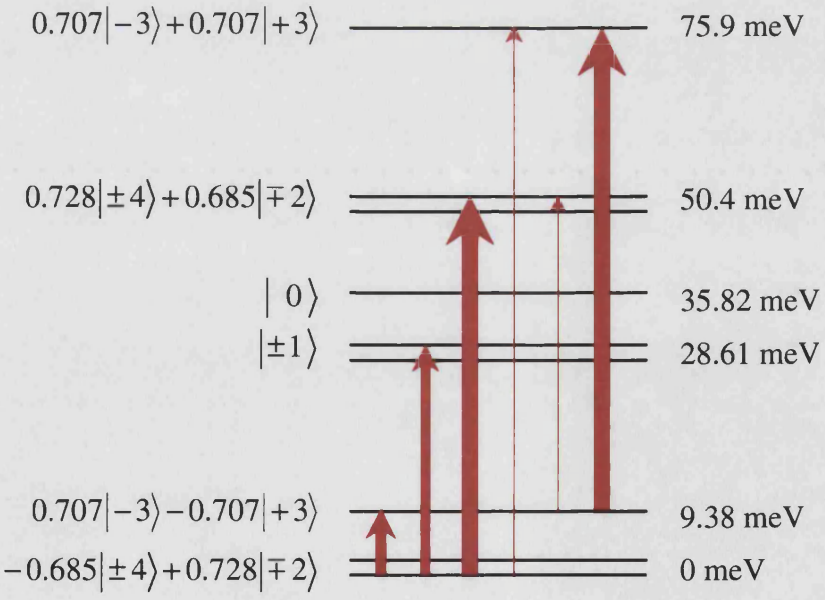

Figure 7.4 The second CEF level scheme deduced by Suzuki *et al.* from more recent bulk measurements. Possible transitions for temperatures well above T_Q are indicated and the thickness of the line indicates their relative intensity.

7.2 Experimental Procedure

Firstly, a white beam vanadium run was carried out for the subsequent normalisation process. The 17.97 g sample of UCu_2Sn was crushed and placed into an aluminium sachet which was then attached to the bottom of a closed-cycle refrigerator (CCR) and cooled. At 7 K, the scattering from UCu_2Sn was measured with incident neutron energies of 60 and 150 meV.

Measurements using neutrons with an incident energy of 23 meV were then made at various temperatures below and above T_Q. Finally, a measurement was made using high incident energy neutrons to search for intermultiplet transitions. See Table 7.1 for a complete list of the data collected.

Incident Energy (meV)	Chopper Speed (Hz)	Sample Temp (K)	Total μAhr
Vanadium	white beam	RT	114
23	150	7	1100
23	150	12	1100
23	150	16	1100
23	150	20	1100
23	150	100	1124
60	200	7	1115
150	250	7	1100
800	600	12	486
800	600	100	3037

Table 7.1 List of scans performed during the experiment.

7.3 Results and Discussion

The magnetic scattering obtained using E_i = 150 meV neutrons is shown in Figure 7.5. The scattering below 120 meV is essentially smooth, although there appears to be extra scattering around 45 meV and a shoulder of scattering at 25 meV. An investigation of these features was performed using E_i = 60 meV neutrons.

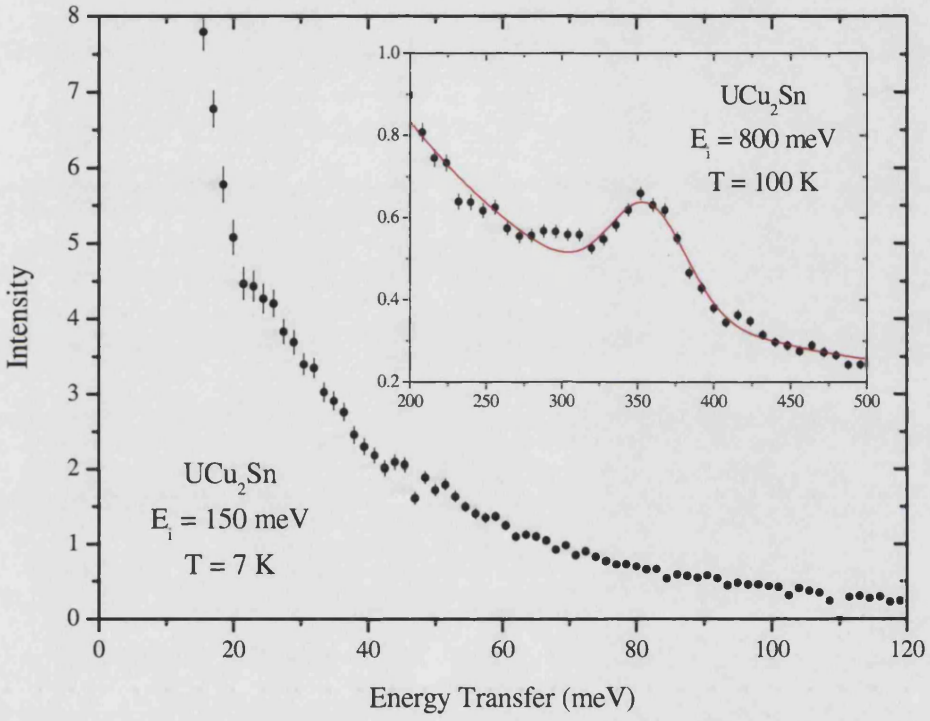

Figure 7.5 Magnetic scattering from UCu_2Sn using neutrons with an incident energy of 150 meV. Inset: possible intermultiplet transition observed using 800 meV incident energy neutrons.

The total scattering and phonon background are shown in the inset of Figure 7.6. Since a non-magnetic reference compound was not available, the phonon contribution was estimated by scaling down the high angle bank data by a factor of 4.5. Looking at the energy gain side, it appears that the phonons are slightly underestimated. The magnetic scattering, shown in the main part of this figure, is dominated by a peak of scattering centred at 7.5 meV which continues up to around 20 meV where a gradient change occurs. No features are seen at 45 meV.

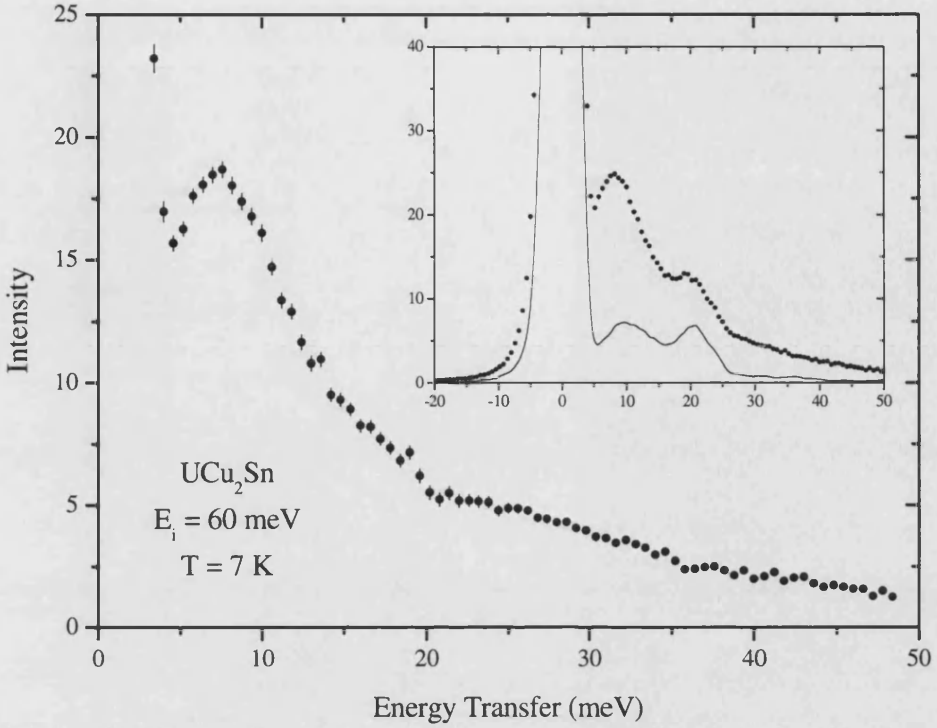

Figure 7.6 Magnetic scattering from UCu_2Sn using neutrons with an incident energy of 60 meV. Inset: the total scattering (points) and phonon contribution estimated by the scaling method (line).

Scans using 23 meV neutrons were then made at various temperatures above and below T_Q in order to investigate the temperature dependence of the scattering below 20 meV. The magnetic scattering from UCu_2Sn at T = 12 K with E_i = 23 meV is shown in Figure 7.7 for both the 2.5 m and 4 m banks.

In the 2.5 m bank, the magnetic scattering is seen as a broad, asymmetric peak centred around 7 meV. The width of the peak is approximately 6 meV, much greater than the instrumental resolution of 0.7 meV. A two gaussian fit places peaks at 6.55 and 8.25 meV with widths of 2.92 and 7.26 meV, respectively.

The data from the 4 m bank reveals at least two contributions to the broad peak which can be fitted to two Gaussian peaks centred at 3.72 and 8.21 meV, with widths of 1.23 and 7.01 meV, respectively. The 4 m bank data has also been fitted by two gaussians with their peak positions fixed to be those obtained from the fit to the 2.5 m data. A summary of the fit parameters is given in Table 7.2.

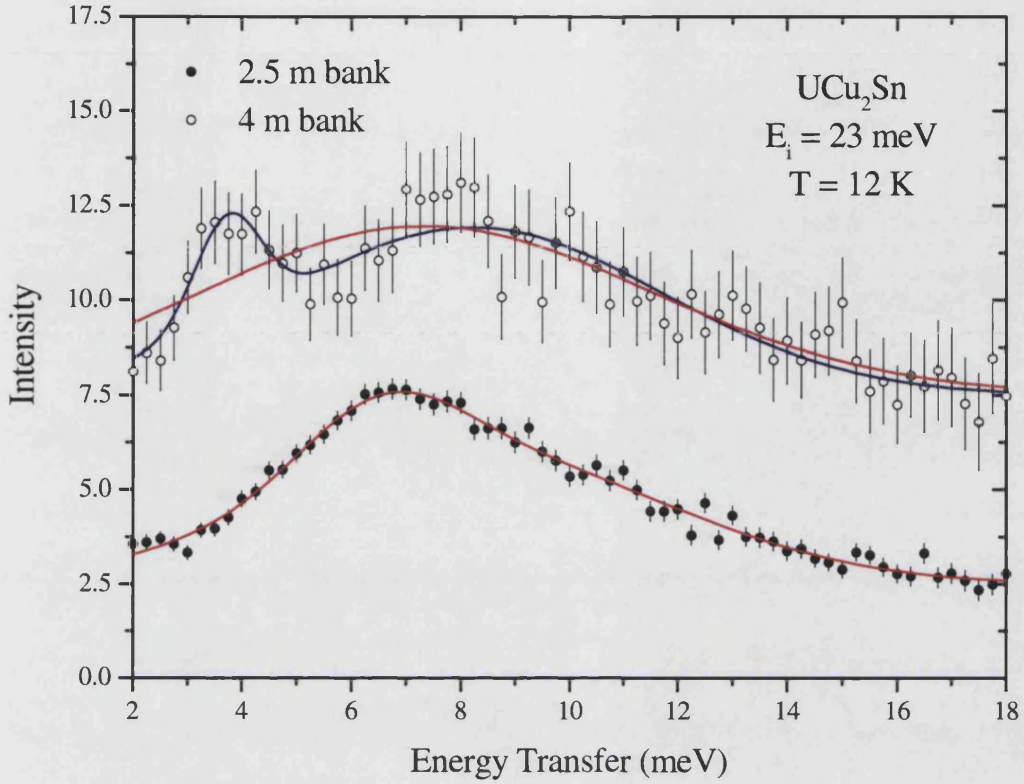

Figure 7.7 Magnetic scattering from UCu_2Sn at 12 K in the 2.5 and 4 m detector banks. The 4 m data has been offset by 5 units for clarity. The solid lines are fits to two gaussian peaks with the peak positions determined by the 2.5 m data. The blue line is a two gaussian fit to the 4 m data.

	2.5 m data	4 m data	
	Free positions	Free positions	Fixed positions
xc_1 (meV)	6.55 ± 0.11	3.72 ± 0.11	6.55 ± 0
w_1 (meV)	2.92 ± 0.31	1.23 ± 0.29	7.62 ± 2.49
A_1 (mb/sr/U)	7.23 ± 1.46	4.34 ± 1.27	20.9 ± 12.6
xc_2 (meV)	8.25 ± 0.17	8.21 ± 0.26	8.25 ± 0
w_2 (meV)	7.26 ± 0.22	7.01 ± 0.53	8.68 ± 1.70
A_2 (mb/sr/U)	31.0 ± 1.63	38.8 ± 2.54	25.8 ± 12.0

Table 7.2 Parameters obtained from the two gaussian fit to the 2.5 and 4 m data at T = 12 K.

The temperature dependence of the scattering is shown in Figure 7.8. There is little change between 7.5 and 12 K, but as the transition temperature is approached the scattering reduces significantly and a quasielastic component begins to form. By the time the temperature reaches 20 K, the scattering is flat and the quasielastic scattering reaches its maximum value. At 100 K, the shape of the scattering remains flat but the overall intensity is reduced.

Fits to the magnetic data have been made at each temperature using a combination of a linear term and either two or three gaussian peaks. The peak positions were fitted simultaneously between all of the data sets, but the widths and intensities were allowed to vary freely for each data set. An example of each fitting technique is shown in Figures 7.9 and 7.10 for the $T = 7.5$ K data.

The parameters obtained from these fits are shown in Tables 7.3 and 7.4. It can be seen that the data at $T = 20$ and 100 K could be fitted by a linear term only. The linear terms change smoothly between 7.5 and 20 K, becoming steeper and more intense as the temperature is raised. In contrast, the gaussian peaks decrease in intensity whilst their widths do not change significantly.

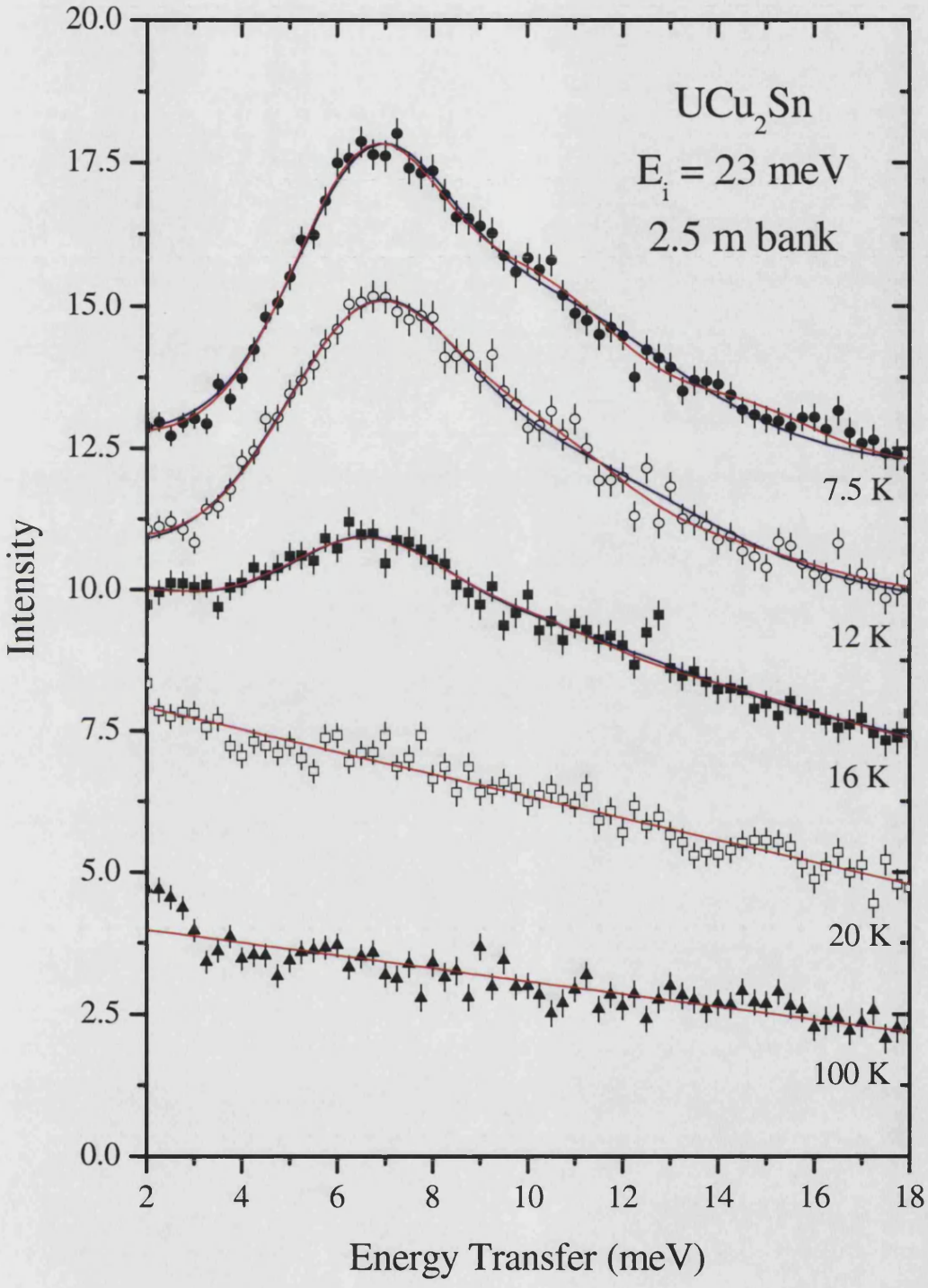

Figure 7.8 Magnetic scattering from UCu_2Sn at various temperatures, using an incident energy of 23 meV. Note that each temperature has been offset by 2.5 units for clarity. The fits are to two (blue line) and three (red line) gaussians on top of a linear background – the positions of the gaussians are the same for each fit but the widths and areas are allowed to vary.

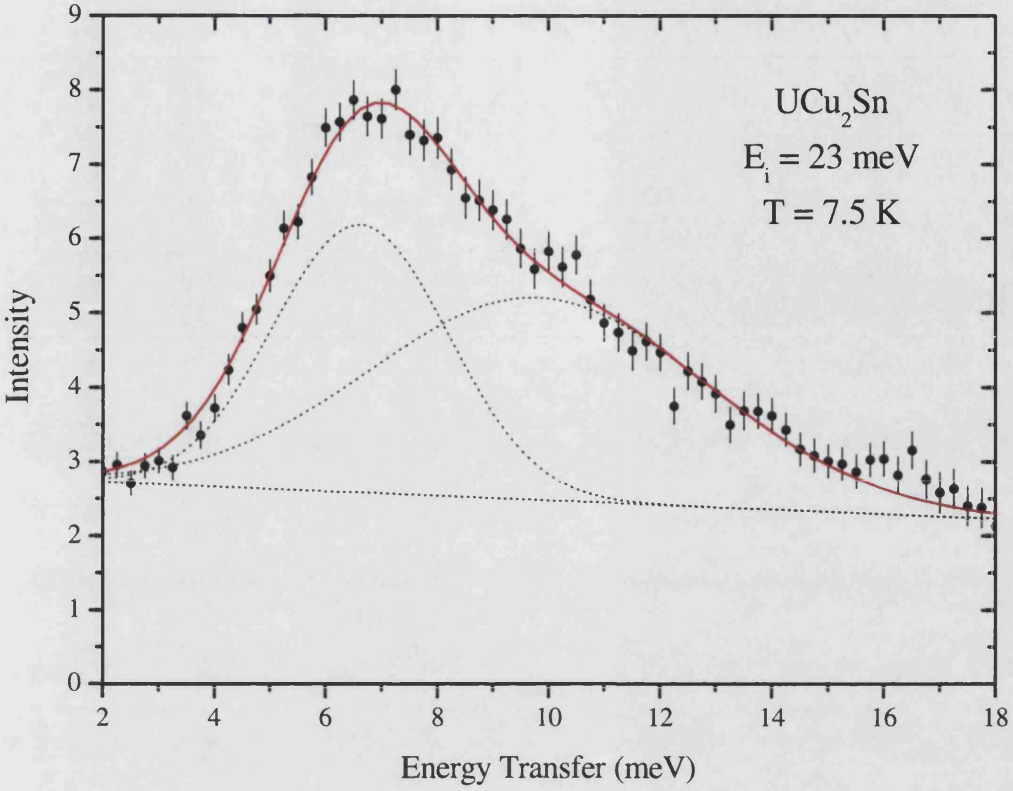

Figure 7.9 Example of the two gaussian fitting with a linear background term.

T (K)	7.5	12	16	20	100
m	-0.03 ± 0.01	-0.05 ± 0.01	-0.16 ± 0.01	-0.20 ± 0.01	-0.11 ± 0.01
c	2.79 ± 0.13	3.24 ± 0.24	5.33 ± 0.15	5.81 ± 0.07	4.21 ± 0.07
w_1 (meV)	3.13 ± 0.25	3.51 ± 0.24	3.08 ± 0.38	-	-
A_1 (mb/sr/U)	14.14 ± 3.21	13.94 ± 2.59	4.86 ± 1.02	-	-
w_2 (meV)	6.06 ± 0.25	6.79 ± 0.24	6.16 ± 0.38	-	-
A_2 (mb/sr/U)	20.64 ± 3.43	19.55 ± 4.77	5.97 ± 1.52	-	-

Table 7.3 Parameters obtained from the linear plus two gaussian fit to the 23 meV data. The peak positions were found to be (6.62 ± 0.05) and (9.81 ± 0.55) meV.

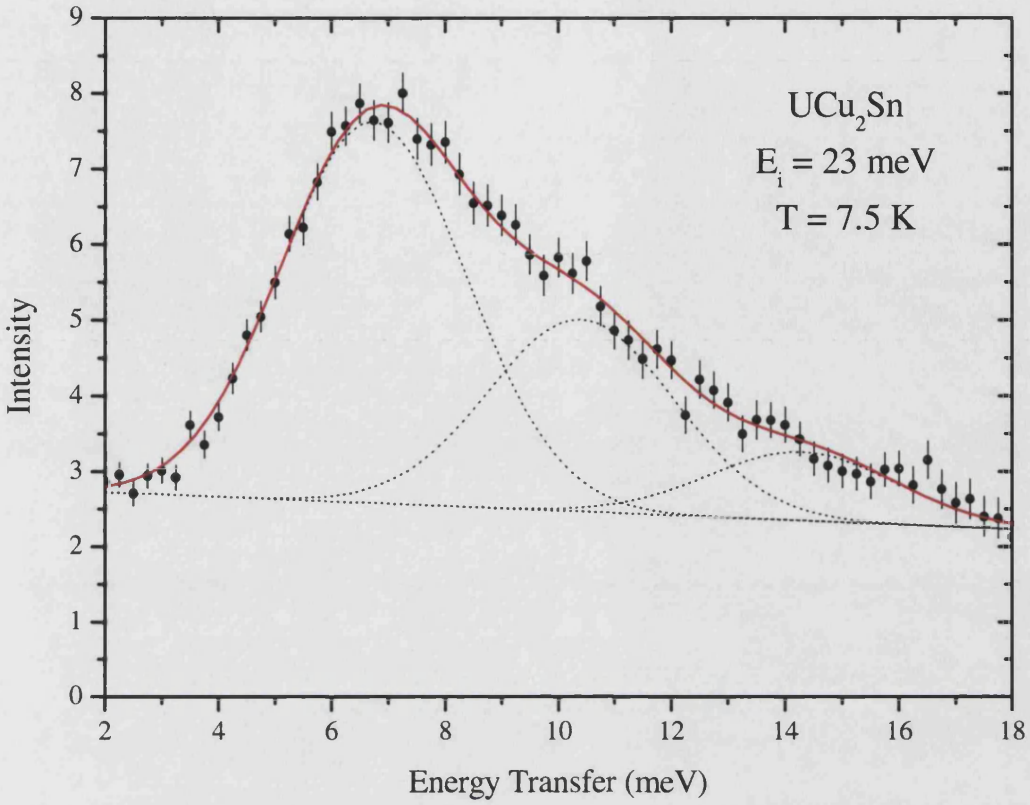

Figure 7.10 Example of the three gaussian fitting with a linear background term.

T (K)	7.5	12	16	20	100
m	-0.03 ± 0.01	-0.05 ± 0.01	-0.16 ± 0.01	-0.20 ± 0.01	-0.11 ± 0.01
c	2.79 ± 0.13	3.44 ± 0.16	5.32 ± 0.14	5.81 ± 0.07	4.21 ± 0.07
w (meV)	3.29 ± 0.09	3.61 ± 0.18	3.37 ± 0.36	-	-
A_1 (mb/sr/U)	20.76 ± 0.57	10.46 ± 0.40	3.74 ± 0.39	-	-
A_2 (mb/sr/U)	19.14± 1.11	8.94 ± 0.49	2.31 ± 0.63	-	-
A_3 (mb/sr/U)	6.89 ± 0.82	2.96 ± 0.40	1.09 ± 0.56	-	-

Table 7.4 Parameters obtained from the linear plus three gaussian fit to the 23 meV data. The peak positions were found to be (6.73 ± 0.05), (10.40 ± 0.14) and (14.30 ± 0.26) meV.

Our experimental results may be compared with the predictions of the CEF models of Suzuki *et al.* According to the first (CEF_1) model, in the paramagnetic phase we should expect neutron induced transitions at 3.4, 4.8, 88 and 101 meV from the ground state, and also transitions at 3.3 meV from the Γ_1 excited state at 1.5 meV (17.5 K) when this is thermally occupied. However, in our data for 16 K and 20 K, we see no distinct peaks between 2 and 15 meV.

According to the second (CEF_2) model, in the paramagnetic phase we should expect neutron induced transitions at 9.4, 28.6, 35.8, 50.4 and 75.9 meV from the ground state, and also transitions at 41.0 and 66.5 meV from the Γ_1 excited state at 1.5 meV (109 K) when this is thermally occupied. The level at 9.4 meV is consistent with our data, although we would expect the scattering from such a transition to be symmetric and less broad.

The wavefunctions and eigenvalues of the CEF levels will be modified in the ordered phase below T_Q = 16.5 K. In particular, the degeneracy of the proposed Γ_5 ground state doublet will be removed. The splitting will be of the order of $k_B T_Q$ (i.e. around 1.4 meV), so it is possible for there to be two or more excitations in the low energy spectra. However, the energy scale of the excitations we have found below T_Q is almost double that of the lower transition energies predicted by the CEF_1 model. Thus, from the inelastic neutron data, the CEF_2 level scheme seems to provide a better description.

7.4 Calculations

7.4.1 Suzuki *et al.* parameters

Using the CEF_2 Stevens parameters obtained by Suzuki *et al.*, a set of eigenvalues and eigenvectors have been calculated and used to calculate the susceptibility, magnetisation and specific heat. In Figures 7.11 to 7.15, the black, red and blue lines refer to the *z*-, *x*-, and *y*-axis respectively.

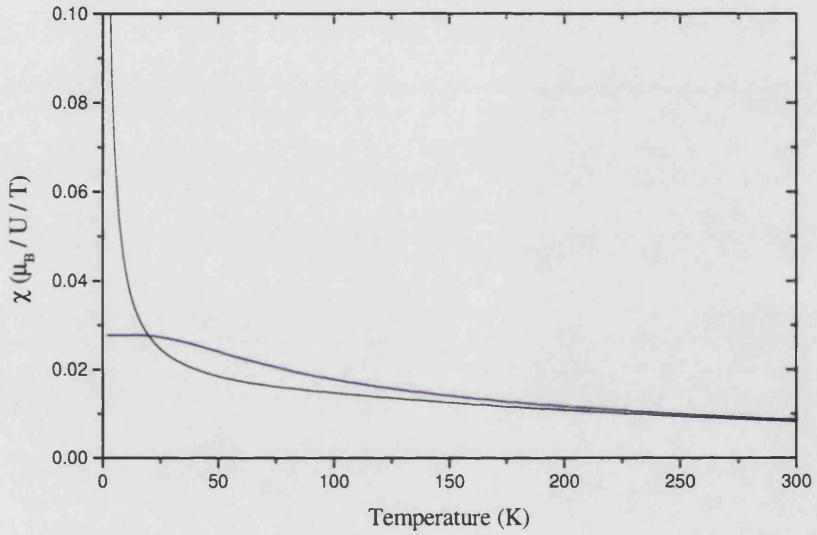

Figure 7.11 Susceptibility of UCu_2Sn calculated using the Suzuki *et al.* parameters.

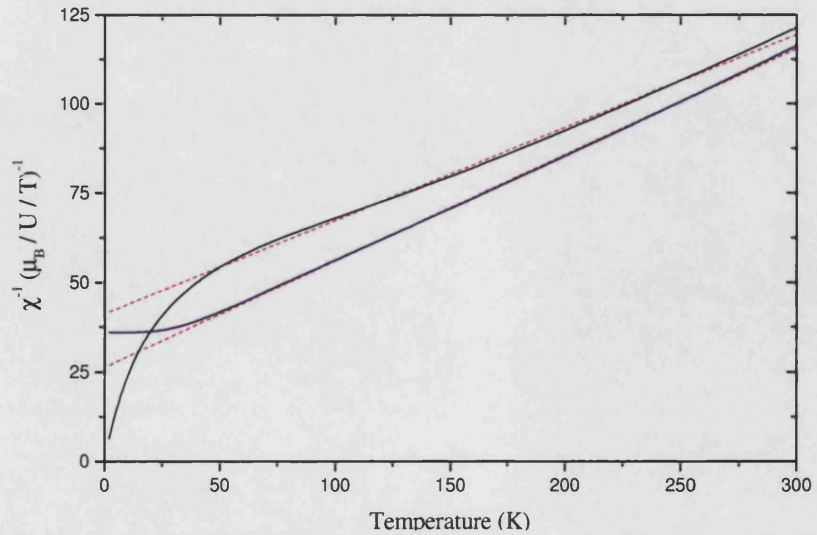

Figure 7.12 Inverse susceptibility of UCu_2Sn calculated using the Suzuki *et al.* parameters.

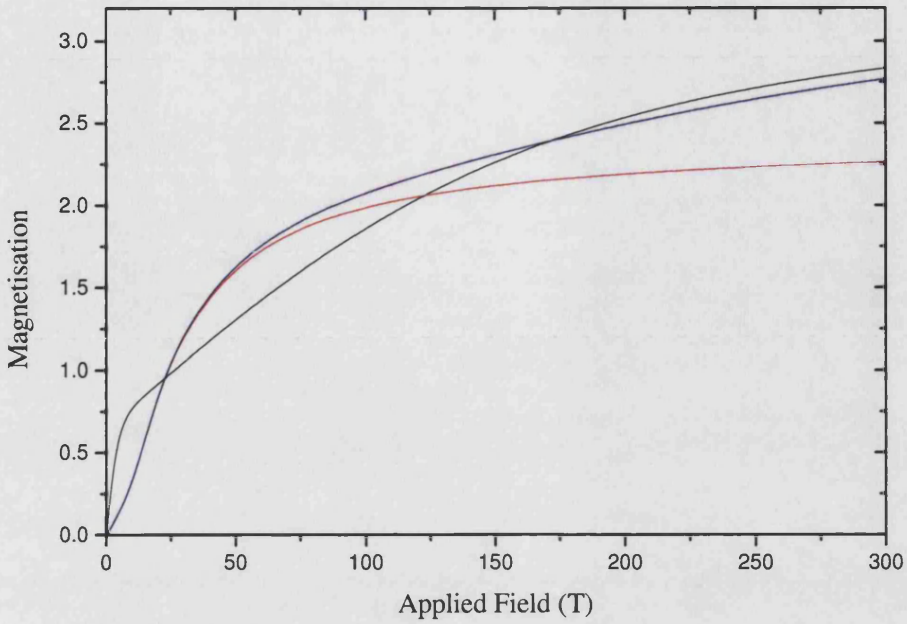

Figure 7.13 Magnetisation of UCu_2Sn calculated using the Stevens parameters obtained by Suzuki *et al.*

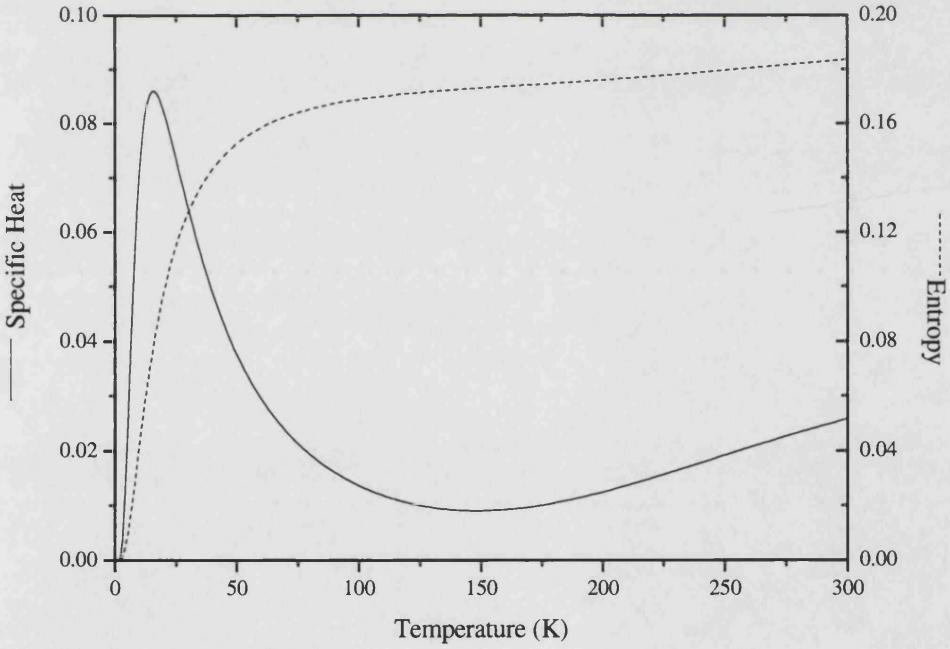

Figure 7.14 Specific heat and entropy of UCu_2Sn calculated using the Stevens parameters obtained by Suzuki *et al.*

7.4.2 FOCUS parameters

Using the equations derived in Section 1.4.1 and inserting the Curie-Weiss temperatures obtained from high-temperature susceptibility measurements (θ_a = -53 K and θ_c = -118 K), we obtain a value of B_2^0 = -0.121 meV. Using the ISIS program FOCUS to fit the inelastic neutron data, whilst keeping the B_2^0 parameter fixed at this value, the fits shown in Figure 7.15 are produced. The Stevens parameters corresponding to this fit are listed in the figure.

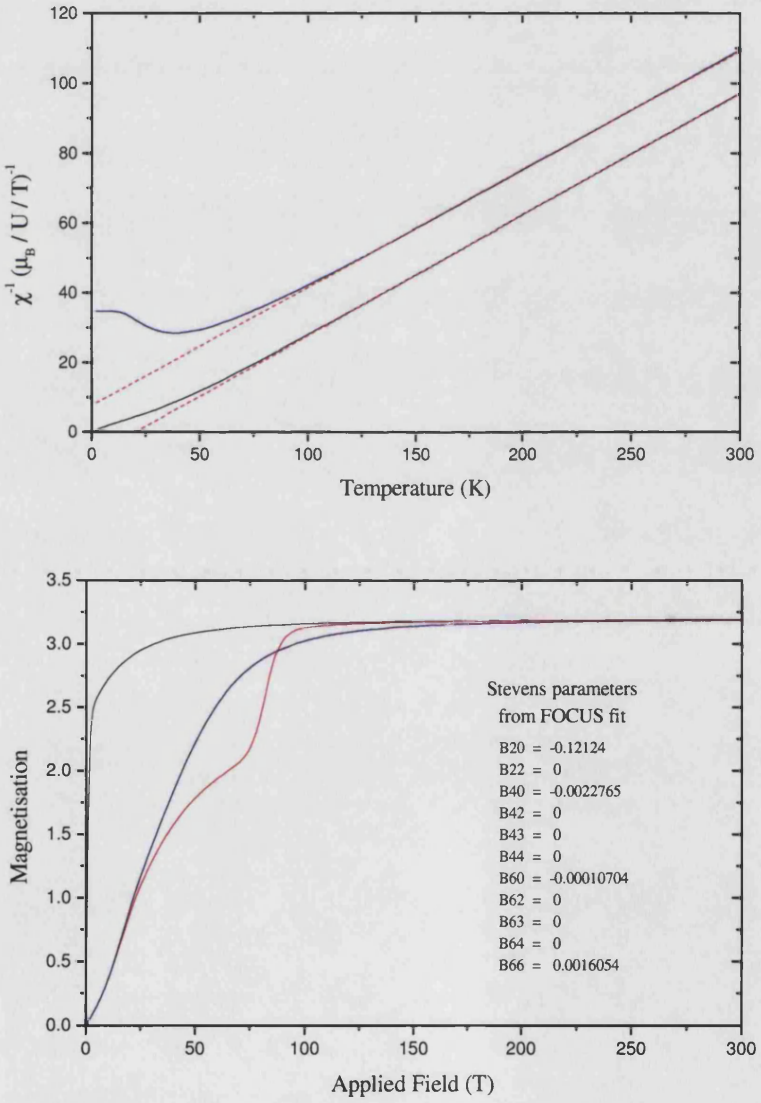

Figure 7.15 Calculations of the inverse susceptibility and magnetisation using the Stevens parameters obtained from the FOCUS fit.

7.5 Conclusions

Although the energy scale and details of the CEF_1 level scheme deduced by Suzuki *et al.* is not in accord with our measurements, the proposed Γ_5 ground state with a first excited Γ_1 state has much to commend it. Firstly, this ground state has the correct symmetry for the c_{66} elastic constant softening. Secondly, its charge density is pancake-like, and predominantly in the basal plane, whereas the charge density of the Γ_1 state is predominantly along the *c*-axis. Thus, at temperatures when the excited Γ_1 state has a significant thermal population, we anticipate a relatively strong hybridisation between U ions with these orbitals and the Cu and Sn ligands.

As the temperature is reduced and this excited state becomes depopulated, the U ions will consequently become much more localised. This mechanism may well explain the rapid temperature dependence of the inelastic scattering that we have observed, which is much faster than expected simply from the temperature factor due to thermal population of the CEF levels.

There is certainly not a straightforward CEF interpretation for the observed behaviour. Recently, a similar type of scattering was seen in the heavy fermion skutterudite compound, $CeRu_4Sb_{12}$. D. T. Adroja *et al.* observed broad, asymmetric magnetic scattering centred at 30 meV. They have interpreted their data in terms of an energy gap due to the hybridisation of localised *f* electrons and conduction bands. Similar hybridisation effects may have a part to play in the UCu_2Sn as well.

7.6 References

[1] Takabatake *et al.*, J. Phys. Soc. Japan, 61, 3 (1992) 778

[2] Takabatake *et al.*, J. Mag. Mag. Mat., 177-181 (1998) 53

[3] S. Wiese *et al.*, Physica B, 230-232 (1997) 95

[4] K. Kojima *et al.*, Physica B, 269 (1999) 249

[5] W. Higemoto *et al.*, Physica B, 281 & 282 (2000) 234

[6] K. Kojima *et al.*, Japan J. Appl. Phys. Ser., 11 (1999) 260

[7] T. Suzuki *et al.*, Phys. Rev. B, 62, 1 (2000) 49

CHAPTER 8

$U_3Pd_{20}Si_6$

8.1 Literature Review

Recent systematic bulk measurements were performed on the $R_3Pd_{20}Si_6$ series of ternary intermetallic compounds, which revealed magnetic ordering at low temperatures. The magnetic properties of these compounds are understood to arise from the competition between the RKKY interaction and CEF effects. Among these compounds, $Ce_3Pd_{20}Si_6$ attracted much attention due to successive quadrupolar (T_Q = 1.2 K) and antiferromagnetic (T_Q = 0.7 K) phase transitions.

More recently, Tateiwa *et al.* undertook a search for new ternary actinide systems $U_3T_{20}X_6$ (T = Pd, Pt or Ni, X = Si or Ge). They discovered[1,2] the compound $U_3Pd_{20}Si_6$ which is isostructural with the $R_3Pd_{20}Si_6$ series, i.e. an ordered derivative of the $Cr_{23}C_6$-type cubic structure (space group $Fm\bar{3}m$). The uranium atoms occupy two inequivalent crystallographic sites, 4*a* and 8*c*, which have cubic O_h and T_d point symmetries respectively.

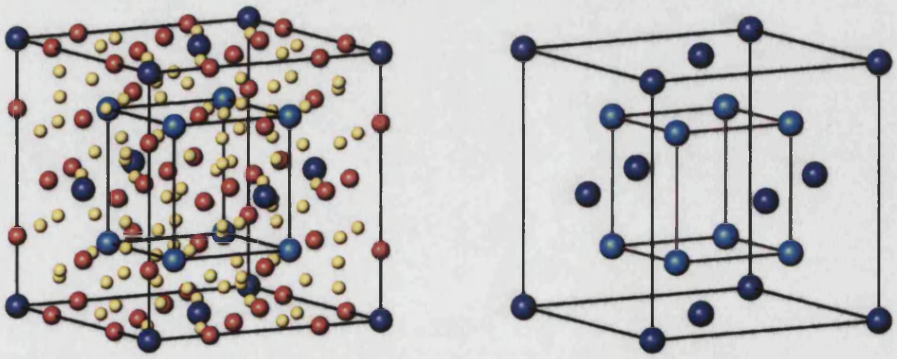

Figure 8.1 (a) The unit cell of $U_3Pd_{20}Si_6$ showing all atoms (U in blue, Pd in yellow and Si in red). (b) The uranium unit cell showing the different sites (4*a* in dark blue and 8*c* in light blue).

They performed measurements of the transport, thermal and magnetic properties on single crystals of $U_3Pd_{20}Si_6$, grown in a tri-arc furnace by the Czochralski pulling method under an Ar gas atmosphere. The resistivity was found to decrease down to 50 K, below which two anomalies are observed at 19 K and 2 K. The two transitions are also observed in the specific heat, with the peak at 19 K being of the λ-type and that at 2 K having a maximum around 2 K and extending to 5 K. The magnetic entropy, obtained by subtracting the specific heat of $La_3Pd_{20}Si_6$, reaches a value at 19 K which is close to Rln3.

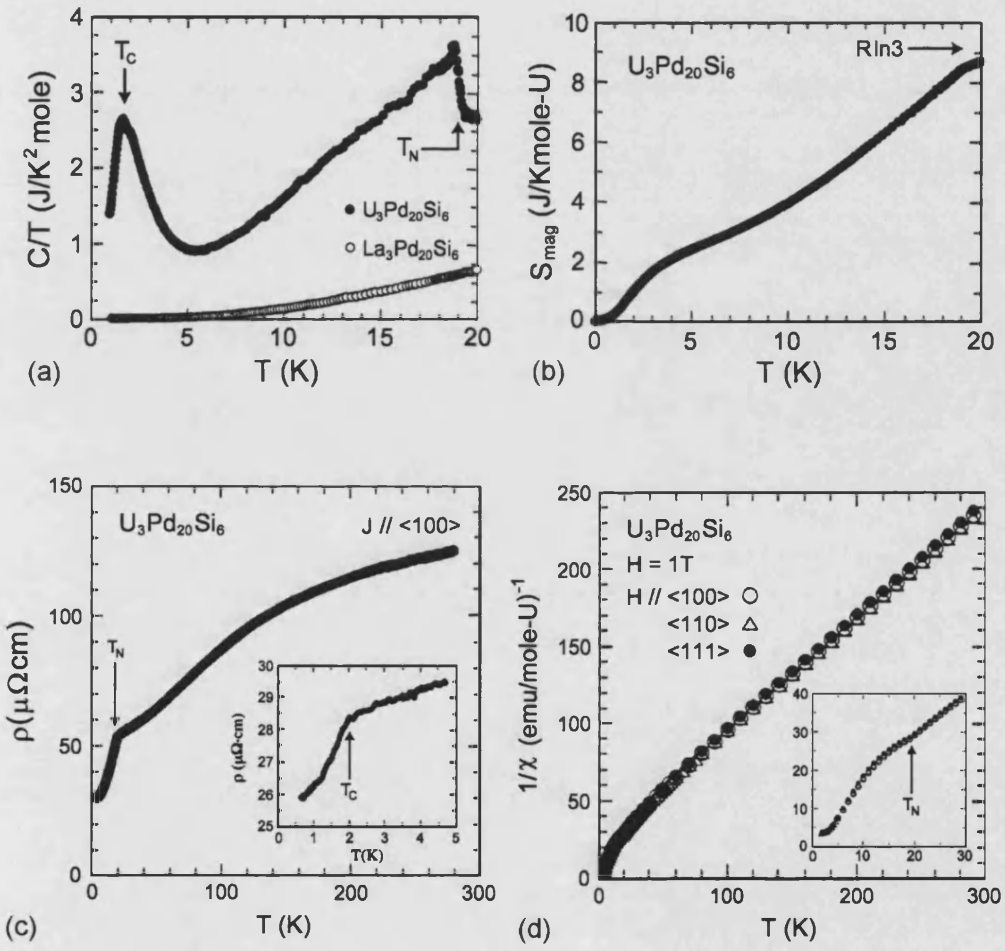

Figure 8.2 Transport, thermal and magnetic measurements of $U_3Pd_{20}Si_6$ showing the 19 K and 2 K transitions in (a) specific heat, (b) magnetic entropy, (c) resistivity and (d) inverse susceptibility (Tateiwa *et al.*)

At high temperatures from 50 K to 300 K, the magnetic susceptibility is isotropic and obeys the Curie-Weiss law with an effective moment $\mu_{eff} = 3.30\mu_B/\mathrm{U}$ and Curie-Weiss temperature θ = -30 K. A weak anomaly at 19 K in the inverse magnetic susceptibility indicated that it is due to antiferromagnetic ordering.

The magnetisation was found to diverge below 4 K in low magnetic fields, indicating that the 2 K anomaly is due to ferromagnetic ordering. The magnetisation is almost isotropic at all temperatures and varies linearly with applied field in the paramagnetic state. Below 19 K, however, a deviation from this linear relation suggests that a ferromagnetic component exists in the antiferromagnetic state. At 1.8 K, the magnetisation increases rapidly with a spontaneous magnetic moment of around $0.5\mu_B/\mathrm{U}$.

The microscopic magnetic properties of $U_3Pd_{20}Si_6$ were investigated[3] by ^{29}Si NMR. They found that the large, strongly *T*-dependent relaxation rate of the 5*f* moments indicated that the single-site dynamics due to hybridisation between the 5*f* and conduction electrons dominates the low energy spin dynamics in the paramagnetic state.

The field dependence of the heat capacity confirms that the 19 K and 2 K transitions are associated with antiferromagnetic and ferromagnetic order, respectively, since an external field shifts the two anomalies to lower and higher temperatures, respectively[4]. Furthermore, powder neutron scattering has shown[5] that type-II antiferromagnetic ordering occurs on the 8*c* sites at 19 K, with an ordered moment of $1.73\mu_B/\mathrm{U}$ at 7 K.

8.2 Experimental Procedure

Susceptibility and magnetisation measurements were made on a 0.105 g fragment taken from the same polycrystalline button which was used in the HET experiment described below. The susceptibility data was taken cooling from 300 to 1.8 K in applied fields of 0.1 and 1 T. The magnetisation data was taken from 0 to 2.4 T at temperatures of 1.8 and 3 K.

Before the main HET experiment, a white beam vanadium run was made to allow for the subsequent normalisation process. The 20.32 g polycrystalline button was then crushed to minimise crystallites and placed into an aluminium sachet. Initial measurements at 14 K were made using incident energies of 23, 60 and 200 meV, and these were followed by temperature dependence measurements using 23 and 60 meV neutrons. Finally, a search for intermultiplet transitions was made using an 800 meV incident energy.

Run number	Incident Energy (meV)	Chopper Speed (Hz)	Sample Temp (K)	Total μAhr
11128	White beam	vanadium	300	595
11136	23	150	6.5	1100
11132	23	150	14	1200
11140	23	150	25	600
11144	23	150	80	600
11142	23	150	150	781
11135	60	150	6.5	1100
11131	60	150	15	1100
11134	60	150	24	592
11139	60	150	25	600
11143	60	150	80	1400
11141	60	150	150	1800
11133	200	250	14	575
11137	800	600	6.5	325
11145	800	600	80	2183

Table 8.1 Summary of the scans performed during the HET experiment on $U_3Pd_{20}Si_6$.

8.3 Results & Discussion

8.3.1 SQUID results

The susceptibility measurements are shown in Figure 8.3 as a plot of inverse susceptibility against temperature. The high temperature data is almost linear, indicating that $U_3Pd_{20}Si_6$ exhibits Curie-Weiss behaviour. Fitting to the Curie-Weiss law between 50 and 300 K gives a Curie temperature of θ = -29.8 K and an effective magnetic moment of $\mu_{eff} = 3.32\mu_B$ in agreement with Tateiwa *et al.* (Note that four spurious points in the 0.1 T data were not included in the fit).

The inset of Figure 8.3 shows the low temperature part of the inverse susceptibility. A slight anomaly can be seen around 19 K which indicates the upper transition temperature, T_N. The susceptibility for the different applied fields begins to diverge below about 8 K.

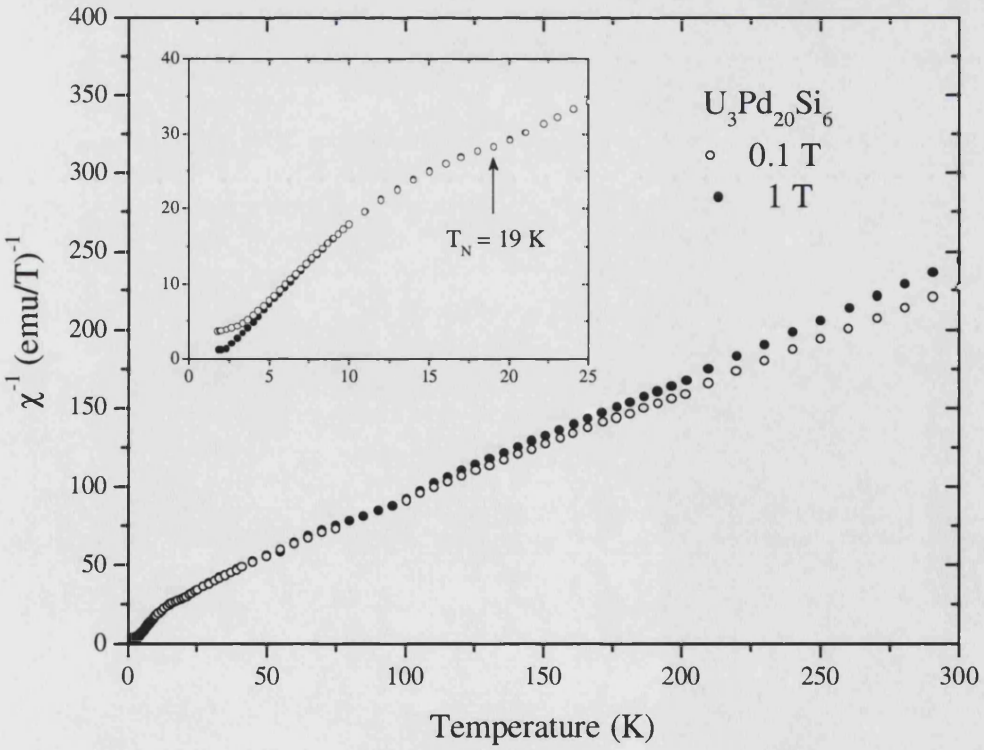

Figure 8.3 The inverse susceptibility of $U_3Pd_{20}Si_6$ measured in fields of 0.1 and 1 T. Inset: the low temperature part showing the transition at T_N = 19 K.

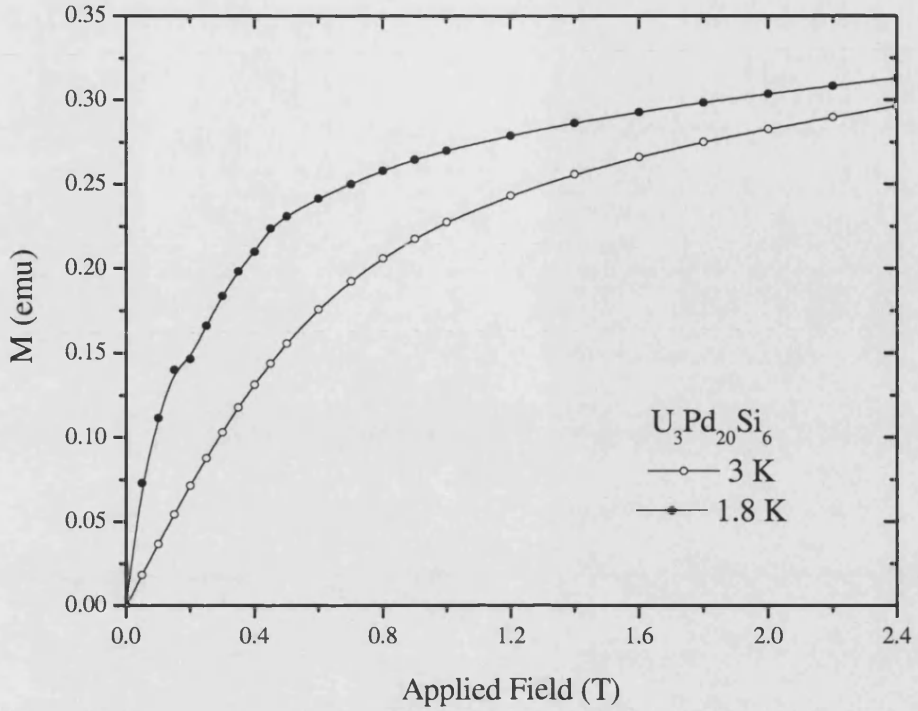

Figure 8.4 The magnetisation of $U_3Pd_{20}Si_6$ measured at temperatures of 1.8 and 3 K.

8.3.2 HET results

Since a non-magnetic reference compound, such as $Th_3Pd_{20}Si_6$, was not available the phonon contribution to the scattering has been estimated by reducing the high angle bank data by a constant factor of 4.5. This results in an underestimation of the phonon background, as shown by the energy gain side of the data.

Using an incident energy of 200 meV, the scattering above 50 meV is weak and is essentially flat. Below this however, there appears to be a shoulder of magnetic scattering between 20 and 40 meV. This can be seen more clearly in Figure 8.5 which is the data obtained using 60 meV neutrons. In fact it can be seen that the magnetic scattering starts to increase just below 10 meV and three distinct excitations are visible at energy transfers of around 14, 24 and 32 meV. Subtraction of the phonon background to leave just the magnetic scattering results in a 'smearing out' of the 14 meV peak.

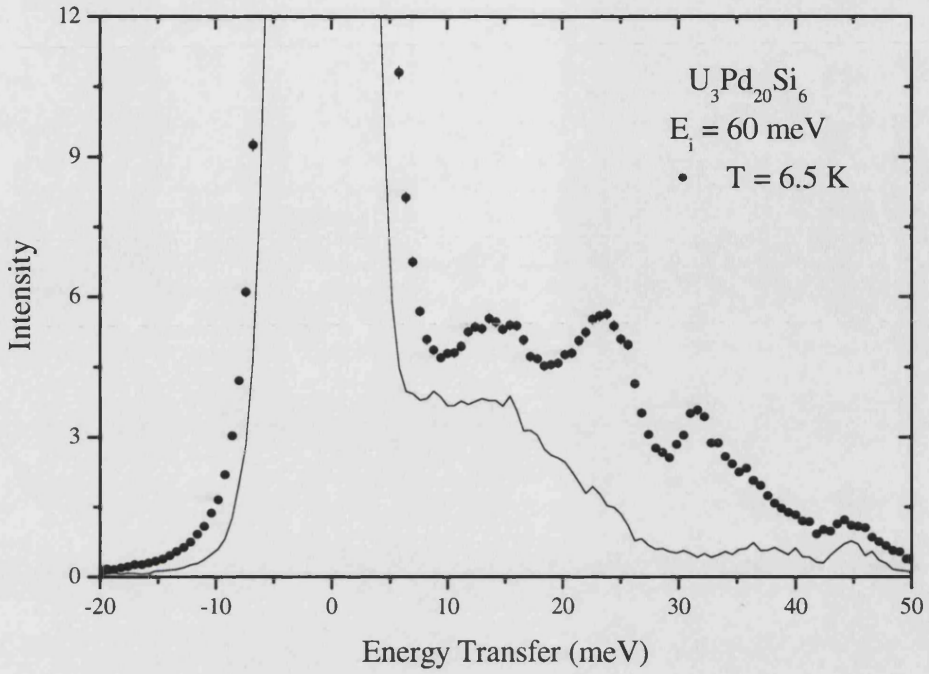

Figure 8.5 The total scattering from $U_3Pd_{20}Si_6$ (symbols) and the phonon contribution obtained by the scaling method (line) using E_i = 60 meV neutrons at T = 6.5 K.

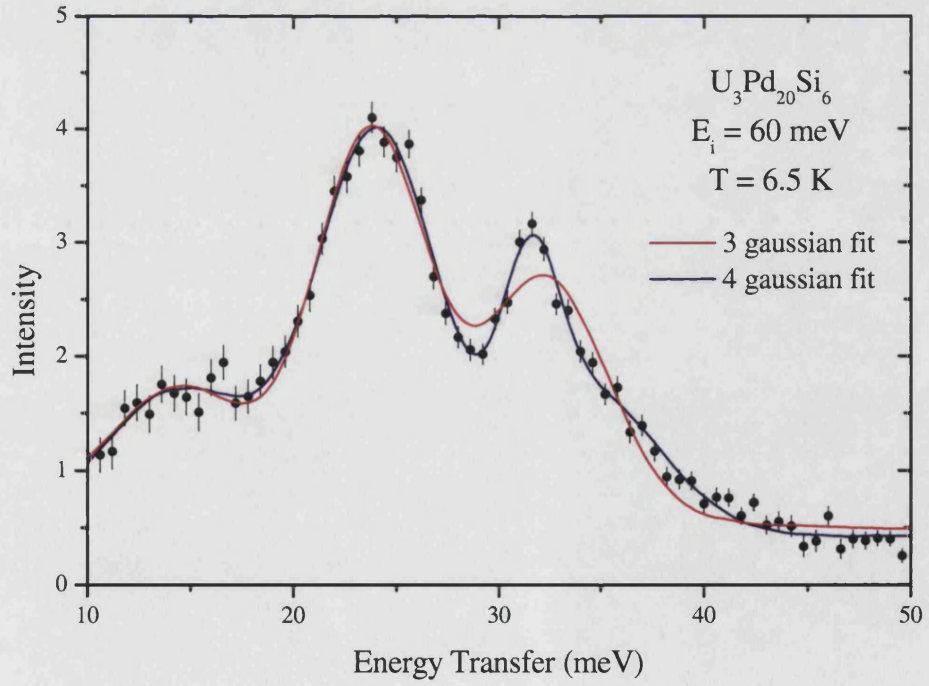

Figure 8.6 The resulting magnetic scattering from $U_3Pd_{20}Si_6$ after phonon subtraction. The red and blue lines are three and four gaussian fits to the data, respectively.

Fits to the magnetic scattering below 50 meV have been made using gaussian functions. Fitting with only three gaussians does not provide a satisfactory fit to the excitation around 32 meV. A fourth gaussian is required to account for the high energy tail of the scattering, enabling a narrower gaussian to describe the main part of the excitation (Figure 8.6).

The four peaks have been designated as A, B, C and D as shown in Figure 8.7. This analysis was repeated on all five temperature data sets simultaneously, whilst keeping the positions of peaks B, C and D fixed between all of the temperature data sets. The results of these fits are shown in Table 8.2. The parameters evolve reasonably smoothly with temperature with a general increase in the integrated intensity caused by the increase in peak width. The shift of peak A to lower energies is due to the increase in quasielastic scattering.

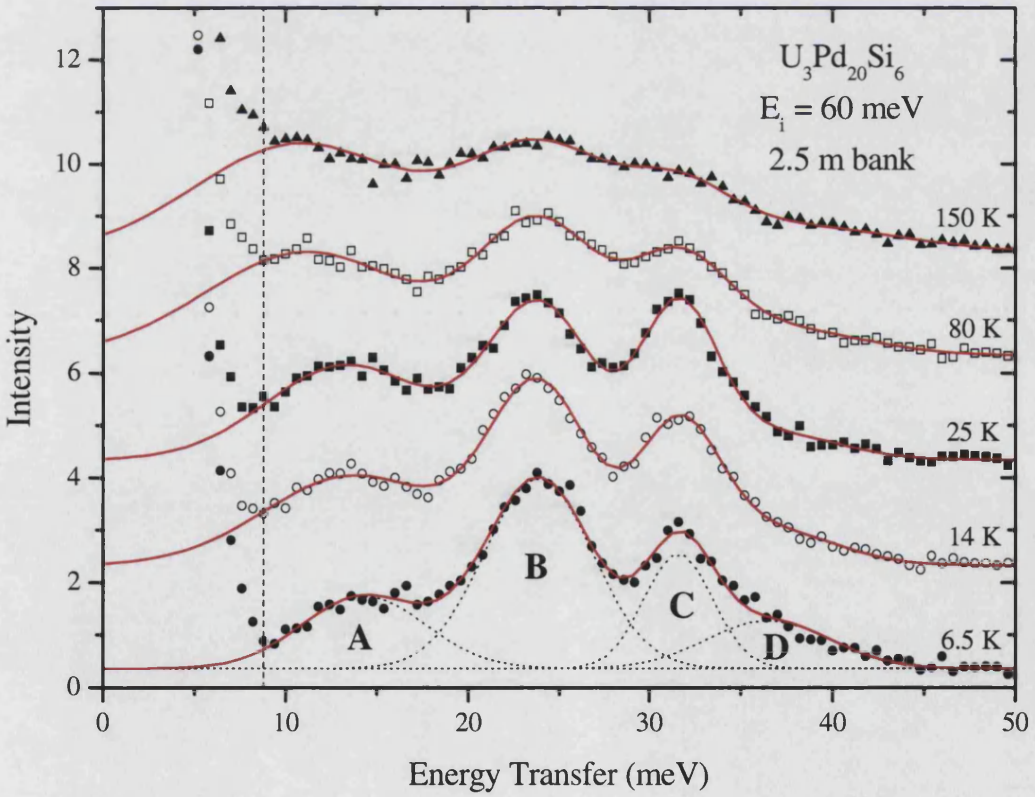

Figure 8.7 The magnetic scattering from $U_3Pd_{20}Si_6$ at various temperatures. The lines are simultaneous fits to the data above the dotted line.

T (K)	Parameter	Peak A	Peak B	Peak C	Peak D
6.5	E (meV)	14.27 ± 0.19	23.87 ± 0.05	31.58 ± 0.05	36.5 ± 0
	w (meV)	6.72 ± 0.42	5.97 ± 0.16	3.75 ± 0	6.72 ± 0.62
	A (mb/sr/U)	11.64 ± 0.78	27.18 ± 0.74	10.27 ± 0.36	7.65 ± 0.84
14	E (meV)	13.71 ± 0.23	23.87 ± 0.05	31.58 ± 0.05	36.5 ± 0
	w (meV)	9.77 ± 0.77	5.54 ± 0.22	4.42 ± 0.21	7.11 ± 0.96
	A (mb/sr/U)	21.01 ± 1.58	23.43 ± 1.26	14.13 ± 0.67	5.97 ± 0.91
25	E (meV)	13.37 ± 0.18	23.87 ± 0.05	31.58 ± 0.05	36.5 ± 0
	w (meV)	8.85 ± 0.57	5.68 ± 0.24	4.13 ± 0.16	7.20 ± 1.23
	A (mb/sr/U)	20.13 ± 1.25	20.92 ± 1.02	14.62 ± 0.60	4.66 ± 0.93
80	E (meV)	11.16 ± 0.36	23.87 ± 0.05	31.58 ± 0.05	36.5 ± 0
	w (meV)	11.25 ± 1.31	6.51 ± 0.38	5.13 ± 0.38	9.57 ± 1.81
	A (mb/sr/U)	28.14 ± 3.42	20.37 ± 1.72	10.37 ± 0.99	6.50 ± 1.51
150	E (meV)	10.75 ± 0	23.87 ± 0.05	31.58 ± 0.05	36.5 ± 0
	w (meV)	11.61 ± 1.02	7.81 ± 0.52	5.5 ± 0	13.61 ± 3.41
	A (mb/sr/U)	31.06 ± 4.05	18.93 ± 1.79	6.02 ± 0.72	9.82 ± 4.25

Table 8.2 Summary of the parameters obtained from the four gaussian fit to the magnetic data at various different temperatures.

The data obtained using neutrons with an incident energy of 23 meV at $T = 6.5$ K is shown in Figure 8.8a. The weak scattering of peak A can be seen between 9 and 17 meV. Below this, a sharp peak of much higher intensity is seen at around 3 meV. This peak is likely to be the result of a transition within the ground state itself, since it is at a very low energy transfer and since the matrix element of such a transition would be large.

The peak is present at $T = 14$ K (although not as well defined) but not at $T = 25$ K as shown in Figure 8.8b. Thus we can conclude that it must be the splitting of the ground state at the 8*c* site which results in the peak at 3 meV.

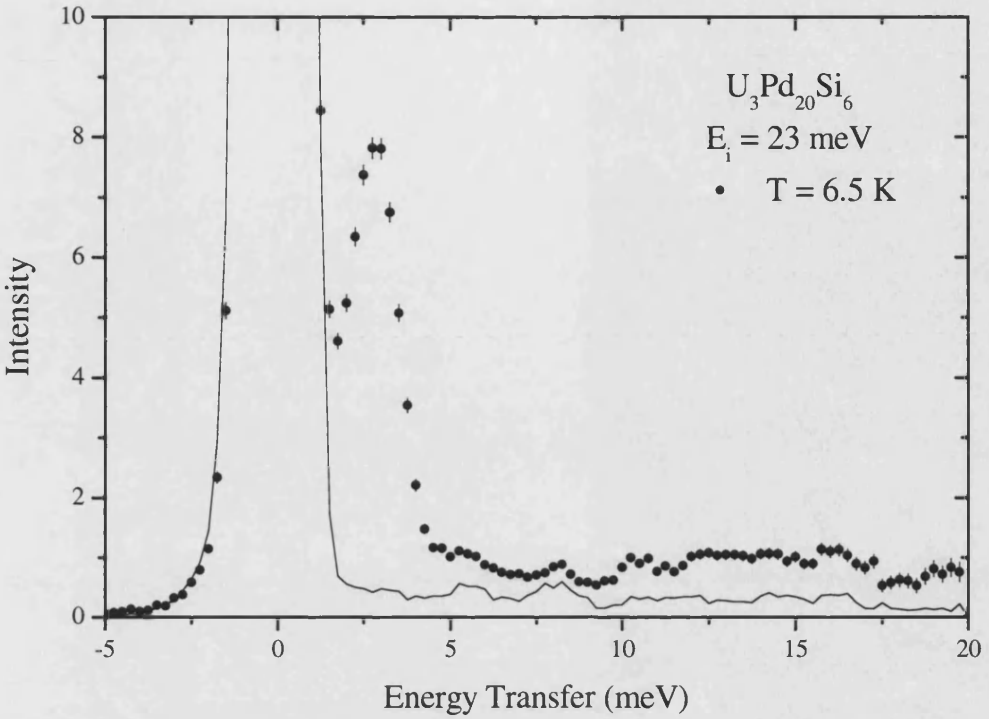

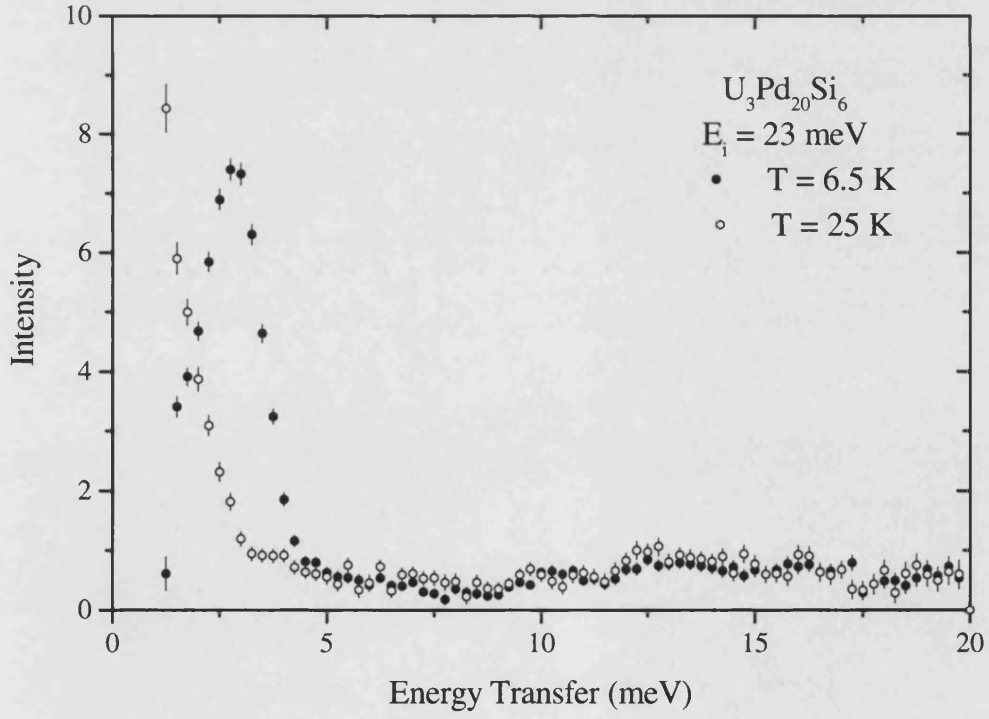

Figure 8.8 (a) The total scattering from $U_3Pd_{20}Si_6$ (symbols) and the phonon contribution obtained by the scaling method (line) using E_i = 23 meV neutrons at T = 6.5 and 25 K. (b) The resulting magnetic scattering from $U_3Pd_{20}Si_6$ after phonon subtraction.

8.4 Calculations

From the bulk measurements, it has been deduced that the uranium ions have a $5f^2$ configuration. The crystal fields at both U sites are cubic so the $J = 4$ multiplet will be split into a Γ_1 singlet, a Γ_3 doublet, a Γ_4 triplet and a Γ_5 triplet. From elastic constant measurements, the most likely ground state for both sites is the Γ_5 level which means that there are possible transitions from Γ_5- Γ_3 and Γ_5- Γ_4 at each site. The four peaks fitted to the magnetic data can therefore be attributed to the two transitions at each U site.

Using the Lea, Leask and Wolf (LLW) parameters[6] defined by:

$$B_4^0 = \frac{Wx}{F(4)} \quad \text{and} \quad B_6^0 = \frac{W(1-|x|)}{F(6)}$$

The LLW diagram can be plotted (as shown in Figure 8.9). Note that the eigenvectors obtained in this cubic CEF do not depend on the choice of Stevens parameters. They are displayed in Table 8.3.

The peaks positions at 6.5 K are 14.27, 23.87, 31.58 and 36.5 meV. Using the LLW diagram to find x positions for which the eigenvalue ratios match the ratios of the peak positions determined experimentally, a tentative CEF level scheme has been deduced. We can propose that the peaks at 14.27 and 36.5 K are related to the 4*a* sites and those at 23.87 and 31.58 K are related to the 8*c* sites, if we assume that the larger magnetic moments on the 8*c* sites will result in greater magnetic scattering.

If this is the case, we can obtain approximate x parameters to match the ratios of 2.73 (for the 4*a* sites) and 1.32 (for the 8*c* sites). The overall energy of the level scheme can then be adjusted using the W parameter to give levels at the measured values.

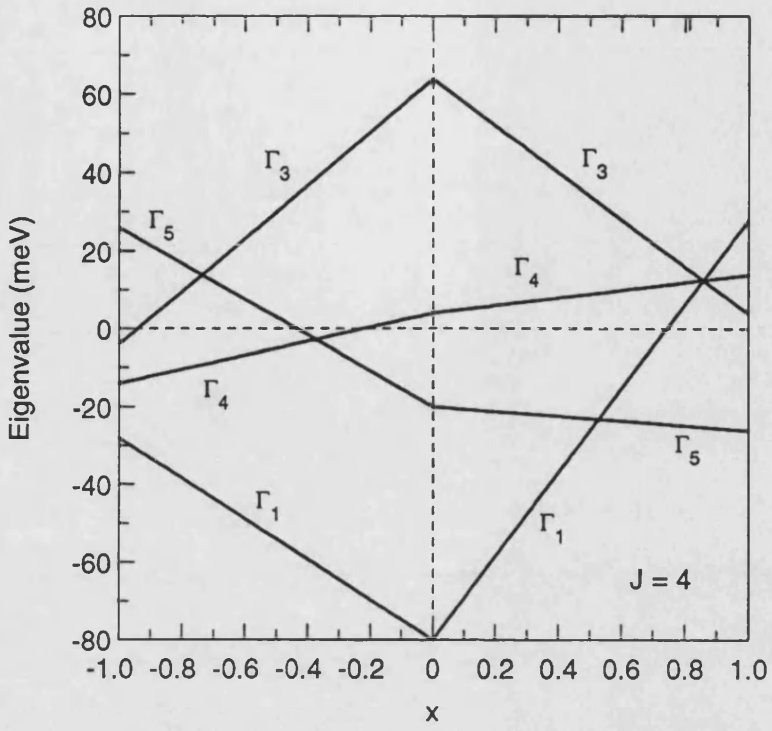

Figure 8.9 The LLW diagram for $J = 4$ with $W = 1$.

$$|\Gamma_1\rangle = 0.4564|+4\rangle - 0.7638|0\rangle + 0.4564|-4\rangle$$

$$|\Gamma_{3a}\rangle = 0.5401|+4\rangle - 0.6455|0\rangle + 0.5401|-4\rangle$$

$$|\Gamma_{3b}\rangle = 0.7071|+2\rangle + 0.7071|-2\rangle$$

$$|\Gamma_{4a}\rangle = 0.3536|+3\rangle + 0.9354|-3\rangle$$

$$|\Gamma_{4b}\rangle = 0.3536|-3\rangle + 0.9354|+3\rangle$$

$$|\Gamma_{4c}\rangle = 0.7071|+4\rangle + 0.0000|0\rangle - 0.7071|-4\rangle$$

$$|\Gamma_{5a}\rangle = 0.9354|+3\rangle - 0.3536|-1\rangle$$

$$|\Gamma_{5b}\rangle = 0.9354|-3\rangle - 0.3536|+1\rangle$$

$$|\Gamma_{5c}\rangle = 0.7071|+2\rangle - 0.7071|-2\rangle$$

Table 8.3 The CEF eigenvectors resulting from the splitting of the $J = 4$ multiplet in a cubic crystal field.

The obtained LLW and Stevens parameters (measured in meV) are:

$x \approx 0.2$ and $W \approx 0.5 \Rightarrow B_4^0 = 1.67 \times 10^{-3}$ and $B_6^0 = 3.17 \times 10^{-4}$, for the $4a$ sites

$x \approx 0.7$ and $W \approx 0.75 \Rightarrow B_4^0 = 8.75 \times 10^{-3}$ and $B_6^0 = 1.79 \times 10^{-4}$, for the $8c$ sites

The J_z transition matrix between the different eigenvectors is displayed below. Note the large value corresponding to the transition within the Γ_5 ground state. This could well explain the intense peak seen at very low energy, assuming the ground state is Γ_5.

	$\|\Gamma_{3a}\rangle$	$\|\Gamma_{3b}\rangle$	$\|\Gamma_{4a}\rangle$	$\|\Gamma_{4b}\rangle$	$\|\Gamma_{4c}\rangle$	$\|\Gamma_1\rangle$	$\|\Gamma_{5a}\rangle$	$\|\Gamma_{5b}\rangle$	$\|\Gamma_{5c}\rangle$
$\|\Gamma_{3a}\rangle$	0	0	0	0	9.333	0	0	0	0
$\|\Gamma_{3b}\rangle$	0	0	0	0	0	0	0	0	4.000
$\|\Gamma_{4a}\rangle$	0	0	0.250	0	0	0	1.750	0	0
$\|\Gamma_{4b}\rangle$	0	0	0	0.250	0	0	0	1.750	0
$\|\Gamma_{4c}\rangle$	9.333	0	0	0	0	6.667	0	0	0
$\|\Gamma_1\rangle$	0	0	0	0	6.667	0	0	0	0
$\|\Gamma_{5a}\rangle$	0	0	1.750	0	0	0	6.250	0	0
$\|\Gamma_{5b}\rangle$	0	0	0	1.750	0	0	0	6.250	0
$\|\Gamma_{5c}\rangle$	0	4.000	0	0	0	0	0	0	0

Table 8.4 The J_z transition matrix between the different eigenvectors.

8.5 Conclusions

The magnetic scattering from polycrystalline $U_3Pd_{20}Si_6$ has been investigated using inelastic neutron scattering. Three crystal field excitations have been found which suggests that this compound is a rare example of a uranium intermetallic with localised magnetic moments. The excitations are visible in the both the paramagnetic phase and the ordered phase. The positions and widths of these peaks do not change significantly with temperature, although the intensity of all of the peaks decreases with increasing temperature.

A very low energy peak at 3 meV has been observed below T = 25 K, which suggests that it is related to the transition at T_N = 19 K. Thus, it is proposed that this peak is due to the splitting of the ground state on the 8*c* sites. The subsequent transitions between these levels is likely to be large since the J_z matrix element couples strongly between the ground state Γ_5 eigenvectors.

8.6 References

[1] Tateiwa *et al.*, J. Phys. Soc. Japan **69**, 5 (2000) 1517

[2] Tateiwa *et al.*, Physica B **281 & 282** (2000) 254

[3] Maruta *et al.*, Physica B **281 & 282** (2000) 251

[4] Michor *et al.*, Physica B **284 – 288** (2000) 1303

[5] Tateiwa *et al.*, J. Phys. Soc. Japan **70**, 6 (2001) 1853

[6] K. R. Lea, M. G. M. Leask and W. P. Wolf, J. Phys. Chem. Solids **23** (1962) 1381

CHAPTER 9

Conclusions and Future Work

9.1 Overall conclusions

The rare-earth intermetallic, PrNiSn, is a prime example of a well localised magnetic system as proven by the occurrence of intense and well defined crystalline electric field excitations. The availability of this material in single crystal form has allowed the dispersion relations of these CEF excitations to be determined along the [0 0 **Q**] and [**Q** 0 0] symmetry directions.

The observed excitations agree extremely well with the CEF level scheme deduced from the inelastic scattering from a polycrystalline sample. The two excitations around 3.5 meV have previously been attributed to different modes of the same energy level. From the data presented in this thesis, we propose that the two excitations at 1.5 and 2.5 meV also originate from the same energy level. In this case they are taken to be different modes of the predicted energy level at 2 meV. Another of the predicted energy levels, the level at 5.1 meV, has also been observed and measurements made on it.

The dispersion of the 3.5 meV mode has been reported previously and the new data we have obtained appears to be able to account for the four modes of this level which arise from the coupling of the four Pr ions in the unit cell. The dispersion relations we have determined for the 1.5 and 2.5 meV modes along [0 0 **Q**] are symmetric and commensurate with the reciprocal lattice. They appear to move in phase with each other, in contrast to the 3.5 meV modes along the same direction. The excitation around 5.1 meV does not appear to be dispersive, at least not along the [**Q** 0 0] direction where detailed measurements were made.

Although the majority of uranium-based compounds show itinerant behaviour, examples of localised magnetism in such compounds can be found. Likely candidates may be revealed by their chemical, magnetic or transport properties. We have looked at three such compounds; UPdSn, UCu_2Sn and $U_3Pd_{20}Si_6$. In two cases, UPdSn and $U_3Pd_{20}Si_6$, we have observed clear excitations which exist in both the paramagnetic and ordered phases. We are therefore confident that the *f* electrons in these compounds are well localised and that these excitations are due to transitions between crystal field split energy levels.

The temperature dependence of the UPdSn excitation is unusual in that, although there are gradient changes at the transitions temperatures, the overall changes in position and intensity of the excitation peak are smoothly varying. We note from recent μSR data that there may be an overlap of the two antiferromagnetic phases which may explain our results. The temperature dependence of the CEF peak and also of the quasielastic scattering can be explained by an energy level scheme which we have derived from comparison of the calculated ground state specific heat with the experimental value.

The three magnetic peaks seen in $U_3Pd_{20}Si_6$ may also be interpreted as CEF excitations, although the determination of a level scheme is made more difficult due to the existence of two inequivalent U sites. The different point symmetries of the 8*c* and 4*a* sites mean that each site gives rise to an individual level scheme. An attempt has nevertheless been made to determine a set of CEF parameters which would account for the scattering we observe. An intense peak at very low energy can be explained by considering the splitting of the ground state when the material orders. Transitions within the split ground state are predicted to have a large J_z component which would explain the intensity of the scattering.

The broad, asymmetric magnetic scattering from UCu_2Sn is unusual and the lack of distinct excitations means that it is not straightforward to interpret the system in terms of a CEF level scheme. The disappearance of this scattering above the ordering temperature suggests that other effects such as hybridisation between the *f* electrons and the delocalised ligand electrons must be taken into account.

9.2 Future work

9.2.1 PrNiSn

The completion of our dispersion measurements along [0 0 **Q**] and [**Q** 0 0] is desirable, especially of the 2.5 meV mode along [**Q** 0 0] to determine its relation to the 1.5 meV mode in this direction. Measurements along other symmetry directions, especially along [0 **Q** 0], would be extremely interesting.

Since the dispersion appears to be relatively strong for the 3.5 meV mode, an experiment on the MAPS spectrometer at ISIS would allow wide regions of the dispersion to be surveyed. Measurements on a high quality single crystal of NdNiSn would also make an interesting experiment.

9.2.2 UPdSn

The energy level scheme we deduced to explain our temperature dependence results predicts transitions to occur at around 80 meV both in the paramagnetic phase and in the ordered phase. Our measurements have not allowed us to determine whether scatting corresponding to such a transition is present or not. Therefore higher energy measurements using 130 meV incident neutrons at both high and low temperatures would allow our predicted energy scheme to be scrutinised. Application of a magnetic field would be another experiment to test the proposed scheme since the eigenfunctions would be strongly affected by such a perturbation.

9.2.3 UCu_2Sn

The only measurements we performed in the paramagnetic phase were either at very high or very low energies. In order to test the level schemes proposed by Suzuki *et al.* measurements would need to be made in the paramagnetic phase using neutrons with an incident energies of perhaps 60 and 130 meV. It would then be possible to determine whether or not the transitions predicted to occur at 28.6, 35.8, 50.4 and 75.9 meV actually exist. Single crystal studies of UCu_2Sn, perhaps on a triple-axis spectrometer such as V2, would allow an investigation of whether the broad scattering we have observed is actually comprised from individual peaks.

9.2.4 $U_3Pd_{20}Si_6$

The existence of two cubic U sites provides problems in determining which of the sites is responsible for the different energy peaks we have measured. A triple-axis experiment with measurements made at a number of temperatures above and below each of the two transition temperatures may allow such a distinction to be made. Crystal field schemes would then be able to be deduced for each site.

9.2.5 Localised U compounds

Searches should also continue to be made for localised uranium compounds, since they are able to provide us with information on *f-f* interactions, as well as demonstrating the effects of hybridisation on localised magnetism. Experiments on such compounds will hopefully help with the formation of a 'standard model', such as that for the rare-earths, which would be able to explain magnetism in the actinides.